University of Massachusetts Amherst

ScholarWorks@UMass Amherst

Summer November 2014

Lightweight, High-Temperature Radiator for In-Space Nuclear-Electric Power and Propulsion

Briana N. Tomboulian
University of Massachusetts Amherst

Lightweight, High-Temperature Radiator for In-Space Nuclear-Electric Power and Propulsion

A Dissertation Presented

by

BRIANA N. TOMBOULIAN

Submitted to the Graduate School of the
University of Massachusetts Amherst in partial fulfillment
of the requirements for the degree of

DOCTOR OF PHILOSOPHY

September 2014

Mechanical and Industrial Engineering Department

Lightweight, High-Temperature Radiator for In-Space Nuclear-Electric Power and Propulsion

A Dissertation Presented

by

BRIANA N. TOMBOULIAN

Approved as to style and content by:

_____
Robert W. Hyers, Chair

_____
David P. Schmidt, Member

_____
Sanjay R. Arwade, Member

_____
Donald L. Fisher, Department Head
Mechanical and Industrial Engineering Department

ACKNOWLEDGEMENTS

ABSTRACT

LIGHTWEIGHT, HIGH-TEMPERATURE RADIATOR FOR IN-SPACE NUCLEAR-ELECTRIC POWER AND PROPULSION

SEPTEMBER 2014

BRIANA N. TOMBOULIAN, B.S., SMITH COLLEGE

Ph.D., UNIVERSITY OF MASSACHUSETTS AMHERST

Directed by: Professor Robert W. Hyers

The desire to explore deep space destinations with high-power and high-speed space+craft inspired this work. Nuclear Electric Propulsion (NEP), shown to provide orders of magnitude higher specific impulse and propulsion efficiency over traditional chemical rockets, has been identified as an enabling technology for this goal. One of large obstacle to launching an NEP vehicle is total mass. Increasing the specific power (kW/kg) of the heat radiator component is necessary to meet NASA's mass targets.

This work evaluated a novel lightweight, high-temperature carbon fiber radiator designed to meet the mass requirements of future NEP missions. The research is grouped into three major sections: 1) a micro-scale radiation study, 2) bench-scale experimental and analytical investigations, and 3) large-scale radiator system modeling.

In the first section, a Monte Carlo ray tracing model built to predict the effective emissivity of a carbon fiber fin by modeling the radiation scattering among fibers showed that the added surface area of the fibers over a flat fin surface increases the effective emissivity of the radiator area by up to 20%. The effective emissivity increases as the fiber volume fraction decreases from 1 to about 0.16 due to increased scattering among the fibers. For fiber volume fractions lower than 0.10, the effective emissivity decreases rapidly as the effect of radiation transmission becomes significant.

In the second section, thermal analyses of the carbon fiber radiator fin predicted that these radiators could meet NASA's performance targets by reducing the areal density to 2.2 kg/m^2 or below. These models were validated through experimental tests conducted on sub-scale radiator test articles. This work elevated the technology readiness level (TRL) of the carbon fiber radiator fin from level 2 to 4.

In the last section, a radiator system model for an NEP vehicle was built to analyze the dependence of radiator mass on selected system parameters. The model was used to minimize the radiator mass for test cases. The results predicted that carbon fiber fins operated near 600°C reduced the radiator mass by a factor of 7 as compared with traditional radiators operating near 100°C. This significant mass-reduction could enable future NEP systems.

TABLE OF CONTENTS

LIST OF TABLES

LIST OF FIGURES

CHAPTER 1

INTRODUCTION

1.1   Purpose and Overview

The needs of NASA's deep space missions were of special interest to the author since they involve both increased energy efficiency and the use of new materials. A NASA research program in these areas provided an opportunity for the author to pursue applications of mechanical engineering to the design of advanced technologies.

One of NASA's "Grand Challenges" is affordable and abundant power for space travel. According to NASA's 2010 Space Power and Energy Storage Roadmap, nuclear electric power can "provide 'game-changing' solutions for powering advanced NASA missions" [1]. Nuclear electric propulsion (NEP) could enable extended space missions ranging from interplanetary exploration to space colonization, but is not yet feasible, in part due to limited efficiency of the current state-of-the-art heat rejection technologies. The waste heat generated during the thermal to electric power conversion cycle must be dissipated by thermal radiation to space. Utilizing a traditional metallic fin radiator for an unmanned NEP spacecraft, the radiator alone would amount to around 40% of the total mass of the spacecraft [2]. At a price of $10,000 per pound (in 2010 dollars) to launch mass to Lower Earth Orbit (LEO), NEP missions will require advanced, low-density radiators [3].

The work presented here consists of research on several aspects of the design and fabrication of a lightweight, high-temperature carbon fiber radiator for space-based nuclear-electric power conversion systems. The goal of this work is to design, fabricate, and test a low-density, high-temperature carbon fiber radiator that meets NASA's areal density target for space-based radiators of 2-4 kg/m^2, improving on existing metallic and composite radiators with areal densities typically greater than 5 kg/m^2. This

goal was achieved by a combination of detailed heat transfer models and radiator test article experimentation as shown in Chapters 3-5.

The important characteristics of an advanced radiator include: low-density, high thermal conductivity, high emissivity, high temperature tolerance, and micrometeorite damage tolerance. As the radiator temperature is allowed to increase, the total radiating area required for a given heat load decreases. The combination of lightweight materials with superior thermal properties, and high operating temperatures enables significant reductions in radiator mass.

The main contributions detailed in this work are:

(1) A detailed model of the radiation within an array of carbon fibers was built and used to predict the dependence of effective emissivity on fiber volume fraction. The model details and findings are presented in Chapter 2.

(2) Chapter 3 discusses proof-of-concept testing of a carbon fiber radiator, including design and fabrication of test articles. The test articles consisted of woven fiber fins with a high-temperature heat pipe. Test articles were used in subsequent studies to quantify the fin performance. The main fabrication steps were weaving carbon fiber into a high-quality textile, manufacturing sodium heat pipes, and joining the textile and heat pipe with a titanium-copper-silver braze.

(3) The total hemispherical emissivity and longitudinal thermal conductivity of the carbon fiber fin were measured. The emissivity was measured using a room-temperature reflectometer and the longitudinal thermal conductivity was measured using a combination of infrared imaging and thermal models. The power radiated from a fin per unit width of heat pipe was measured using data collected by infrared images. A discussion of the methods and conclusions is presented in Chapter 4.

(4) A parametric study was conducted of the heat rejection from a carbon fiber fin over a range

of fin thicknesses, lengths and root temperatures using a detailed finite element model. An

analytical model was fit to the parametric data, which was used to easily automate radiator

optimization studies. The model development is discussed in Chapter 5.

(5) A thermal resistance model of a space-based heat rejection system was built incorporating

the analytical fin heat transfer model developed above. An optimization of the heat

rejection system mass for a nuclear-electric power system test case with a 700 kW waste

heat load was conducted in Chapter 5. The optimal solution for the high-temperature

carbon fiber heat rejection system yielded an areal density of 2.28 kg/m^2, which meets

NASA's areal density target, and is significantly lower mass than designs presented in

previous NASA studies.

1.2   Background

Advancing technologies, especially in power generation, propulsion, and communication, have

enabled increasingly complex space exploration missions. Travel to the outer planets and interstellar

space are of interest to the science community and NASA, but are limited by the present-day low-power,

low-speed propulsion methods and by vehicle and fuel weight. The latest mission to Mars, the Mars

Science Lab with the Curiosity rover, took approximately 9 months to reach the planet, while the current

Jupiter mission Juno will take 5 years to reach its destination [4][5]. If the same propulsion methods

used in the existing spacecraft were used for interstellar space missions, the travel time would be

undesirably high. Voyager 1, which is currently the farthest spacecraft from Earth, has reached the

Heliosheath (the region between the Termination Shock and Heliopause, see Figure 1.1) after 35 years in

flight. It would take Voyager 1 approximately 77,000 years to reach the next closest star, Alpha

Centauri. Developing faster spacecraft is necessary for completing deep-space missions on the human time-scale.

The "Innovative Interstellar Explorer" is a NASA project aimed at breaking out of our solar system to reach interstellar space, as shown in Figure 1.1 [6]. The nearest interstellar space is approximately 200 AU away, where 1 AU (astronomical unit) is the mean distance from the Earth to Sun [7][8]. In order to reach interstellar space within 15 years from launch, velocities of at least 63 km/s must be achieved [6], which is not possible with chemical or nuclear thermal propulsion systems. Nuclear-electric propulsion (NEP) has been identified as a potential 'game-changing' technology for achieving the high-speeds necessary for reaching deep-space destinations in reasonable travel times [1][9][10].
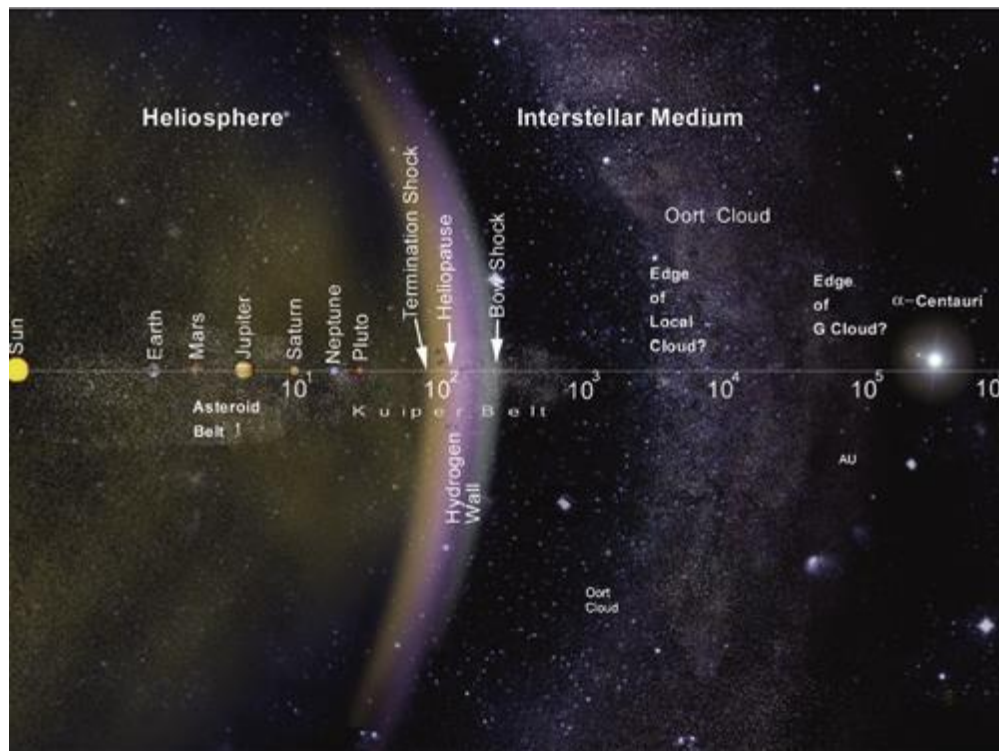
Figure 1.1: Relative distances (in AU) in our solar system and its surroundings [6].

The following sections provide additional background on deep-space travel, nuclear-electric propulsion, and heat rejection technologies.

1.2.1 Deep Space Missions

There have been many successful unmanned missions to Mars including Viking Landers 1 and 2 (1975), Mars Pathfinder (1996), Mars Odyssey (2001), Mars Exploration Rovers Spirit and Opportunity (2003), Mars Reconnaissance Orbiter (2005), Phoenix Lander (2007), and the Mars Science Laboratory (2012) [4]. With an increasing number of successful Mars probes, NASA is now considering manned missions to the planet. High-speed NEP vehicles could enable manned missions by decreasing the travel durations.

During the past few decades, there have been several successful unmanned missions to remote planets within our solar system. The first unmanned probe to Jupiter, Pioneer 10, reached the planet in 1973, followed by Pioneer 11 (1973), Voyager 1 and 2 (1977), and Galileo (1989). Other deep-space missions have included: Ulysses (1990) whose mission was to study the north and south poles of the sun, but flew by Jupiter to use the planet's gravitational field to assist its trajectory; Cassini-Huygens (1997) is a Saturn orbiter; New Horizons (2006), which is on its way to Pluto and also used Jupiter's gravitational field to assist its trajectory; Juno (2011) is a Jupiter orbiter that is scheduled to reach the planet in 2016. The next-step for unmanned deep-space exploration is to employ advanced propulsion systems that can achieve higher vehicle velocities.

1.2.2 Existing Deep-Space Power and Propulsion

Deep-space probes are launched out of Earth's gravitational field and set on a trajectory using large chemical rockets. Any additional propulsion for maneuvering or adding speed in space has typically been provided by smaller chemical thrusters. Once in space, other energy sources can be used to provide power for scientific instrumentation (payload) and communication. To date, only two different types of power systems have been used in NASA's interplanetary probes. The two types of systems are radioisotope thermoelectric generators (RTG), a type of nuclear power, and photovoltaic

solar power. An RTG uses thermal energy generated by natural radioactive decay of radioisotopes like

plutonium to generate electrical power using a thermoelectric generator, which is essentially a

thermocouple and discussed in more detail later [11]. Power output from an RTG is governed by the

amount of radioactive fuel available and its half-life, so it steadily decreases and cannot be controlled

during operation [6]. During long missions, spacecraft capabilities are reduced as the RTG power level

drops below the required amount to sustain the entire load [8]. Pairing radioisotope heat sources with

Stirling engines has been investigated, which provides more power than the static power converters in

RTG's but has the same heat source limitations [12].

The advancement of photovoltaic solar-power technology has enabled its use in the Juno probe,

the first solar-powered system used on a mission to an outer planet [5]. Even with significant

improvements, solar power is inherently limited to destinations close to and in view of the sun. For

example, the solar intensity at Pluto is more than 900 times less than at Earth [13]. Similar to RTG-

powered spacecraft, photovoltaic solar-powered spacecraft use electrical power for the science payload

and communication, and not for propulsion. Neither RTG nor photovoltaic solar power sources are ideal

for powering efficient propulsion on deep-space missions.

1.2.3   Nuclear Energy Source for In-Space Propulsion

Nuclear fuels used in fission reactors provide seven orders of magnitude more energy per mass

than chemical propellants used in combustion, as shown in Figure 1.2. For perspective on the energy

density of nuclear fission versus combustion, the energy obtained by fissioning the amount of uranium

that could fill a soda-can is about 50 times the energy contained in the Shuttle External Tank, as shown

in Figure 1.3 [14]. Nuclear fission energy has the highest specific energy density of all of the viable

energy sources for propulsion [14], and can enable the longest period of continuous high power output

as shown in Figure 1.4 [11].
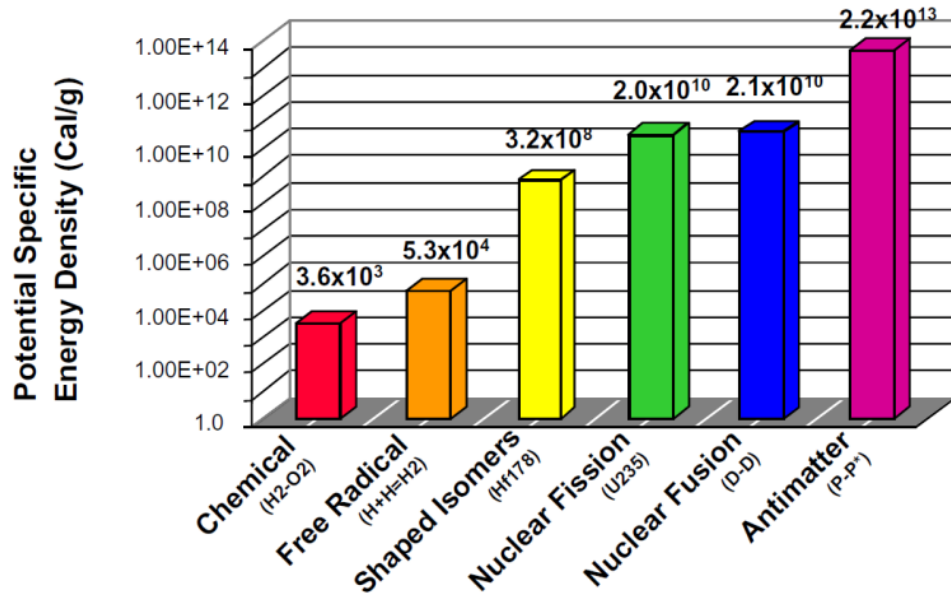
Figure 1.2: Propulsion Energy Sources [14]

Figure 1.3: External fuel tank for the Space Shuttle [15].
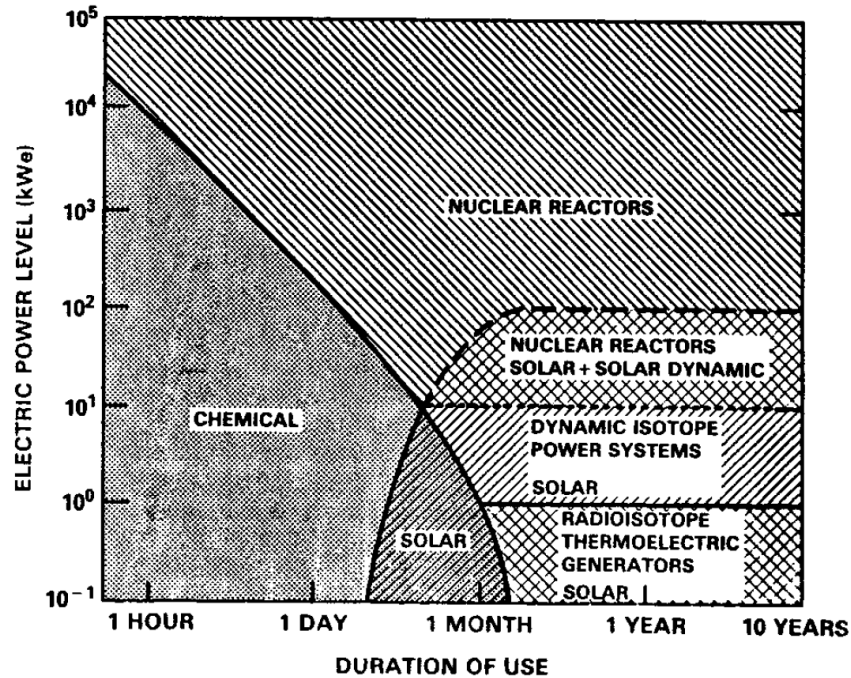
Figure 1.4: Regimes of space power applicability [11]

A nuclear fission energy source has not yet been used on a deep-space mission, but combining a nuclear fission power source with electric propulsion has the potential to provide the high-power and high-speed required to reach interstellar space in under 20 years. Thus, NEP is a leading propulsion option for deep-space missions, according to NASA

From 1967 to 1988, Russia launched at least 37 nuclear fission reactors into Earth's orbit on Kosmos satellites, during a program called RORSAT (Radar Ocean Reconnaissance SATellite) [13]. In 1969, the US launched their one and only space nuclear reactor on a mission called SNAP-10A. The SNAP-10A vehicle shown in Figure 1.5 was designed to test the safety and viability of flying nuclear reactors [13][16].

Figure 1.5: NASA's SNAP-10A spacecraft with a nuclear reactor at the top [16].

One of NASA's current challenges with using nuclear reactors in space is the negative public opinion of nuclear energy safety in the U.S. [13][17]. A primary design requirement for U.S. space nuclear reactors is safety, meaning that the reactor must stay in a subcritical condition (no self-sustaining nuclear fission reactions taking place) during launch and during potential accident situations [13]. There have been eight reported accidents involving nuclear-powered spacecraft: three U.S. and three Russian RTG vehicles, and two Russian vehicles with nuclear fission reactors. The organizations responsible for these incidents claim that the systems met the safety requirements and posed no threat to people [13]. Even though safety and public opinion issues have created barriers for using nuclear power in the past, continued improved safety and experience with reactors may allow advances in in-space nuclear technology, critical to the next generation of deep-space probes [17][13].

1.2.4   Nuclear Electric Power and Propulsion

Nuclear electric propulsion is the combination of two separate energy conversion processes: converting nuclear energy to electricity, and generating thrust (kinetic energy) from electric energy. Figure 1.6 provides a schematic of the NEP power subsystem with the thermodynamic power engine in

yellow, the nuclear fission reactor (heat source) in red, and radiator (heat sink) in blue. Waste heat can also be directed to any system that requires heating. Electric power output from the engine is directed to electric thrusters and any spacecraft subsystem requiring power. The thrusters repel a high molecular weight propellant from the spacecraft, which imparts a thrust on the vehicle in the opposite direction.
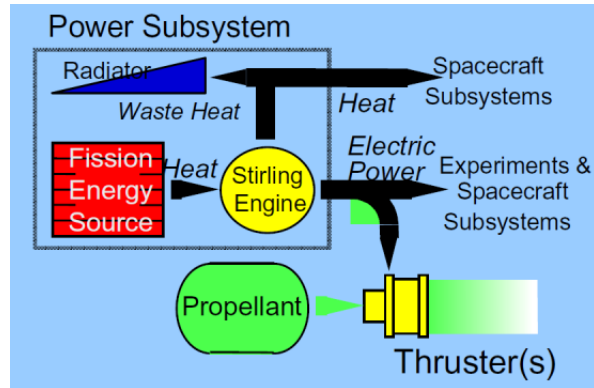
Figure 1.6: Schematic of Power Subsystem for NEP [14]

Advantages of using nuclear-electric propulsion include that it requires little propellant, has maximum thrust capability at all locations in space (no dependence on solar proximity or orientation), can generate thrust for extended periods (tens of months), and is essentially non-radioactive until it leaves the Earth's orbit [14]. A primary performance target for space nuclear power systems is to generate 100 kWe of power with a specific mass no greater than 30 kg/kW [18]. With numerous benefits over existing propulsion technologies, NASA has great interest in developing NEP [3][1][9]. Brief descriptions of the major components in an NEP system are provided below.

1.2.4.1 Reactor

In a nuclear reactor, fissile isotopes of plutonium or uranium (typically U233, U235, Pu239 or Pu241) split in a fission reaction when hit with a neutron with a certain amount of energy. When the nucleus of a fissile atom is struck by a free neutron, the neutron joins the nucleus, which becomes highly

unstable and splits into two fragments called fission products. These fragments repel each other at extremely high velocities and heat is generated from friction as surrounding media slows the fissile products. The friction between the fragments and the fluid creates heat, which increases the local temperature in the core. In addition to heat generated by friction, the fission reaction emits gamma rays, additional free neutrons that initiate subsequent reactions, beta particles, and neutrinos. The fragments are usually unstable and will decay to stable end products. The total energy released from one fission reaction is about 200 MeV (3.2×10^{-11} J), and about 80% of that is converted to heat [19].

The fuel (fissionable isotopes) and its containment shell together forms a 'fuel element'. The fuel containment shell is called cladding, which is typically cylindrically-shaped and metal. Cladding prevents the radioactive material from contaminating the reactor coolant. The reactor core consists of many fuel elements arranged in a close-packed hexagonal configuration. The heat generated by the fission reactions is absorbed by a coolant that flows between the fuel elements and carries the heat out of the core. Leaving the reactor core, the coolant flows through a pumped closed loop delivering thermal energy to the hot side of the power conversion cycle. Figure 1.7 is a schematic of a reactor core showing the fuel element configuration and how the coolant flows around the elements and out through a single pipe.
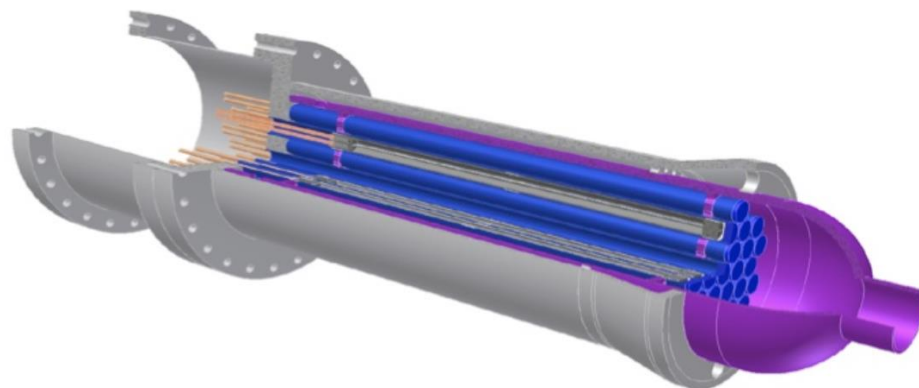
Figure 1.7: Reactor core simulator used at GRC showing the configuration of the fuel elements within the core and the coolant outlet [20].

The state of a nuclear reactor is determined by the stability of the chain fission reactions. A reactor is in a critical state when the free neutron production rate by fission reactions equals the rate of neutrons lost due to absorption by non-reactive atoms in the core or by leakage out of the reactor. The critical state is the reactor's steady-state. The supercritical state is one in which the free neutron production rate exceeds the consumption/loss rate. Finally, the subcritical reactor state occurs when the number of free neutrons lost exceeds those produced. Supercritical states occur during start up when ramping up to steady-state, while subcritical occurs during shut down or before start-up. Reactors should be in the subcritical state before and during launch to minimize the risk of releasing harmful radiation into the environmental in case of an accident. The reactor should only be brought to the critical state once in orbit or traveling away from Earth.

Gamma rays and neutrons can leak from the reactor and are hazardous to biological systems and electronics, therefore the reactor must be shielded. Heavy shields are installed between the reactor and the rest of the spacecraft to provide protection from the reactor's harmful byproducts. For an unmanned mission, the shield must provide neutron and gamma attenuation factors of about 10^6 [21].

1.2.4.2 Electric Power Generation

Both static and dynamic power conversion mechanisms have been considered for space nuclear power systems. All of the existing nuclear-powered spacecraft (i.e., Russian radar ocean reconnaissance satellites, NASA's SNAP-10A, Voyagers, New Horizons, etc.) utilized static converters, which generate electricity by using a temperature gradient to move charges. There are two types of static generators: thermoelectric and thermionic. In a thermoelectric generator a voltage is created at the junction between two dissimilar materials that drives current flow, similar to thermocouples. Figure 1.8 gives a schematic of a thermoelectric generator, where the dissimilar materials are N- and P-type

semiconductors. N-type semiconductors use electrons as negative charge-carriers and P-type use holes as positive charge-carriers, which provide opposite current flows as indicated by the yellow arrows.
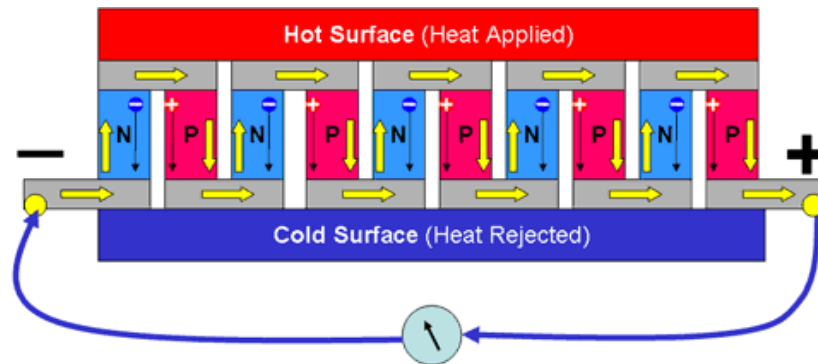
Figure 1.8: Schematic of thermoelectric generator [22]

In a thermionic generator, electron emitting and absorbing surfaces, or electrodes, are positioned facing each other and separated by a small gap. When the electron-emitting surface is heated, electrons evaporate and are absorbed by the other surface. The emitting and absorbing surfaces are connected in a loop to recharge the emitting side, see Figure 1.9. Thermoelectric and thermionic generators are termed 'static' since there are no moving parts. Static systems typically produce high currents and low voltages, therefore are considered for low-power applications (i.e. not for electric propulsion). Thermoelectric and thermionic systems operate at higher temperatures than existing dynamic generators, with cold-side temperatures around 800-900 K [23].
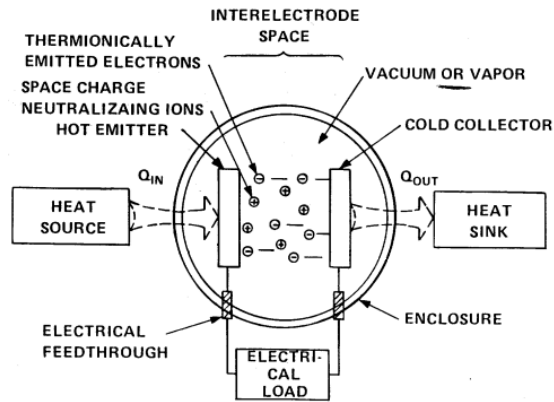
Figure 1.9: Schematic of a thermionic generator [24].

One disadvantage of passive power converters is lower thermal efficiency compared to dynamic converters. The thermal efficiency of the SNAP-10A thermoelectric power system reached only about 1.6% [25]. The nuclear-powered Russian spacecraft TOPAZ generated 5 kWe of power with a thermionic generator, and achieved a thermal efficiency of around 3% [25]. One of NASA's better-performing thermoelectric generators produced 100 kWe of electric power from 2.3 MWt of thermal power, an efficiency of 4.35% [11]. The typical power level achieved in a static system is too low to generate the thrust required for high-speed deep-space missions. For these reasons, much of the current work in power conversion technologies is focused on dynamic options.

Dynamic power conversion systems, or heat engines, convert heat into mechanical work, used to generate electricity. To obey the second law of thermodynamics, a heat engine generating work must operate between two temperature reservoirs, one from which it gains heat and one to which it rejects heat. In a closed cycle heat engine, a working fluid undergoes several processes and returns to its original state. The process steps typically include heat addition (expansion generates work), heat rejection (condensing or compressing), and a pump (absorbs work to restore fluid pressure). This process produces a net amount of mechanical work that is converted to electricity in an alternator.

Cycle performance is evaluated on the amount of input energy required to produce a desired energy output. The maximum theoretical cycle efficiency, called the Carnot efficiency, is based on a

reversible cycle operating between two temperature reservoirs. The Carnot efficiency is always less than 100% and greater than the real efficiency of a cycle operating between the same two temperatures, as given by:

$$100\% > \eta_{Th,Carnot} = \frac{T_H - T_C}{T_H} > \eta_{Th,real} = \frac{W_{net}}{Q_{in}} \qquad (1\text{-}1)$$

Where T_H and T_C are the hot-side and cold-side temperatures of the cycle. In an NEP system T_H and T_C are the operating temperatures of the reactor and radiator respectively, as shown in Figure 1.10.
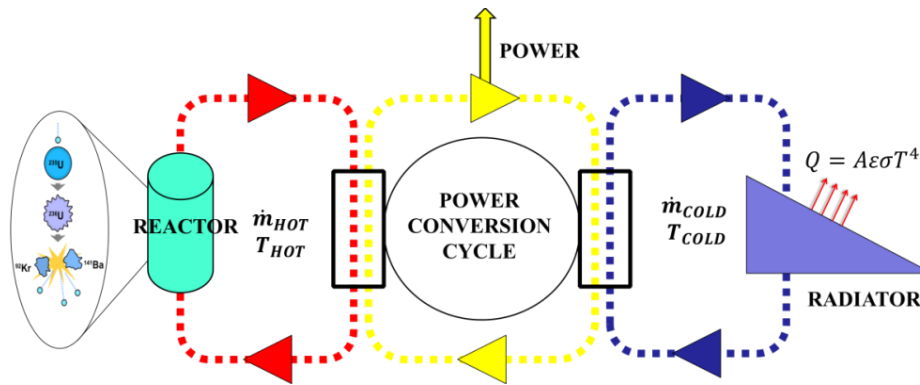
Figure 1.10: Schematic of the power subsystem for NEP.

The two most advanced options for power converters for nuclear-electric systems are the Closed Brayton Cycle (CBC) and the Free-Piston Stirling (FPS) cycle [26][27]. There are several other lower TRL power conversion options that NASA has evaluated for nuclear-electric space applications including the Rankine cycle [20]. The Brayton cycle consists of a compressor and turbine running on the same drive shaft, and two heat exchangers for absorbing and rejecting heat, as shown in Figure 1.11. The 100 kWe power conversion system (PCS) for the Jupiter Icy Moon Orbiter (JIMO) concept ran on a CBC, which has been used for several subsequent studies on nuclear power in space [26][28]. The CBC was selected for this application because of its high efficiency and power capabilities [27]. CBC converters optimize at efficiencies around 20-25% for cold-side temperatures in the range of 400-600K [26].
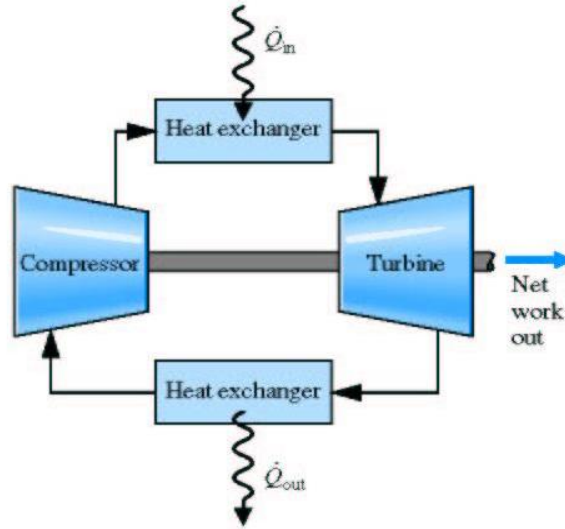
Figure 1.11: Standard Closed Brayton Cycle, after [29]

The Stirling engine has been considered for several in-space power applications including designs for a 40kWe nuclear power system on the surfaces of Moon and Mars [20]. Free-Piston Stirling engines consist of a piston and a displacer in parallel as shown in Figure 1.12. When gas contained at the top is heated for a short period the displacer is forced toward the piston, which compresses the gas in between and forces the piston down. When the heat source at the top is turned off, the pressure of the gas at the top decreases pulling the displacer back up. Then the gas in between the piston and displacer is cooled for a short period reducing pressure of that gas, which forces the piston back to its original position. The cross section picture shows that electricity is generated as the piston rod moves in and out of an electric field each cycle. Since FPS engines have fewer moving parts than other engines, they experience less wear and a potentially longer lifespan.
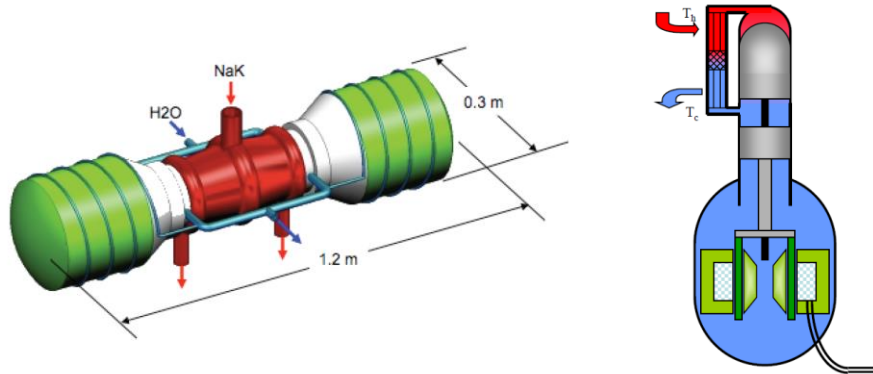
Figure 1.12: Left: Dual-opposed linear alternator FPS engines developed at NASA Glenn Research Center [20]; Right: Cross-section of one engine, heat addition on top near the displacer and electrical power output from the bottom [30]

Figure 1.13 provides a comparison of the specific mass (kg/kWe generated) for dynamic and static power conversion options over a range of power levels. This shows that the Brayton engine provides the best specific mass for the 100kWe, but Rankine engines provide superior specific mass at higher power levels. The Rankine may be of interest for far-term missions requiring megawatts of power.
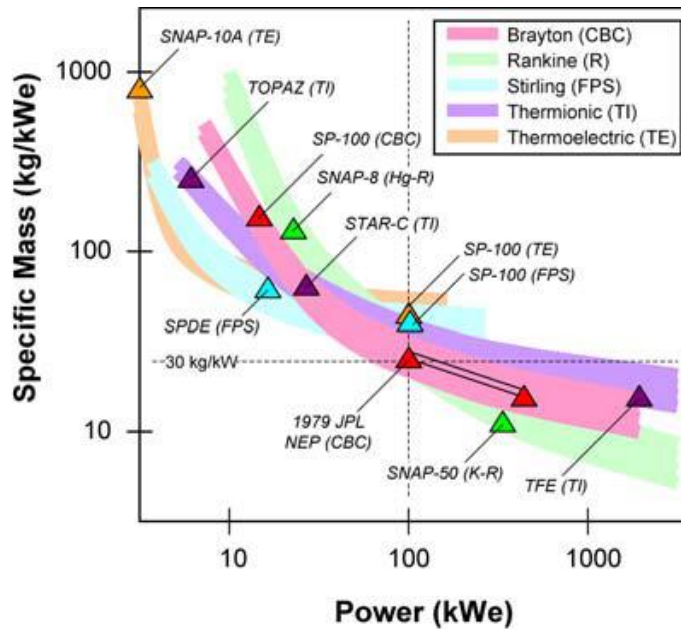
Figure 1.13: Comparison of power conversion systems over a range of power levels [31].

1.2.4.3 Coolant

Coolant is the heat transport fluid between the power conversion cycle and both the heat source and sink. Different coolants can be used on the hot and cold sides of the system since they are typically separate pumped loops. A good coolant has high specific heat capacity and thermal conductivity, appropriate melting and boiling temperatures so that it remains in the desired phase during operation, and has good chemical and radiation compatibility with all interfaces. A fluid with high thermal conductivity (k, W/(m-K)) and specific heat capacity (c_p, J/(K-kg)) requires reduced pumping power since the fluid can quickly absorb a large amount of heat (due to k) with a small increase in temperature (due to c_p).

Common coolants include water, ammonia, and liquid metal (potassium and sodium, or their alloys), and sometimes gases such as carbon dioxide and helium. A very common coolant in systems operating above 300 K is the eutectic sodium-potassium mixture called NaK, which is about 78% potassium and 22% sodium [20][32], and can be used with nuclear reactors, power conversion systems and many other heat transport applications. As with many liquid coolants, NaK has a high specific heat capacity and thermal conductivity, but its primary advantage is liquidity over a wide temperature range, with a melting point of 262 K and boiling point of 1058 K [32]. Liquid metal coolants can be driven by electromagnetic pumps, a major benefit for space applications because electromagnetic pumps have no moving parts and are therefore more reliable than their dynamic counterparts [20].

1.2.4.4 Thrusters

Thrusters are the devices that repel mass from the spacecraft creating thrust, or reaction forces in the direction of travel. Traditional chemical thrusters repel high-speed combustion products through a nozzle. As indicated previously, generating thrust this way is highly inefficient because the fuel has a low energy density. The benefit of chemical thrusters is that they can provide very high impulse, which

is required to escape Earth's gravity and atmosphere, but is not necessary for in-space travel where

gravitational and drag forces are very low. Once in space, continuous, low levels of thrust over time can

provide large increases in velocity. While in-space electric thrusters require more time to provide the

same change in velocity as chemical thrusters, they provide significant fuel and system mass savings.

Since electric thrusters are far more efficient and lightweight than chemical thrusters, they can be used

continuously for longer durations while consuming much less propellant, and therefore achieve higher

speeds. For these reasons, electric thrusters are desirable for deep-space probes.

Within the class of electric thrusters, there are three main types: electrostatic, electrothermal

and electromagnetic. Table 1.1 provides performance parameters for various thruster types, showing

that electrostatic (ion and Hall) types operate at high efficiencies and can generate large specific

impulses compared to chemical and other electric thrusters [33].

Table 1.1: Typical operating parameters for thrusters with flight heritage [33]

Thruster	Specific Impulse (s)	Input Power (kW)	Efficiency Range (%)	Propellant
Cold gas	50–75	—	—	Various
Chemical (monopropellant)	150–225	—	—	N_2H_4 H_2O_2
Chemical (bipropellant)	300–450	—	—	Various
Resistojet	300	0.5–1	65–90	N_2H_4 monoprop
Arcjet	500–600	0.9–2.2	25–45	N_2H_4 monoprop
Ion thruster	2500–3600	0.4–4.3	40–80	Xenon
Hall thrusters	1500–2000	1.5–4.5	35–60	Xenon
PPTs	850–1200	<0.2	7–13	Teflon

The leading options for electric thrusters are ion and Hall thrusters (both electrostatic). The US

and Russia have each used over one hundred electric thrusters in communications satellites, and many

more in deep-space missions. Hall thrusters have been used on 48 spacecraft since their first mission on

a Russian vehicle in 1971 [33]. Japan launched the first ion thruster in 1995 [33], and NASA followed

with the Solar Electric Propulsion Technology Applications Readiness (NSTAR) 2.3 kW ion thruster on the Deep Space 1 probe launched in 1998, whose primary mission was to test ion propulsion as the primary propulsion during an interplanetary mission [34].

Ion thrusters generate plasma that ionizes the propellant. The positively-charged ions are electrostatically extracted and accelerated to high velocities using high voltage (10kV) electrode grids as shown in Figure 1.14 [33]. The NSTAR thruster ejected ions at velocities of 30 km/s (62,900 mph) [35]. Ion thrusters provide the highest efficiency, up to 80%, of the electrostatic thrusters [33]. Hall thrusters use the Hall Effect to generate plasma from which ions are electrostatically accelerated using orthogonal electric and magnetic fields, as shown in Figure 1.15 [33]. Ion thrusters have higher efficiency, complexity and cost than Hall thrusters, which are tradeoffs that make each a better choice for different missions [36]. For missions that require a large change in velocity, ion thrusters are the better choice, whereas complexity and cost savings make Hall thrusters the better choice when low or moderate velocity changes are needed. Figure 1.16 shows commercially available ion and Hall thrusters. The preferred propellant for both ion and Hall thrusters is the high atomic weight and inert gas xenon. For an order of magnitude perspective on the propellant consumption rate of an electric thruster, the ion thruster on Deep Space 1 mission expended 73.4 kg of xenon over 16,265 hours of operation to achieve a velocity change of 4.3km/s (approximately 10,000 mph), and for 2000 of those hours the specific impulse was 2200 s and the consumption rate was less than 4 g/hr [37].
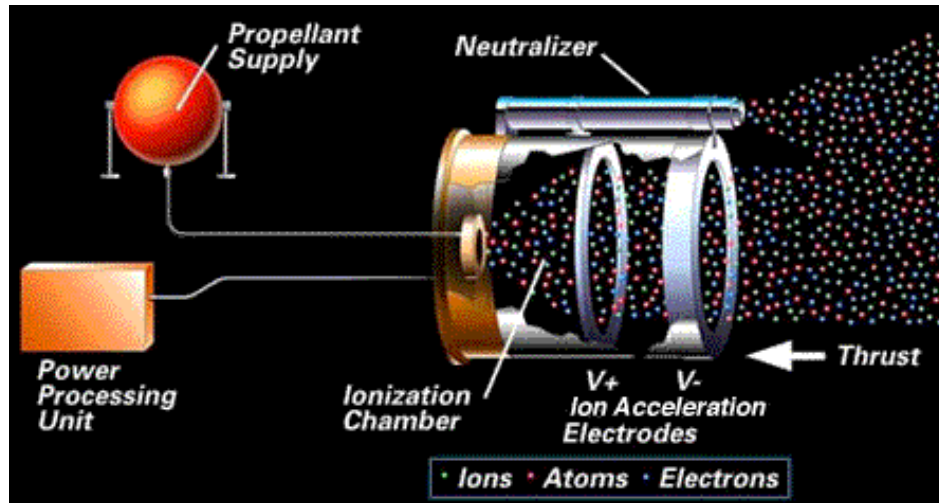
Figure 1.14: Schematic of NSTAR ion thruster, validated on the Deep Space 1 mission [35]
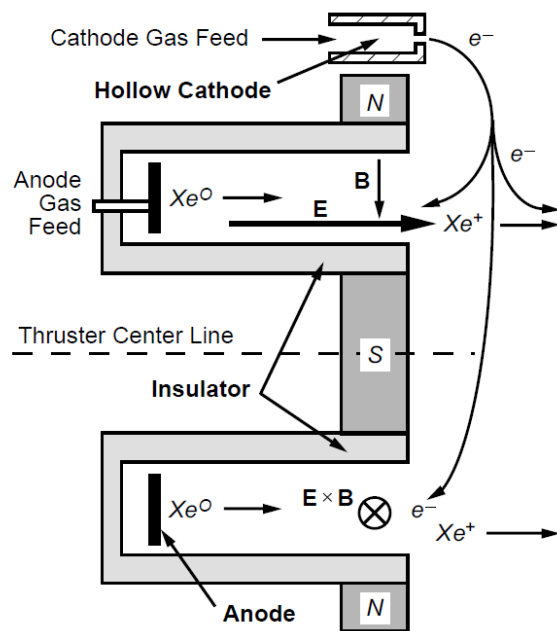
Figure 1.15: Schematic of a Hall thruster with Xenon propellant [33]
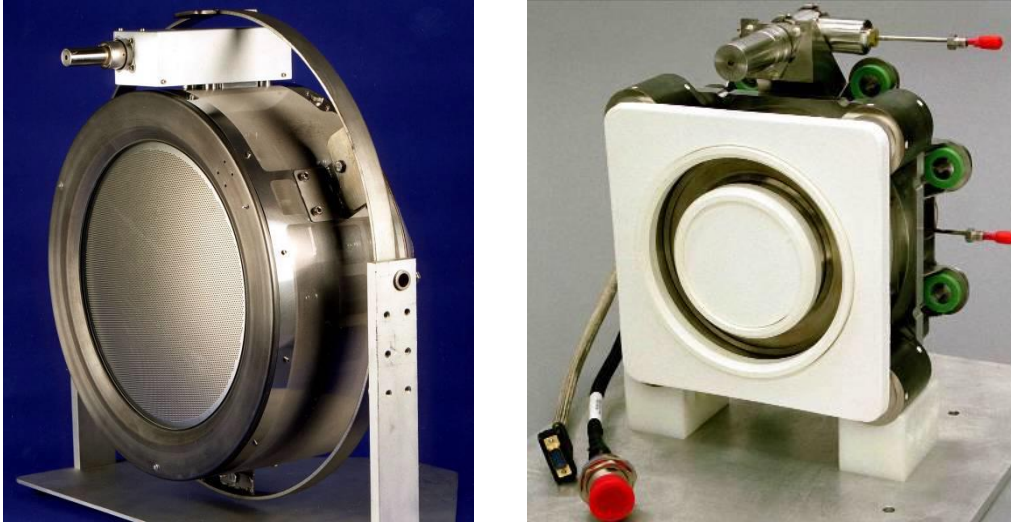
Figure 1.16: Commercially available thrusters from Aerojet: 2.3 kW ion thruster (left) and 4.5 kW Hall thruster (right) [36]

Most ongoing research on electric thrusters is conducted at NASA's Glenn Research Center and

Jet Propulsion Laboratory, and at Hughes Electron Dynamics [33].

1.2.4.5 Heat Radiators

Radiators reject the waste heat from the power generation process. Chemical propulsion does

not require the same type of heat rejection system because most of the heat is rejected as hot exhaust.

As shown in Figure 1.6, the waste heat from the power conversion cycle is absorbed by a heat transport

loop in a heat exchanger and is ultimately rejected to space by a radiating surface. Radiating surface

area is required since there is no other heat transfer mechanism to space; therefore all space-radiator

designs need exposed and emissive surfaces. The necessary radiating area is dictated primarily by the

operating temperature of the cold-side heat transport coolant and the amount of waste heat.

Throughout the evolution of space heat rejection systems, the major improvements have

targeted efficiently of heat transport to the radiating surface and are summarized in Figure 1.17. The

original deployable radiators, used on the Space Shuttle vehicles, used a fully pumped system of heat

transport pipes that interfaced with the radiator panels, as shown in Figure 1.17 on the left. This design

required significant pumping power and was vulnerable to failure since the entire system pressure could

be lost due to the failure of a single pipe. The following generations of heat transport included a

primary pumped loop that interfaced with heat pipes in a heat exchanger. The heat pipes would

efficiently transport heat along their lengths to the radiating panels. Heat pipes are designed to

maintain near-isothermal conditions along their lengths, which aids in high-efficiency heat transfer to

the radiating fins. Each heat pipe is independent from the others and from the coolant loop, so the loss

of one heat pipe results in only a minor loss in system efficiency, which significantly decreases the

system vulnerability as compared with fully-pumped coolant loops.
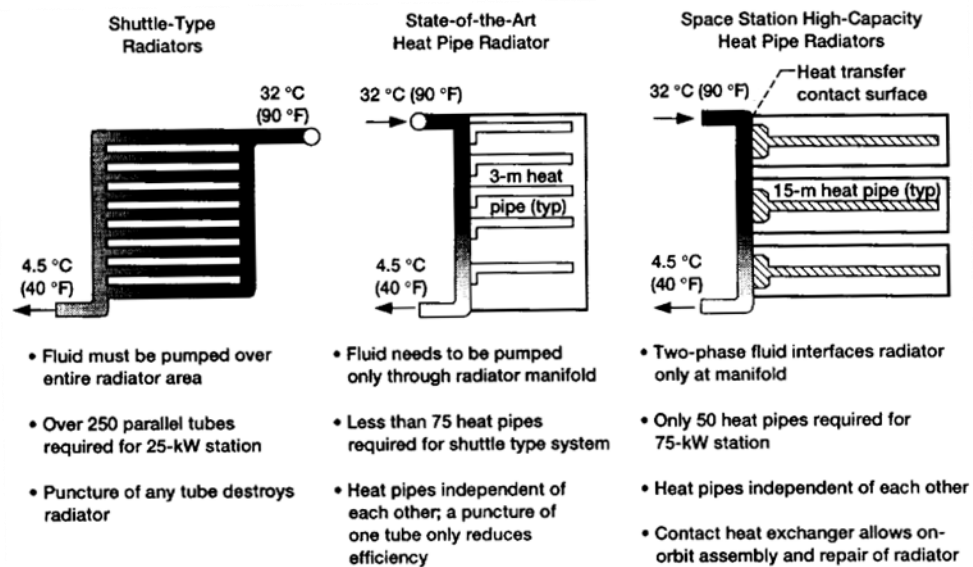
Figure 1.17: Summary of the evolution of heat transport systems in space-radiators, from mid-1970s to
early 1990s [38]

In addition to the heat transport loop and heat pipes, the other major element of the heat

rejection system is the radiating fins. To date, radiating fins have been designed using either metal or

composite facesheets. The fin construction should maximize the heat conduction from the surface of

the heat pipe to the bulk fin material. Thus, the thermal resistance of any intermediate layers for

bonding the heat transport system to the panels should be minimized. Aluminum is the primary metal

used in radiator panels because of its low density and high thermal conductivity. One advantage of

using metal fins is that metal can be easily shaped to wrap tightly around the heat pipes as shown in

Figure 1.18-A, which provides good contact area and only needs a thin bonding layer. Composite panels

are either polymer or graphite matrix with carbon fiber reinforcement depending on the operating

temperature, and are generally very stiff. The standard construction of a composite panel is given in

Figure 1.18-B, which consists of several bonding layers in between the heat pipe and the panel surface.

The extra layers are required to securely fasten the flat panel to the round pipe, but add extra thermal

resistance. The development and performance of various panel types will be discussed later.
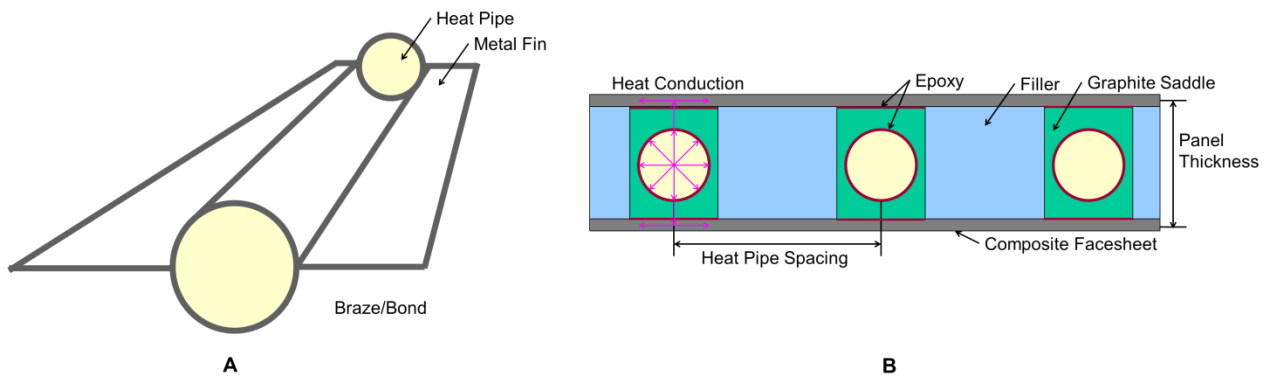
Figure 1.18: Cross sectional views of typical metal (A) and composite (B) radiator panels, after [20]

1.2.4.6 Heat Pipes

Heat pipes are closed, two-phase flow devices that can passively transfer large quantities of

heat between two locations without electrical power. Figure 1.19 gives a schematic of the basic

components of a heat pipe. The pipe is generally hollow except for a wick against the wall and working

fluid. Inside a heat pipe, working fluid in the liquid phase adheres to the wick lining the pipe walls, while

the vapor phase fills the remaining volume of the pipe. In space, the liquid phase will adhere to the tube

walls without a physical separator due to surface tension forces. When heat is added to one end of the

pipe (evaporator section), liquid absorbs the energy through evaporation. Relative to the condenser,

the evaporator end has a lower liquid fraction, which creates a pressure gradient across the length of

the wick, and capillary forces draw liquid toward the hot end. The evaporating fluid creates a region of

higher pressure vapor, thus driving vapor flow toward the condenser region. In the condenser region, the vapor condenses and refreshes the liquid wick.
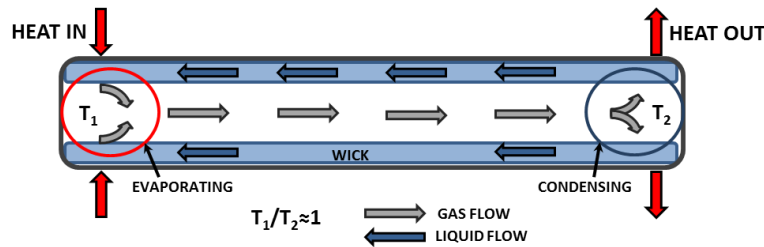
Figure 1.19: Schematic of a two-phase heat pipe

The working fluids selected for heat pipes have high latent heat of vaporization so only a small amount of fluid is required to transport a significant amount of heat between ends. The temperature difference between the evaporator and condenser does not have to be large to induce capillary pumping, therefore heat pipes are nearly isothermal. The heat pipes developed for lower temperature applications around 400 K are typically constructed with titanium pipes and water as the working fluid [20]. For higher temperatures near 600°C heat pipes must be fabricated with higher melting point materials such as Inconel for the pipe and sodium or potassium for the working fluid.

1.2.4.7 System Integration and Tradeoffs

Each of the aforementioned components of the power subsystem have been studied and optimized independently for various applications, but a successful system will utilize the components in an optimal way for the mission depending on specific objectives and constraints. The trade space between spacecraft components with respect to performance, mass, and configuration is complex and only several of the relevant trades to heat rejection are listed below. Specific case studies will be presented in following sections.

- Higher cold-side operating temperatures benefit from the fourth power temperature radiation law, such that the radiator area may be reduced.

- A heat engine with a lower temperature ratio (T_H/T_C) allows the cold-side temperature to be higher, thus the radiator area is reduced; yet a higher temperature ratio yields higher thermal efficiencies: $\eta_{Th,Carnot} = 1 - \dfrac{T_C}{T_H}$

- Increasing the operating temperature requires more waste heat rejection in order to maintain a specific thermal efficiency.

- Operating at higher temperatures may require advanced materials to withstand the thermal load over time (i.e. added development and materials cost and risk).

- Heat transport loop flow rate tradeoffs: higher flow rate yields lower temperature difference between the ends of the radiator (along the evaporator length), but consumes more energy in pumping and fluid drag.

1.2.5   Related Studies

In this section, related studies and projects are discussed including the first US nuclear reactor in space on SNAP-10A, a large nuclear fission feasibility project called SP-100, the ISS deployable heat rejection system, the Advanced Radiator Concepts project, the Jupiter Icy Moons Orbiter (JIMO) NEP concept, and the on-going Fission Surface Power (FSP) project. JIMO and FSP are two of the largest studies on space nuclear-electric power and contain the most mature designs in the literature.

1.2.5.1 Systems for Nuclear Auxiliary Power, mission SNAP-10A

The 10A mission was the SNAP program's first and only US mission using a nuclear reactor. The nuclear reactor provided heat for a thermoelectric generator that produced 600 W of electric power with an efficiency of about 1.4% [25]. The cone-shaped heat rejection system had a pumped heat transport loop integrated into radiator panels. Liquid sodium coolant was used in the power system because it melts at 208°F, has good heat transfer properties and can be driven by electromagnetic

pumps. The launch and reactor startup were successful, but SNAP-10A shut down after 45 days in orbit due to a failed voltage regulator that shut down the core [16]. SNAP-10A and all of the nuclear reactor-powered Russian satellites were designed to remain in Earth's orbit indefinitely because of the hazards of reentering radioactive material [11].

1.2.5.2 International Space Station (ISS)

The ISS radiators are relevant because they are an established technology. The radiators on the ISS and Space Shuttle are for general thermal management and operate at low-temperatures around 300-350 K. The panels consist of a fully-pumped heat transfer distribution system with ammonia working fluid, aluminum faceplates and honeycomb fill [20]. These materials are lightweight and readily available, but are limited to low-temperature applications. The panels are deployable to accommodate varying heat rejection needs using a scissor mechanism to achieve a maximum radiating surface area of 85 m^2. The areal mass of the system including the panels, fluid loop and deployment mechanism is 8.8 kg/m^2, which does not meet NASA's performance targets for interplanetary probes [20][21]. The panels alone have an areal density of 2.75 kg/m^2. Figure 1.20 shows the deployed ISS radiators
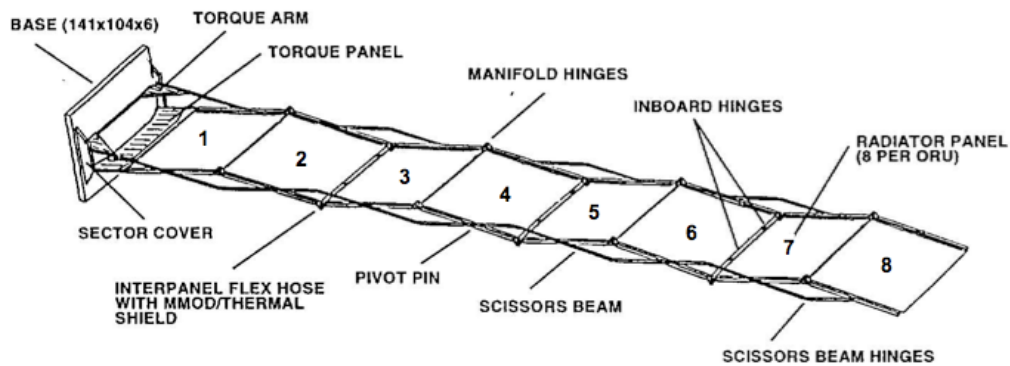
Figure 1.20: Deployed ISS heat rejection system [20]

1.2.5.3 Space Power Program, SP-100

The SP-100 was a NASA program to study in-space nuclear fission power that ran from 1983 to 1994. This program studied power conversion systems including 100 kWe thermoelectric generators, Closed Brayton and Free-Piston Stirling cycles, as well as heat pipe radiators, and NaK heat transport loops. The applications considered in SP-100 included deep space probes and power for Martian/lunar surface habitation [39]. The program was cancelled in 1994 because nuclear-electric power had not yet been incorporated into any specific NASA missions [40].

Figure 1.21 shows one SP-100 concept with a nuclear reactor, thermoelectric generator, and electric propulsion on a spacecraft. The generator's cold-side temperature was 800 K, the heat rejection load was 2,200 kWt, and the radiator area was 106 m^2 [11]. The high cold-side temperature allowed for a relatively small radiator (compare with JIMO's large low-temperature radiator in Figure 1.28). The radiator design utilized carbon fiber reinforced graphite composite fins that had an areal density of about 3 kg/m^2 [38].
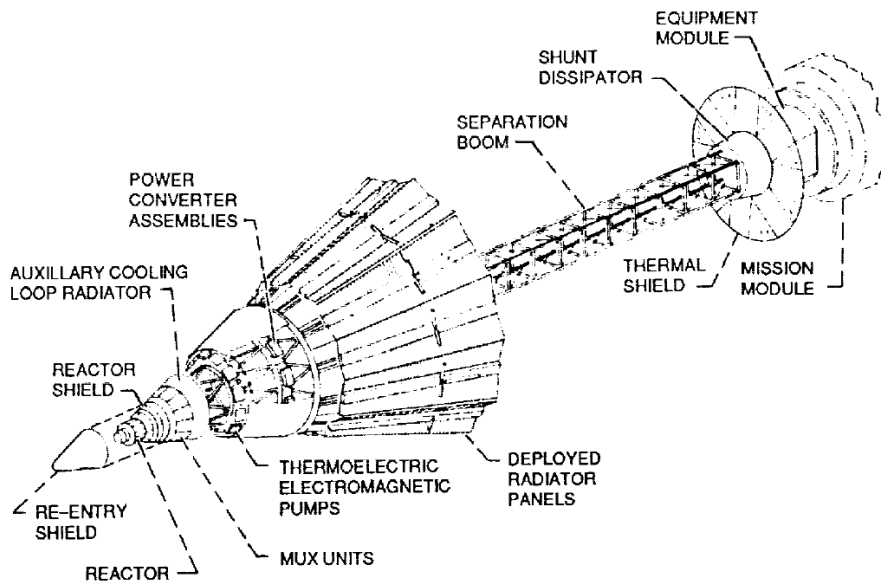
Figure 1.21: SP-100 power system on a spacecraft [39]

Another SP-100 study evaluated power system designs for lunar base applications. Free-Piston

Stirling engines were selected because of their high thermal-to electric efficiency, low-risk due to few

moving parts, and a low temperature ratio (T_H/T_C) that allows for smaller radiators [39]. Figure 1.22

gives the results from a trade study on this design. These results show the system mass sensitivity to

the net power output and hot-side temperature keeping thermal efficiency constant. The variance

between the two curves is due to differences in the radiator mass because operating at higher

temperatures substantially reduces radiator mass.
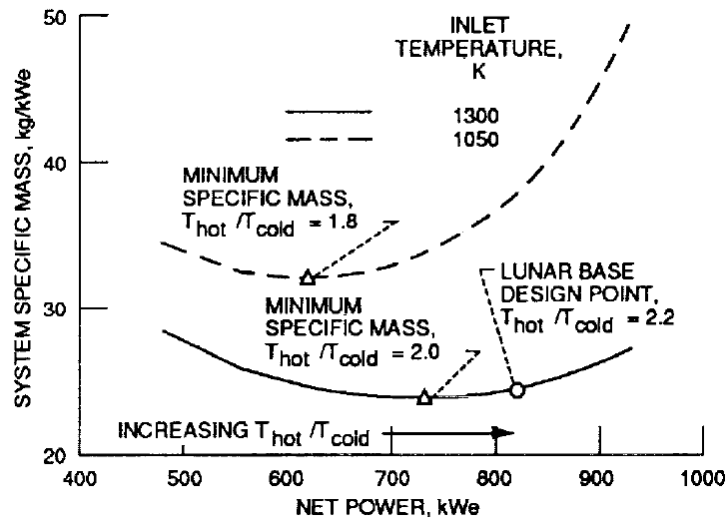
Figure 1.22: Power system mass sensitivity to Stirling engine inlet temperature (T_{hot}) [39]

Within the broadly-scoped SP-100 program, many different systems were considered and while

no missions resulted directly from the effort, many of the technologies were used in later research.

1.2.5.4 Advanced Radiator Concepts Project

The Advanced Radiator Concepts (ARC) was a NASA project closely tied with the SP-100 program

to develop improved, light-weight heat rejection systems for several power options including Free-

Piston Stirling engines and thermoelectric generators. During this project many unconventional designs

were evaluated. Juhasz, *et. al.* presented a review of the radiator concepts developed for this project

describing over ten vastly different designs utilizing complex dynamic systems and untested mechanisms

[38]. Several radical radiator designs included the liquid belt, liquid droplet, roll-out fin, rotating film,

Curie point, and rotating bubble membrane among others [38]. Figure 1.23 through Figure 1.25 below

show several of these concepts.
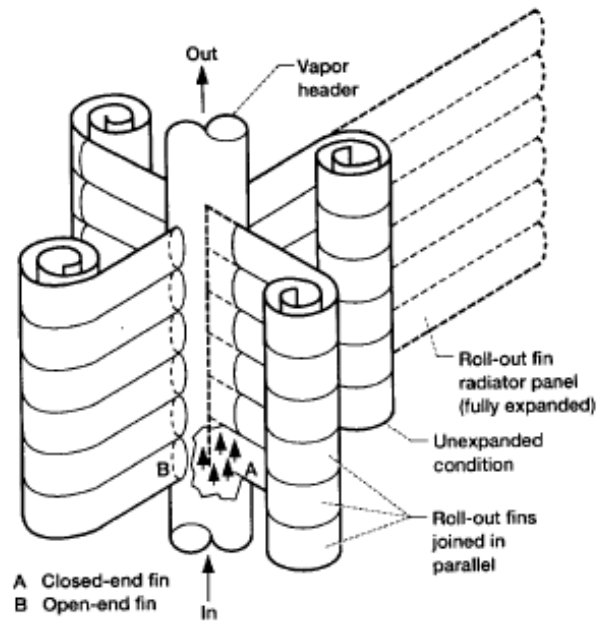
Figure 1.23: Roll-out fin expandable radiator panel concept [38]
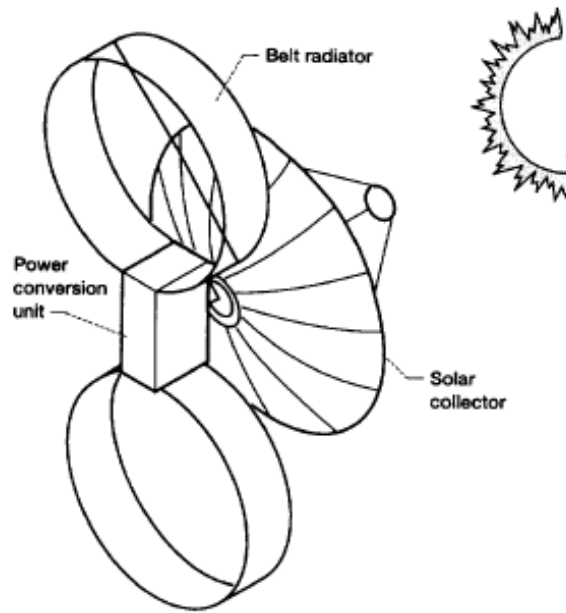
Figure 1.24: Moving belt radiator concept [38]
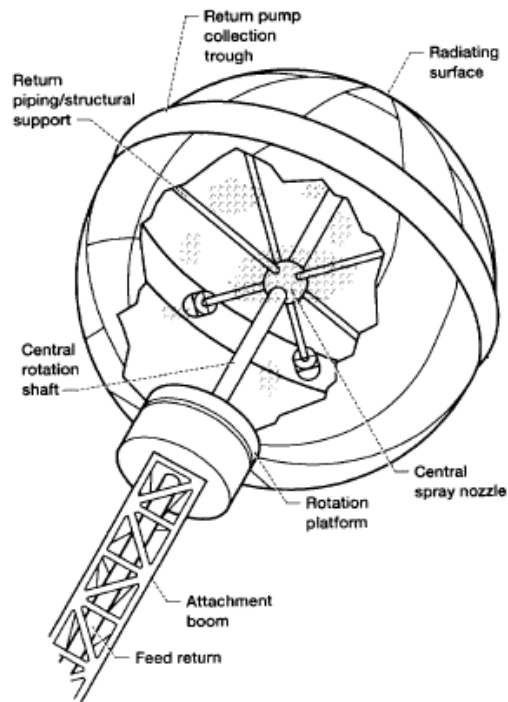
Figure 1.25: Bubble membrane radiator concept [38]

One of the more viable designs from the ARC project was the carbon-carbon tube and fin design that was used in the SP-100 nuclear thermoelectric vehicle concept [51]. This radiator was designed for operational temperatures in the range of 600 to 875 K, consisted of metal heat pipes with potassium working fluid that directly interfaced with composite fins as shown in Figure 1.26. Wrapping the composite material around the heat pipe facilitated good heat conduction to the fins and a low areal mass of 2.1 kg/m^2 [27].
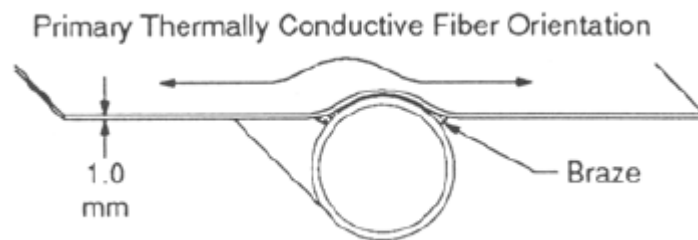
Figure 1.26: Metal heat pipe with a wrapped carbon-carbon fin [41]

This design was tested and matured to a moderate development stage. Denham, *et. al.* conducted tests with these carbon-carbon composite fins at 600 and 850 K using various types of carbon fiber, heat pipes (stainless steel, titanium, and niobium), and fin attachment methods [41]. The carbon fibers had thermal conductivities ranging from 450-850 W/(m-K) during tests at 300 K. The fins were attached to the heat pipes using a braze called Ticusil (a titanium-copper-silver alloy), which melts and creates an alloy bond between the two components. The primary challenge with fin attachment was delamination of the composite caused by high stresses generated in cooling the sample from the braze metal melt temperature, and resulted from differences in the coefficients of thermal expansion of the braze and composite. The combination of no near-term missions requiring high-temperature radiators and fabrication challenges halted further development of the carbon-carbon composite fins.

1.2.5.5 Jupiter Icy Moon Orbiter (JIMO)

The JIMO mission was the first mission concept of the Prometheus Project, the first large-scale

NEP design effort to enable outer solar system exploration [42]. The Prometheus Project ran from 2003

to 2005 when its funding was cut in large part due to NASA's shifting priorities toward manned, near-

Earth missions [42]. The NEP design included a 100 kWe Closed Brayton Cycle and either ion or Hall

thrusters [26]. A block diagram of the JIMO spacecraft is given in Figure 1.28. One of the major

technical limitations of this concept was the size of the heat rejection system, as shown to scale in

Figure 1.29.
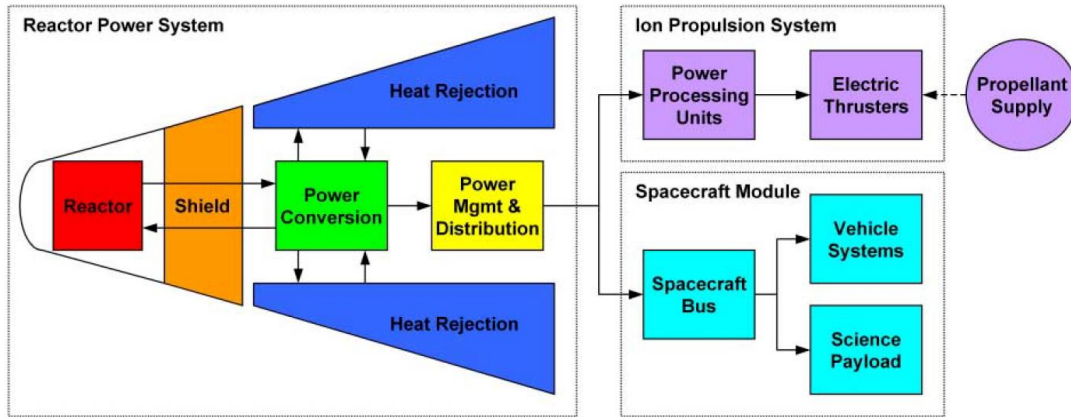
Figure 1.27: NEP block diagram [27]
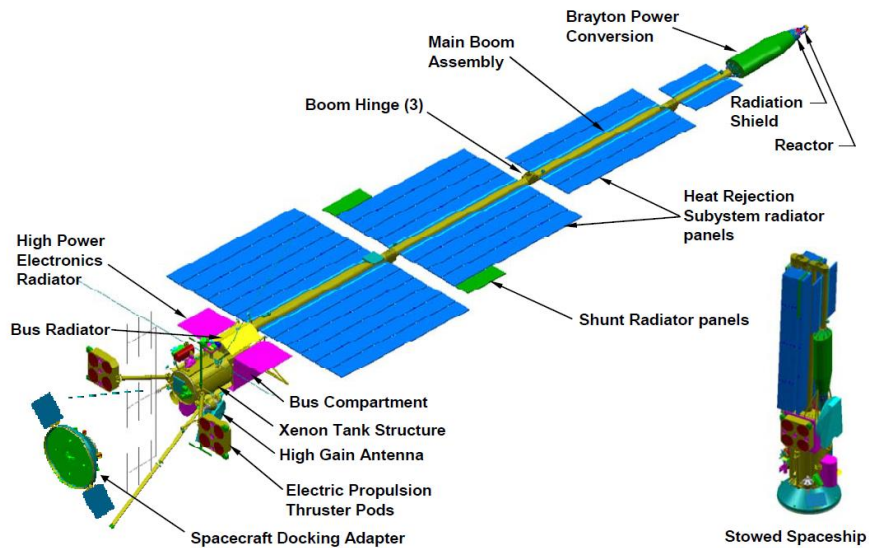
Figure 1.28: Conceptual design for JIMO [42]

The SP-100 and ISS radiators strongly influenced the JIMO heat rejection system design. The JIMO heat rejection system operated in the range of 400-600 K and consisted of a pumped NaK heat transport loop and deployable radiator panels constructed of titanium-water heat pipes and carbon-carbon composite facesheets bonded to the heat pipe using epoxies. Epoxy bonding did not have the same delamination challenges as the braze joining methods used the high-temperature applications [27]. The radiator panel cross-section was similar to that in Figure 1.18-B. A 25-ft truss supported the

panels and NaK loop. The heat transport loop interfaced with the heat pipes in a simple rectangular

heat exchanger as shown in Figure 1.29 [34]. The total radiator area was 170 m^2, and the mass including

the panels, heat transport loop plumbing and deployment mechanism was 854 kg, or 5 kg/m^2. The mass

of the scissor deployment mechanism was estimated by taking 30% of the panel mass, which was the

approximate fraction of the ISS system and assumed to be reasonable for similar applications. The

radiator made up approximately 30% of the power conversion system mass [27][42].
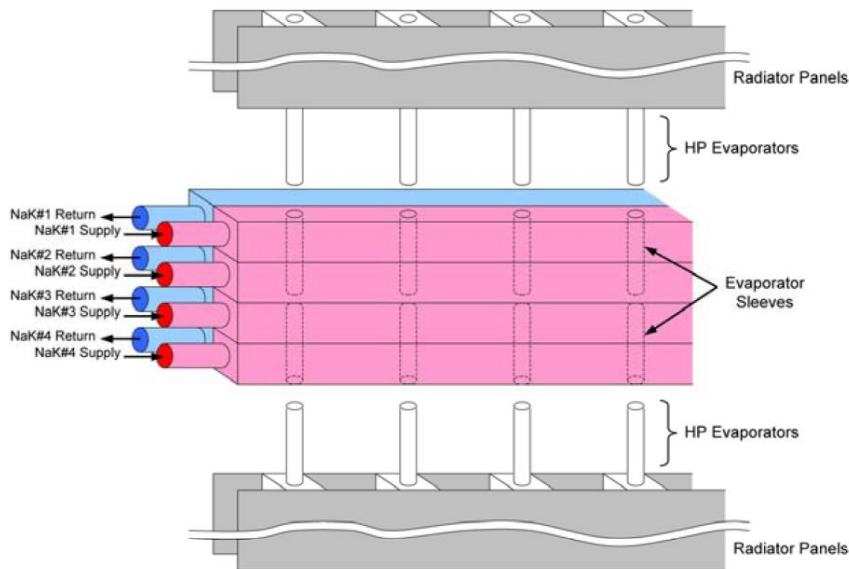
Figure 1.29: Heat exchanger between the main heat transport loop (NaK) and the heat pipes embedded
in the radiator panels [26]

Higher operating temperatures were not utilized in the JIMO study because of the cost and risk

associated with developing and using advanced materials such as refractory alloys. Refractory metals

are typically highly resistant to heat and wear, with melting temperatures above 2000°C. Mason *et. al*.

estimated a 55% reduction in radiator area by increasing the JIMO hot-side temperature by 300 K [27].

This mass-saving potential may motivate future development of higher-temperature applications.

1.2.5.6 Fission Surface Power (FSP)

Once JIMO was cancelled, space nuclear fission efforts were focused on surface power applications for lunar or Martian outposts. The FSP project started in 2006 and most ongoing work is conducted at NASA's Glenn Research Center (GRC). One of the project objectives is to create affordable, low-risk designs, which have replaced minimizing mass and maximizing system performance as top priorities [20]. Nuclear electric power is recognized as a necessary technology for long-term outposts that cannot depend exclusively on solar energy due to long durations shadowed from the sun. Since mass is less of a constraint for surface applications than on spacecraft, some power system components are different from JIMO's including the use of heavier Free-Piston Stirling engines because they have fewer moving parts, so they are potentially more reliable than CBC's [20]. Much of the JIMO radiator design, however, was used in the FSP project [26]. The FSP heat rejection system with its motor-driven scissor mechanism is shown in Figure 1.30.
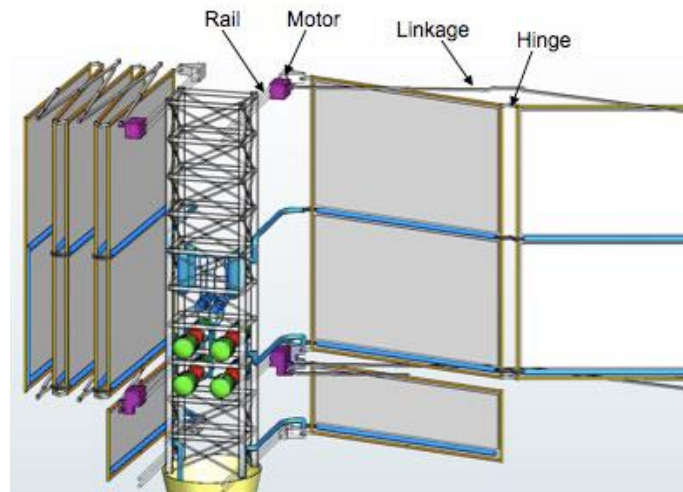
Figure 1.30: FSP radiator panels and deployment mechanism [20]

Radiator development at GRC is focused on advanced heat pipes and composite fin construction. The selected heat rejection design temperature is around 400 K, compatible with current low-power nuclear-electric conversion systems [20][43][44]. The radiator fins at GRC consist of an

epoxy matrix, carbon fiber composite facesheet bonded to a POCOFoam® (POCO) saddle that is bonded

to the heat pipe. Epoxy is used to bond each layer, and the POCO is used to transition between the

curved geometry of the heat pipe and the flat facesheet and facilitate heat conduction. POCO is a

structural graphite foam with aligned graphitic ligaments within the walls and is used because it has a

relatively high thermal conductivity of 379 W/(m-K) in the ligament orientation [45]. The facesheets are

coated with a polyurethane paint with an emissivity of 0.89 [45]. Technology demonstration units of

this radiator concept have been constructed and are currently undergoing tests. Figure 1.31 shows the

second generation radiator demonstration unit in position for testing in the GRC Vacuum Facility #6.

Figure 1.31: Second generation Radiator Demonstration Unit (approx. 3 ft by 5 ft) in GRC Vacuum Facility
#6 [45]

1.2.5.7 Radiator Studies Summary

Improving radiator fins has been an ongoing objective for NASA since the 1980's alongside the

development of heat transfer loops and heat pipes. NASA's design considerations for just the radiator

include: specific heat rejection performance, reliability, technology readiness, life expectancy, system

complexity, required area, panel configuration, life cycle cost, and micrometeoroid vulnerability [38].

Optimizing radiator designs with all of these criteria, some of which are difficult to quantify, can lead to many varied designs depending on the objectives are prioritized. Yet over time, only several concepts have prevailed mostly due to simplicity and low development cost. The simple and proven 'fin and tube' radiator design has remained standard with slight changes as improved heat transport mechanisms and fin materials have developed.

As discussed previously, the heat transport mechanism has evolved from a fully pumped single-phase system to a pumped single-phase main loop with 2-phase heat pipes. The two basic types of fins that have been explored are metal and composite. Metal fins were used in earlier designs until lighter-weight composite materials were developed. Recent fin studies have focused on only composites, all of which use high thermal conductivity carbon fiber and various matrix materials including graphite and polymers.

Another main radiator design parameter is the operating temperature. Many radiator studies have investigated lower temperature (500 K or less) applications including the ISS and JIMO. There are no mature design concepts for high-temperature radiators because there have been few possible applications until recently. Notional high-temperature applications include NEP with heat rejection in the range of 400-800 K, and Magnetohydrodynamic (MHD) and alkali metal Rankine power conversion systems with cold-side temperatures exceeding 1000 K [1].

No existing high or low-temperature heat rejection system can meet NASA's areal density target of 2-4 kg/m^2. Table 1.2 provides a basic comparison of radiator fin materials that have been considered with the addition of bare carbon fiber, which is the focus of this work.

Table 1.2: Comparison of Fin Materials

Fin Material	Melting Point (°C)	Axial Thermal Conductivity (W/m-K)	Density (kg/m^3)
Aluminum	660	237	2712
Stainless Steel	1510	15	7500
Molybdenum	2620	138	10188
Carbon Fiber Composite	2000*	50-300**	1600-1980**
Carbon-Polymer Composite	<200	50-300**	1600-2000**
Bare Carbon Fiber	>2500	700-900**	1800-2200**

 * Typical Maximum Operating Temperature
 ** Depends on the construction

Figure 1.32 provides specific heat rejection data from three of the more mature radiator designs: JIMO Brayton system, SP-100 thermoelectric vehicle, and the SP-100 surface power Stirling system. Specific heat rejection curves for various fin materials and temperatures are overlaid on the plot. The specific heat rejection curves are shown in only the temperature ranges where that fin material can be used. This demonstrates the superior properties and potential of using bare carbon fiber fins. Figure 1.33 shows the same data on a log-log scale. A triangle whose hypotenuse has a slope of four is overlaid on the plot to show that these lines follow the fourth power temperature dependence as given in Equation 1-2
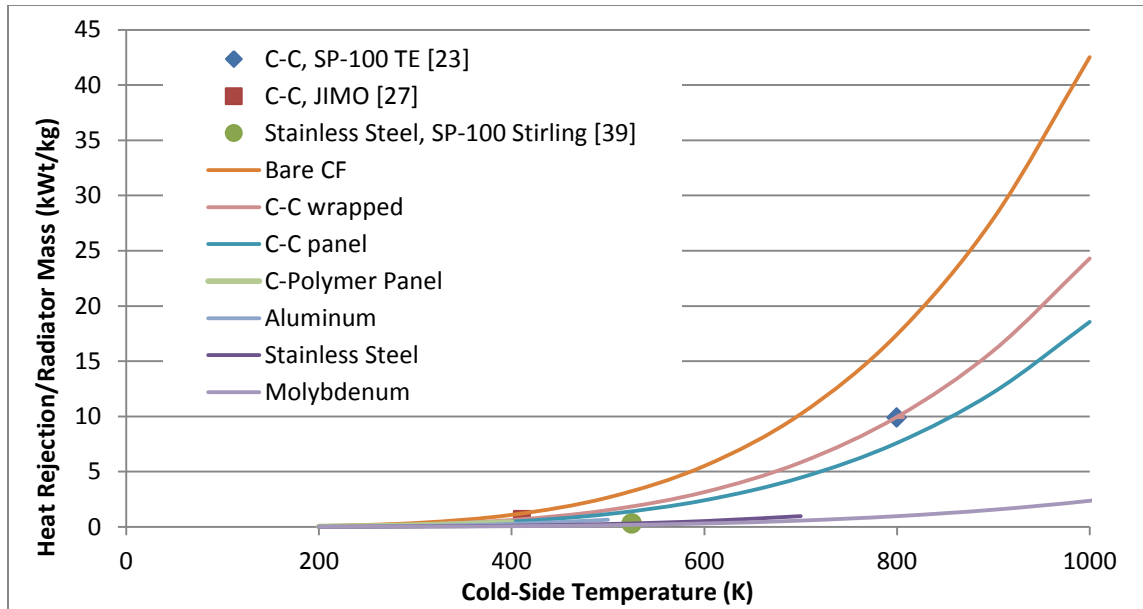
Figure 1.32: Specific radiator heat rejection versus radiator temperature for different fin materials
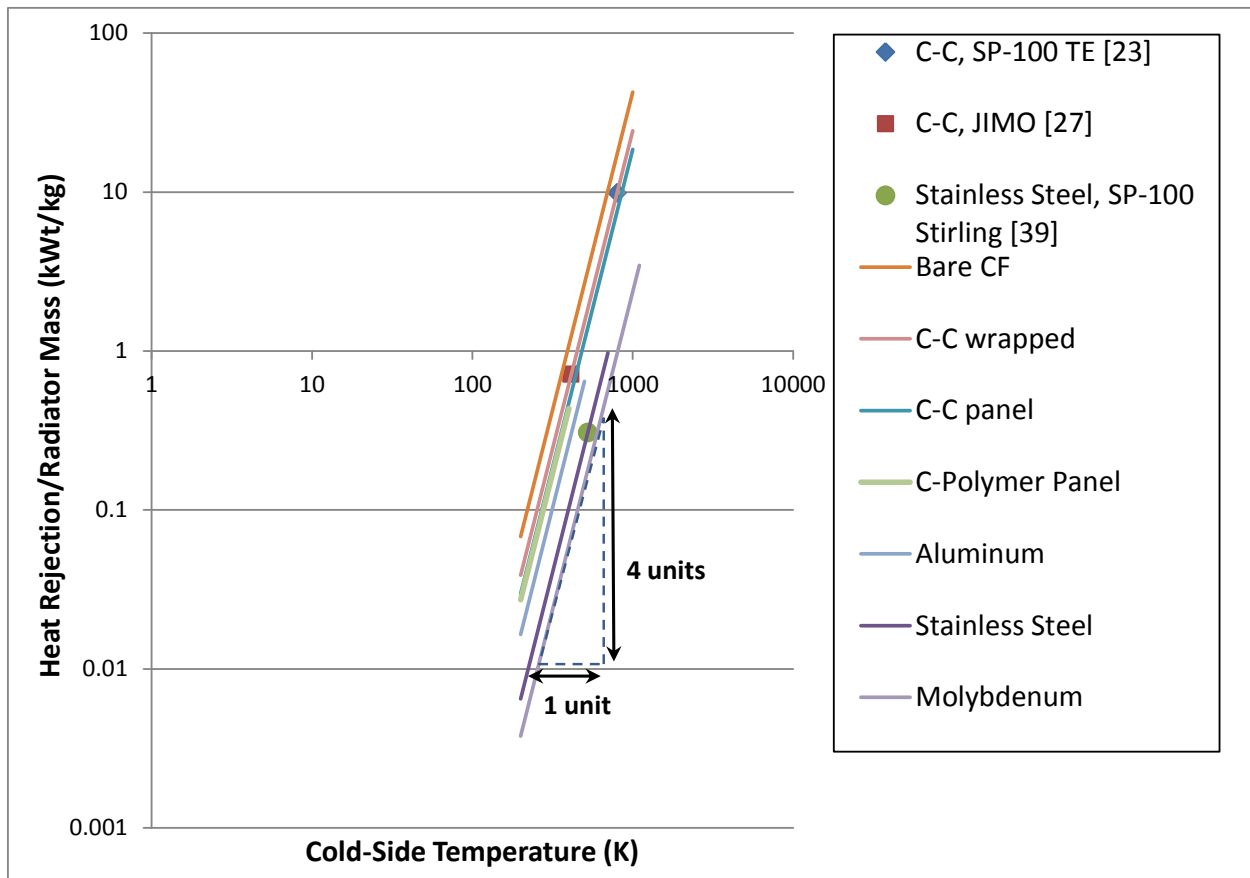
Figure 1.33: Log-log plot of Figure 1.32 showing the fourth power relationship between heat flux and surface temperature

Developing lightweight, high-temperature radiators is one of the major challenges explicitly

stated in NASA's 2010 "Space Power and Energy Storage Roadmap" [7]. A high-temperature,

lightweight radiator could enable and initiate research in other technology areas that would not be

possible otherwise.

1.2.6   Thermal Radiation Overview

Thermal radiation is the heat transfer mechanism by which energy leaves a system in the form

of electromagnetic waves. The heat flux by radiation from a surface is given by Equation 1-2, where q is

the heat flux (J/s/m^2), ε is the total hemispherical emissivity, σ is the Stephan-Boltzmann constant

(5.67x10^{-8} W/m^2/K^4), T is the temperature of the surface (K), and T_{env} is the temperature of the

environment (K). In space T_{env} is approximately 4 K, so that term is often neglected.

$$q = \varepsilon\sigma(T^4 - T_{env}^4) \tag{1-2}$$

Total hemispherical emissivity is a surface property of a material given by the ratio of the total

radiated energy in all wavelengths and all directions by a surface at a given temperature, $e(T)$, to the

same quantity emitted by an ideal black surface at the same temperature, $e_b(T)$. Equation 1-3 gives

this relationship in terms of directional spectral emissivity ($\varepsilon_\lambda(\lambda, \theta, \varphi, T)$). Equation 1-4 gives the total

hemispherical emissivity in terms of hemispherical spectral emissivity ($\varepsilon_\lambda(\lambda, T)$).

$$\varepsilon(T) = \frac{e(T)}{e_b(T)} = \frac{\int_{\varphi=0}^{2\pi}\int_{\theta=0}^{\pi/2}\left[\int_0^\infty \varepsilon_\lambda(\lambda,\theta,\varphi,T)i_{\lambda b}(\lambda,T)d\lambda\right]\cos\theta\sin\theta\, d\theta d\varphi}{\sigma T^4} \tag{1-3}$$

$$\varepsilon(T) = \frac{\pi\int_0^\infty \varepsilon_\lambda(\lambda,T)i_{\lambda b}(\lambda,T)d\lambda}{\sigma T^4} = \frac{\int_0^\infty \varepsilon_\lambda(\lambda,T)e_{\lambda b}(\lambda,T)d\lambda}{\sigma T^4} \tag{1-4}$$

Where $i_{\lambda b}(\lambda, T)$ is the spectral radiative intensity of a blackbody, which is by definition

independent of direction, $e_{\lambda b}(\lambda, T)$ is the blackbody spectral emissive power, θ is the altitude angle, and

φ is the azimuthal angle of the surface element's hemispherical envelope. The cosine in Equation 1-3 is

derived from the directional dependence of a blackbody's emissive power. A blackbody is a diffuse

emitter, which means that the intensity of radiation is uniform in all directions. The emissive power,

however, is not uniform in all directions because the projected area of the emitting surface element

decreases with $\cos\theta$, as given by Lambert's Cosine Law in Equation 1-5 where $e_{\lambda b}(\lambda, \theta, T)$ is the

directional emissive power for a black surface. Figure 1.34 shows emissive power as a function of the

altitude angle, θ. The maximum radiative flux occurs normal to the surface, and zero flux occurs

tangentially since the surface's projected area goes to zero.

$$e_{\lambda b}(\lambda, \theta, \varphi, T) = i_{\lambda b}(\lambda, T) \cos\theta = e_{\lambda b}(\lambda, \theta, T) \qquad \text{(1-5)}$$
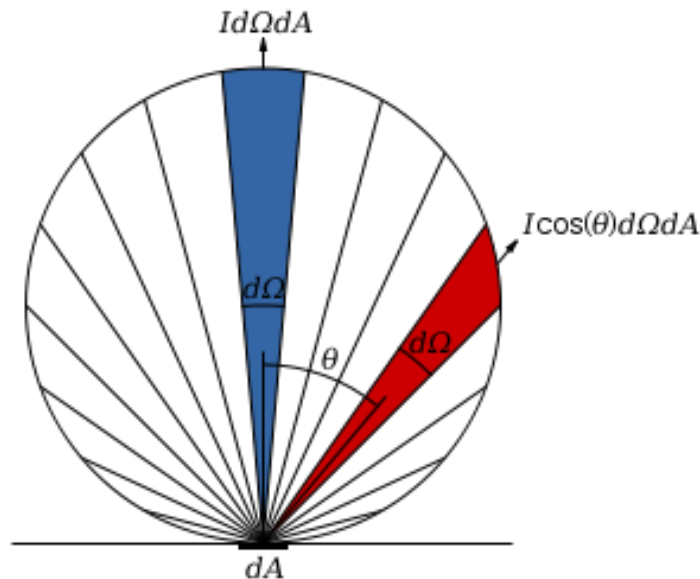
Figure 1.34: The dependence of energy emitted from a diffuse surface on the altitude angle θ, as
described by Lambert's Cosine Law [46]

In Equation 3 the projected area of the emitting surface must be integrated over the entire

hemispherical envelope, which is the solid angle of the hemisphere. A differential solid angle is given

by: $d\omega = \sin\theta \, d\theta d\varphi$. Figure 1.35 is a schematic of the radiative flux from a surface element through a

solid angle $d\omega$. Hence, the blackbody spectral emission from a surface point over the entire

hemispherical envelope is given by Equation 1-6.

$$e_{\lambda b}(\lambda, T)d\lambda = i_{\lambda b}(\lambda, T)d\lambda \int_{\varphi=0}^{2\pi} \int_{\theta=0}^{\pi/2} \cos\theta \sin\theta \; d\theta d\varphi = \pi i_{\lambda b}(\lambda, T)d\lambda \qquad (1\text{-}6)$$
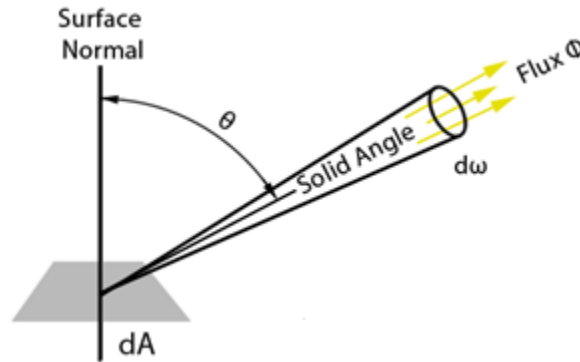
Figure 1.35: Energy flux through a solid angle $d\omega$ [47]

The total emissive power from a given real surface element in the entire hemispherical envelope is given Equation 1-7.

$$e(T) = \int_{\varphi=0}^{2\pi} \int_{\theta=0}^{\frac{\pi}{2}} \left[\int_0^\infty \varepsilon_\lambda(\lambda, \theta, \varphi, T) i_{\lambda b}(\lambda, T) d\lambda \right] \cos\theta \sin\theta \; d\theta d\varphi \qquad (1\text{-}7)$$

In 1900, Max Planck proposed a law that describes the spectral distribution of hemispherical emissive power in a vacuum for a blackbody at a given absolute temperature. Planck's Law, or "Planck's Spectral Distribution of Emissive Power", is given in Equation 1-8. This was based on quantum theory and verified experimentally [68].

$$e_{\lambda b}(\lambda, T) = \pi i_{\lambda b}(\lambda, T) = \frac{2\pi h c_0^2}{\lambda^5 (e^{hc_0/\lambda kT} - 1)} \qquad (1\text{-}8)$$

Where h is Planck's constant ($h = 6.62606876 \times 10^{-34}$ J $\cdot$ s), k is the Boltzmann constant ($k = 1.3806503 \times 10^{-23}$ J/K), and c_0 is the speed of light in a vacuum ($c_0 = 0.299792458 \times 10^{14}\ \mu m$/s). The wavelength at which the peak emissive power occurs, λ_{max}, is given by "Wein's Displacement Law" in Equation 1-9. Figure 1.36 shows emissive power versus wavelength curves for different temperatures. As temperature increases, the peak of the curve moves toward shorter wavelengths.

$$\lambda_{max}T = \frac{hc_0}{5k\left(1-\exp\left(-\frac{hc_0}{\lambda_{max}T}\right)\right)} = 2897.7686 \, \mu m \cdot K \qquad (1\text{-}9)$$
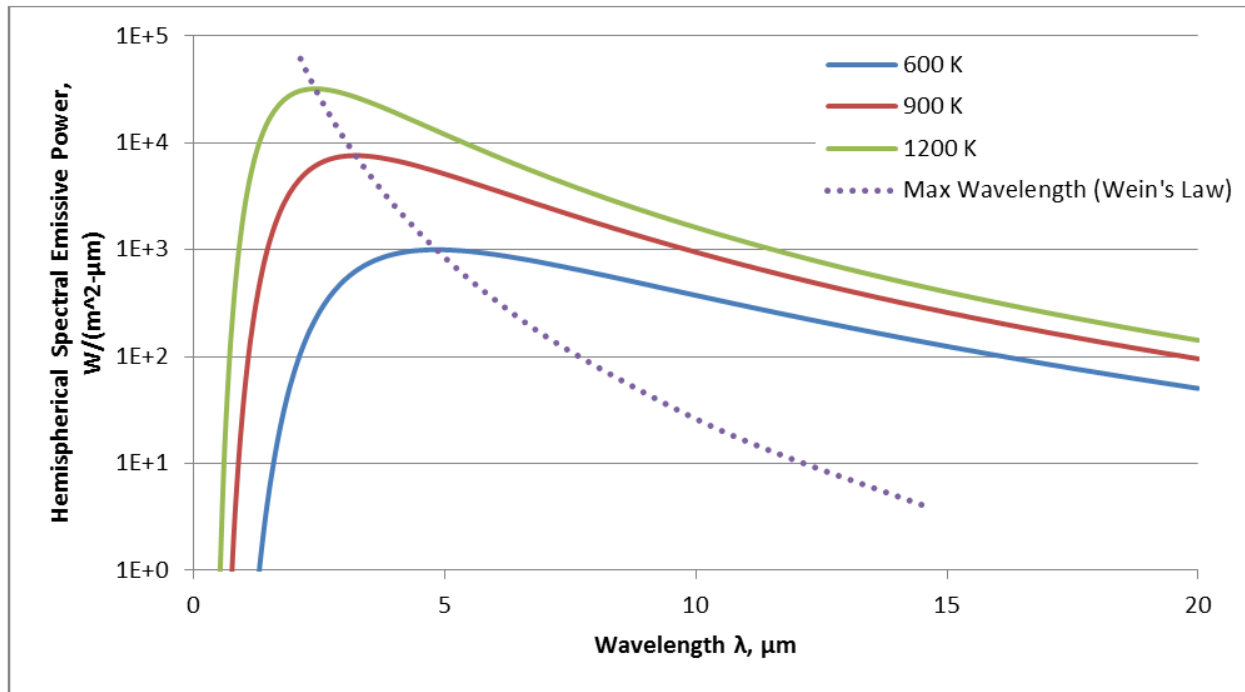
Figure 1.36: Hemispherical spectral emissive power of a blackbody at several temperatures, given by Planck's Law

Many engineering materials are idealized to have gray surfaces to simplify radiation calculations. Gray surfaces emit spectral radiation at a fixed fraction of the emitted blackbody spectral radiation for a given temperature. Figure 1.37 shows the hemispherical spectral emissive power for a blackbody and a gray body with an emissivity of 0.6 at 900 K.
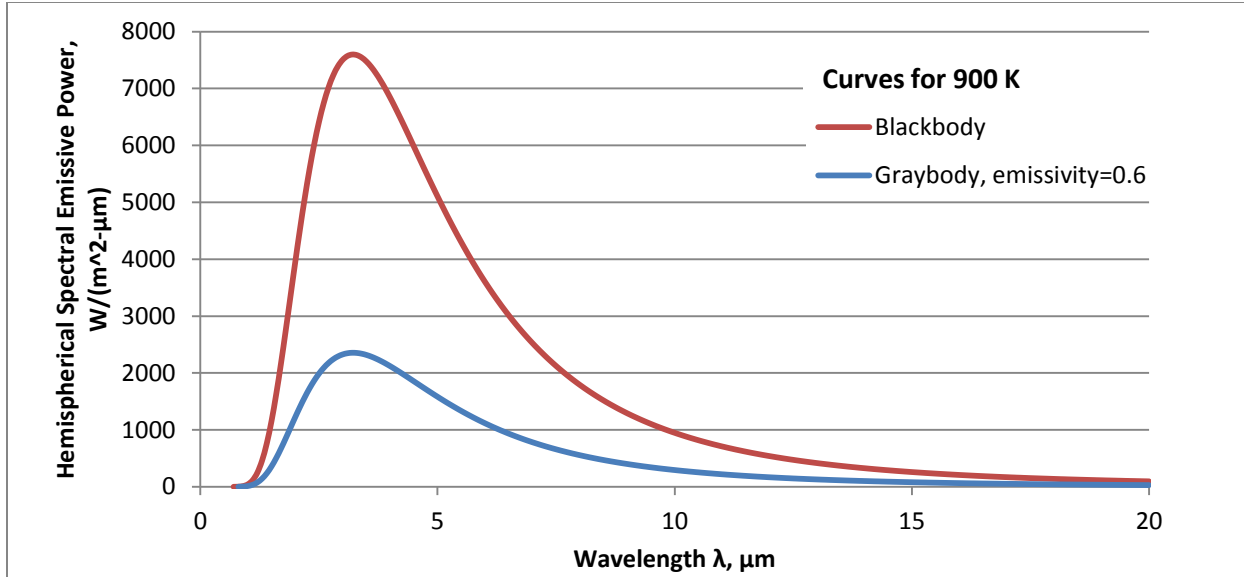
Figure 1.37: Hemispherical spectral emissive power versus wavelength for a blackbody and gray body at 900 K

In a multi-surface system, radiation exchange between elements will occur if they have a non-zero projection onto one another. In a multi-surface system, a full radiosity problem must be solved to calculate the net energy flux leaving a surface by emission or reflection. Radiosity, *J*, is the rate at which radiant energy leaves a surface per unit area. The radiosity from a diffuse-gray surface, *i*, surrounded by *N* surfaces is given by Equation 1-10, where H is the incident radiant flux. The incident radiant flux is given by Equation 1-11, where B_j is the radiosity from another surface and $F_{A_i-A_j}$ is the viewfactor from surface *i* to surface *j*. To solve the full radiosity problem, Equation 1-11 must be written for all *N* surface elements in the enclosure and solved simultaneously for the *N* unknown J_i's.

$$J_i = \varepsilon_i \sigma T_i^4 - (1 - \varepsilon_i)H_i, \ \ 1 \le i \le N \tag{1-10}$$

$$H_i = \sum_{j-1}^{N} J_j F_{A_i-A_j} \tag{1-11}$$

1.2.7   Thermal Properties

At steady state, the two most important thermal properties of a radiator fin are the longitudinal thermal conductivity and total hemispherical emissivity.

1.2.7.1 Thermal Conductivity

The fin axial thermal conductivity controls how quickly heat can be transferred in the direction normal to the heat pipe. Energy can be transferred through a solid by either phonons or free electrons. In metals, free electrons transport heat as they move about the lattice colliding with nuclei, transferring thermal energy with each collision. This is a fast solid-state heat transfer mechanism because electrons travel at high velocities. Materials with high densities of free electrons have correlated thermal and electrical conductivities since free electrons act as thermal energy and charge carriers. This behavior is described by the Wiedemann-Franz law that states that for a metal the ratio of thermal to electrical conductivity is proportional to the temperature as given in Equation 1-12.

$$LT = \frac{\kappa}{\sigma} \qquad\qquad (1\text{-}12)$$

Where L is the Lorenz Number ($2.45 \times 10^{-8} W\Omega K^{-2}$), κ is the thermal conductivity ($W(mK)^{-1}$), σ is the electrical conductivity ($\Omega^{-1}m^{-1}$)), and T is the material's temperature (K).

Phonons are high frequency, low amplitude acoustic waves produced by vibrating atoms that travel through the solid lattice structure carrying vibrational thermal energy. Heat conduction in most non-metals is dominated by this method of energy transfer due to the low density of free electrons. Typically, heat transfer by free electrons is much faster than phonon transfer because high velocity electrons carry energy as they move freely in the lattice, whereas phonons propagate by moving the whole lattice structure around the vibrating high energy atoms. Both phonons and free electrons experience scattering due to interactions with lattice imperfections. Phonons are much more sensitive to scattering, which is another reason why phonon heat transport is less effective than the free electron mechanism.

Graphite and graphene are considered semimetals or zero-band-gap semiconductors because unlike semiconductors, they always have charge carriers (i.e., free electrons and holes) that can conduct, but unlike metals they do not have a large amount free electrons. In most non-metals, heat transfer is

dominated by phonon transport, which is typically the slower transport mechanism. In graphene layers, however, phonon transport is extremely fast due to the strong covalent bonds between the planar carbon atoms [49]. The stronger the chemical bonding, the faster phonons may travel. In addition to strong bonds, phonon transport is enhanced with fewer defects and grain boundaries that scatter the energy. Diamond is another good example of this phenomenon, with pure diamond exhibiting one of the highest known thermal conductivities at room temperature (2200 W/(m-K)) and is an electrical insulator. Again, this is due to the extremely strong covalent bonding in the diamond crystal lattice, not due to free electron transport.

A comparison of the thermal and electrical conductivities of several metals and Mitsubishi carbon fibers is shown in Figure 1.38. This shows that the pitch-based carbon fibers (labeled "Dialead" in the Figure), have far superior thermal conductivity over the metals and the PAN-based carbon fibers, while having relatively high electrical resistance.
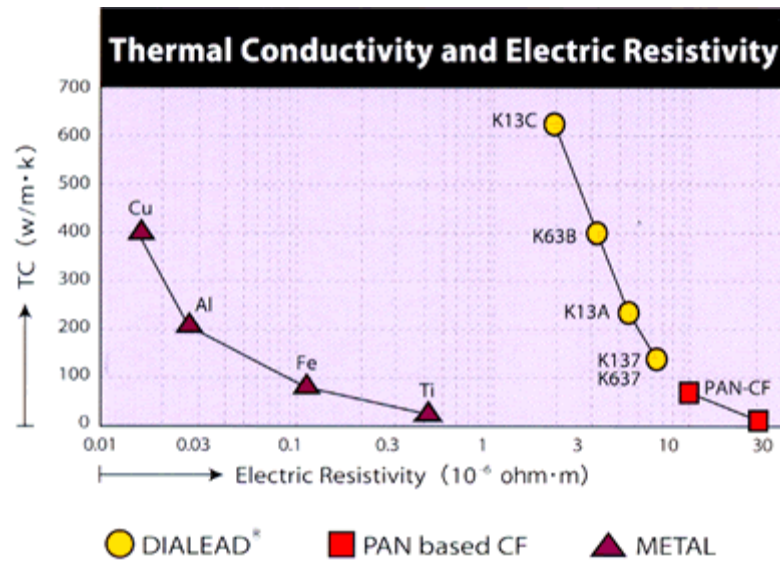
Figure 1.38: Thermal Conductivity and Electrical Resistivity of Select Metals and Carbon Fiber Materials [50]

Conventional methods for measuring thermal conductivity, like the guarded hot plate method (ASTM C177 Test Method), are often used for isotropic solids that can be easily sectioned into uniform

samples. This would not be feasible for fibrous materials, as the uncertainty associated with the

disordered fiber sample would be larger than the precision of test. Therefore, another method

specifically designed for fibers is used, the hot-wire method (ASTM C1113 Test Method), which

measures the thermal conductivity of a single fiber [51]. This method was likely used to generate the

fiber data in Figure 1.38. None of the standard methods is easily adaptable to measuring the thermal

conductivity of loose, bulk fiber material. The development of a method to address this need is given in

Chapter 4.

It should be noted that the stiffness of the carbon fibers is positively correlated with thermal

conductivity because they are both affected by the fiber microstructure, or degree of graphitization. As

the graphene sheets become more aligned along the fiber axis, the fiber becomes stiffer. This results in

increased critical bend radius for high thermal conductivity pitch-derived carbon fibers, as compared low

thermal conductivity PAN-derived fibers.

1.2.7.2 Emissivity

All matter at temperatures above absolute zero emits radiation. Thermal energy causes atoms

and molecules to move in particular patterns depending on the composition and microstructure of the

material and amount of energy. Interacting electrons and protons cause charge-acceleration and

dipole-oscillations, which generate electromagnetic waves. Further specifics on the mechanisms of

producing electromagnetic radiation will not be discussed here. Besides the electromagnetic wave

generating mechanisms, the geometry of the surface on a micro-scale also affects the effective surface

emissivity. Rougher surfaces provide more surface area on a micro-scale from which to radiate, and

thus tend to have higher emissivities than polished surfaces.

Emissivity measurements of graphite range from about 0.6 to 0.95 depending on the surface preparation, so it is expected that the emissivity of carbon fiber is also in that range [48][52][53]. Chapter 4 describes the emissivity measurement technique used in this work.

1.3   Organization of this Text

The following chapters discuss the research conducted on the design, fabrication and testing of carbon fiber radiator fins for advanced space power systems. Chapter 2 presents a micro-scale study of geometric effects on the effective emissivity of an array of carbon fibers. Chapters 3 and 4 present results from bench-scale experimental studies of the radiator concept. Chapter 5 discusses full-scale heat rejection system considerations. Finally, conclusions and future work are presented in Chapters 6 and 7.

CHAPTER 2

PREDICTING THE EFFECTIVE EMISSIVITY OF A CARBON FIBER ARRAY USING A MONTE CARLO RAY TRACING MODEL

2.1   Introduction

As discussed in Chapter 1, designing innovative radiators is critical to advancing NEP technology and future deep space travel. The purpose of radiating fins is to quickly conduct the power conversion engine's waste heat over a large radiating area with a maximum view factor to space. Common fin materials such as aluminum and carbon fiber composites typically do not meet NASA's areal density goals for deep-space vehicles [10]. Thus, a bare, pitch-based, carbon fiber weave radiator fin is proposed because of the fiber's high thermal conductivity, 800 W/m-K (Mitsubishi product number K13D2U), low density, and inherently high emissivity. Unlike composites, the bare carbon fiber fin concept has no matrix. The matrix material adds a significant mass penalty and thermal resistance along the heat transport path to space. Without the matrix, the free fiber weave radiates directly to space, which is a novel heat transfer problem.

Zhu (2009) has shown experimentally that optically thick yet porous carbon fiber felt is more emissive than a smoother deposited carbon surface [52]. This result supports the hypothesis that a lower volume fraction medium that is optically thick can provide a higher effective emissivity over flat fins due to the added surface area free to radiate to space. The geometry of the fiber weave (i.e., fiber packing density and weave thickness) will influence the effective emissivity of the weave. Within the manufacturing limits, the weave design should maximize the effective emissivity. Thus, predicting the dependencies of the weave design parameters on the effective emissivity is of great value.

In many radiative heat transfer problems, the objective is to determine the radiative heat flux through a certain plane, which requires defining or solving for the emitting surface temperature(s). In this study, radiative properties (e.g., effective emissivity) instead of heat flux are estimated. By

predicting the radiative behavior of an array of carbon fibers, the properties can be used in radiator-fin-level finite element models where the fins are idealized as flat surfaces. The effective emissivity of the fiber weave accounts for the added fiber surface area exposed to space directly or indirectly through scattering so that the extra emissive capacity of the fins is not lost when modeling them as flat surfaces.

Fibrous media is often characterized as pseudo-continuum, with highly complex integro-differential radiative heat transfer equations that have only numerical solutions [56][57]. As radiation travels through a fibrous medium, scattering occurs as it reflects from fiber surfaces. Due to scattering effects, the radiation intensity at a given point cannot be determined by local properties and their derivatives, as with most other transport relations (e.g., Fourier's law). Instead, the intensity of all surfaces in the domain depend on the intensity at every other surface, which makes problems of radiative heat transfer through participating media difficult to solve using standard numerical integration methods.

Solution approximations of radiative heat transfer problems through fibrous media that emit, absorb, and scatter radiation have been obtained using Monte Carlo Ray Tracing (MCRT), analytical models developed for participating media, or through curve-fitting using empirical data [57]. Analytical approaches use electromagnetic theory to describe radiation scattering behavior within specific types of participating media including Rayleigh and Mie Scattering theories, which assume spherical particles that are generally small compared with the wavelength of the incident radiation. Since these assumptions are not appropriate for the anisotropic, larger-diameter fibers in the current work, and since empirical data is unavailable for this material, a MCRT method was selected.

Monte Carlo Ray Tracing is a numerical method that combines ray optics with stochastic methods for generating ray emission locations and directions. In general, ray tracing methods generate "rays" (e.g., single or bundles of photons) from all emitting surfaces or volumes in the model domain and follow the rays as they travel through the domain. A ray may get absorbed by media, reflected out,

or transmitted through the domain. Monte Carlo (MC) numerical methods use stochastic techniques for solving problems that are generally too complicated or expensive to solve analytically or by direct numerical integration [48]. As with any well-posed stochastic method, the results converge to the solution with increasing trials, or rays in this case. In MCRT simulations, ray emission surface locations and select model parameters are chosen randomly with the appropriate probability density functions. Monte Carlo techniques are used in this model to generate the random location and direction of emitted rays along the source boundary, and random ray reflection directions when rays reflect off fiber surfaces. More specifics are provided later in this Chapter.

Studies in the literature have used MCRT techniques successfully to predict the effective emissivity of cavities and other self-viewing bodies [59] – [66]. Other studies on radiative heat transfer through fiber insulation have employed MCRT methods to determine the surface-to-surface view factors between the heat source, heat sink and fibers [62][67]. Surface-to-surface view factors are useful for solving the full radiosity problem, but since the goal of this work is to predict the effective emissivity of the surface plane of the fin from the entire collection of fibers beneath, a slightly different method called reverse MCRT is used. Utilizing the principle of reciprocity in radiative heat transfer, reverse MCRT methods can be used to simplify the problem [56][68][69]. The basic principle of reciprocity uses the assumption that the effective total absorptivity of an isothermal cavity will be equal to the effective total emissivity due to Kirchhoff's Law. In the reverse method, rays are emitted from the target surface and traced into the domain. This is especially useful when the emitting surfaces have complex geometries, are part of a porous medium, or make up the boundaries of a cavity. Since the high-conductivity fibers are heated primarily by axial conduction, it is reasonable to assume they are nearly isothermal at a given fin cross-section. According to Howell (1998), reverse MCRT techniques are employed to reduce variance in slow-converging problems [68]. Several applications of this method appear in the literature, where the target surface is much smaller or simpler than the emitting

surface(s), including effective emissivity predictions of blackbody cavities and scattering packed-beds [61][65][66].

Unique to this work, the effective absorption, reflection, and transmission rates of the fiber media are distinguished. Separating these effects provides insights into how the effective radiative properties vary with fiber volume fraction and fiber surface emissivity. These generalized radiative results are independent of temperature and thus can be used to inform the design of fiber media for various thermal applications.

2.2   Reverse Monte Carlo Ray Tracing Model

The effective emissivity of an array of carbon fibers was estimated using reverse MCRT methods. Instead of emitting rays from each fiber, rays were incident upon the fiber array and traced into the model domain. The effective absorptivity, which was taken as equal to the effective emissivity, was calculated by taking the ratio of the number of rays absorbed by the array to the total number of incident rays. The model was built and executed in Matlab.

2.3   Assumptions and Model Development

The model development and assumptions pertaining to the fiber configuration in the model domain, fiber properties, and radiation physics (i.e., scattering behavior) are presented below.

2.3.1   Model Domain

The fibers were assumed to be long cylinders with uniform diameters, aligned parallel to one another, and dispersed uniformly in a hexagonal array. Figure 2.1 is a schematic of the model domain, which was defined such that the periodic hexagonal array was fully represented. Symmetry side boundaries were set by intersecting two adjacent columns of fibers. Using symmetry conditions to minimize the domain width reduces computational cost. Reducing the array to a 2-D domain is valid for

predicting the effective emissivity because the z-direction component does not affect the penetration depth. The counting planes shown in Figure 2.1 are used track the fraction of active rays versus depth.
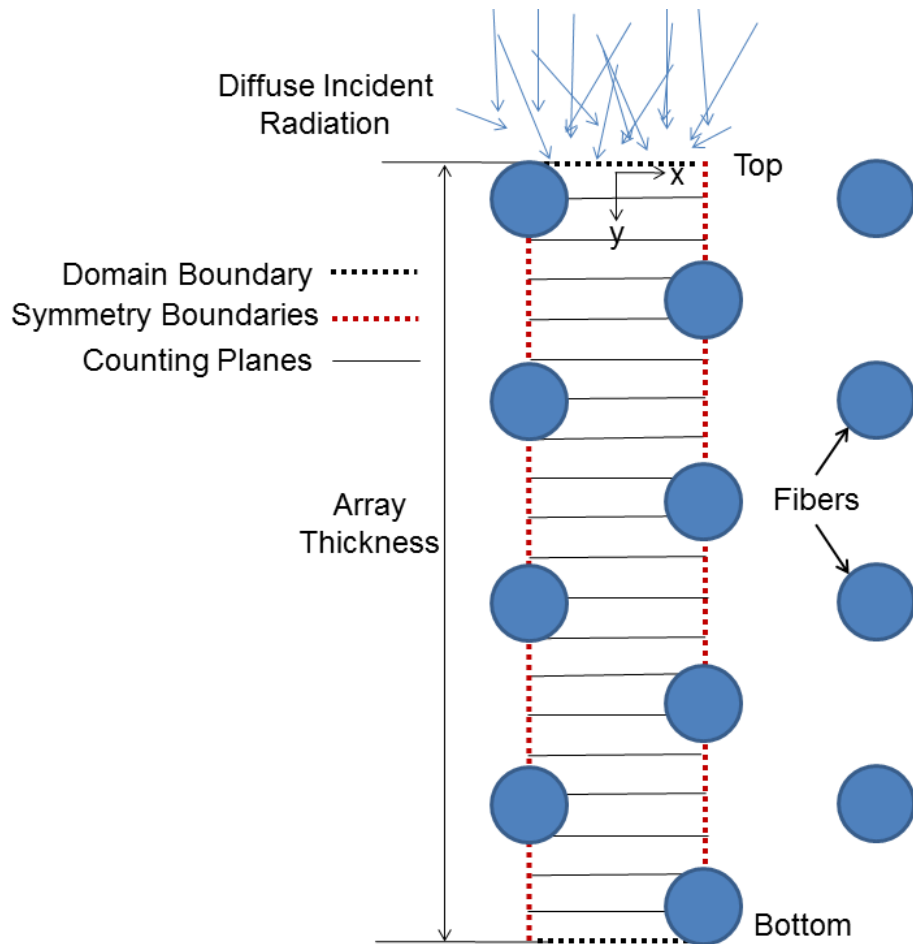
Figure 2.1: Model domain for a four-fiber thick array

Boundary conditions were imposed on the top boundary, bottom boundary, fiber surfaces, and symmetry side walls. The top surface was the boundary from which the diffuse incident radiation was introduced to the domain. Rays that intersected the top boundary after a reflection escaped out of the fiber array and were not followed further. Likewise, rays that intersected the bottom boundary were transmitted and not followed further. When a ray collided with a fiber, the energy was absorbed or reflected. As demonstrated in Figure 2.2, symmetry conditions were valid because a ray ultimately collides with a fiber at the same depth within the domain as it would have if it had continued its trajectory through the array.
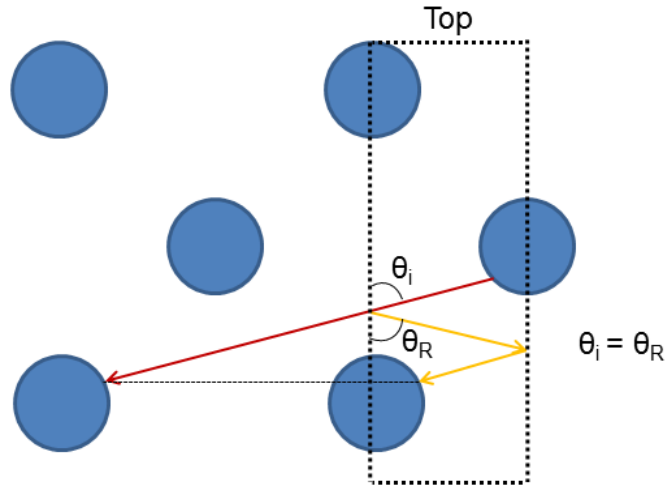
Figure 2.2: Schematic of the fiber array showing how rays reflected from symmetry side walls reach a fiber at the same depth (yellow ray) within the domain as they would have if the domain contained a larger array (red ray)

The volume fraction of fibers in three-dimensional space is the same as the area fraction in two dimensions because the array cross section was assumed to be constant along the axis of the fibers. The maximum fiber packing density is achieved when there is no space between adjacent fibers. The maximum fiber packing density, or volume fraction, is $\rho = \frac{1}{6}\pi\sqrt{3} \cong 0.9069$.

2.3.2   Fiber Emissivity and Scattering Behavior

The fibers were assumed to be opaque, with gray-diffuse surfaces. Depending on surface preparation and purity, the emissivity of graphitic materials is typically in the range of 0.7-0.9. It has been shown experimentally that similar materials (i.e., graphite and carbon-carbon composites), have relatively flat spectral responses for a broad range of temperatures [52][70]. The spectral emissivity of a sample of the carbon fiber used for this work was measured in Chapter 4. The emissivity was nearly uniform over a wide range of wavelengths. Thus, the spectral emissivity was assumed to be independent of wavelength and temperature, and equal to the total hemispherical emissivity.

A dispersed fiber array can be described as porous, participating, or scattering media. Participating media may scatter, absorb, and emit radiation; common examples include clouds, smoke and, fog. Optically-thin, dispersed fiber arrays could be categorized as participating media, however, the individual fibers are typically larger than the scattering particles in clouds or smoke. This makes a fiber array act less like a continuous medium than common participating media, so some of the characteristic behaviors may be described by slightly different models (i.e., Beer's Law for predicting the absorption coefficient). Densely-packed, optically-thick, fiber arrays are more aptly described as porous media, such as a packed bed or solid foam. When incident radiation penetrates the exterior envelope of a porous medium and strikes an interior surface, it may undergo multiple scattering events before getting fully absorbed or reflected out of the envelope. This characteristic, as shown in Section 2.4, increases the effective absorptivity, and thus emissivity, of a given fin surface envelope.

Scattering is the deflection of a photon from its original path by dispersed media by means of reflection, refraction, or diffraction. Scattering is divided into the subcategories independent and dependent scattering. Independent scattering, which assumes no near-field effects, is assumed for this study. Ray tracing uses the laws of geometrical optics, which neglect diffraction and near-field effects. It is common practice to assume independent scattering when $c/\lambda > 0.3$ or 0.5, where c is the average pore size [72][73][74][75]. However, low porosity media with a small particle size parameter $(x = \frac{\pi d}{\lambda} < 1$, where x is particle size parameter and d is the fiber diameter) has been shown to scatter dependently [76]. For carbon fibers with diameters in the range of 10-20 µm, dependent scattering of large wavelength radiation ($\lambda > 10$ µm) may occur at high fiber volume fractions, yet in the absence of data specific to this condition and the limited ability to address this phenomenon with ray tracing, it is neglected here. Even when packed densely, the fibers are large enough that most of the diffracted photons will remain nearly parallel to the original direction [6], thus diffraction is also neglected.

Independent scattering without diffraction is increasingly applicable with increasing fiber diameter and decreasing average wavelength.

Since carbon fibers are not polished and have a dull luster, it was assumed that reflections from fiber surfaces are diffuse. There are two common ways to simulate ray reflections and ray attenuation in ray tracing models. Rays consist of either a single photon or a bundle of photons. In the single-photon case, when a ray strikes a participating surface the entire energy of the ray is either absorbed or reflected. The probability of a ray absorbing when it strikes a surface is given by the surface total absorptivity, $P_{abs} = \alpha$, thus the probability of a reflection is $P_{ref} = 1 - P_{abs} = 1 - \alpha$. For multi-photon rays, at each fiber interaction the ray intensity is reduced by a fraction, given by the fiber total absorptivity, and the remaining energy is reflected. In general, simulations using multi-photon rays should converge faster than single-photon rays. This study investigates both ray structures.

The reflection angles are selected randomly with the probability density function characteristic of a Lambertian surface. The probability density function for the zenith angle, θ, is derived from Lambert's Cosine Law, and the azimuthal angle, φ, is uniform over 2π. Yang *et. al.* shows the derivation of the zenith and azimuthal angles as functions of uniform random numbers, R_1 and R_2, with values between 0 and 1, given in Equations 2-1 and 2-2 [77].

$$\theta(R_1) = \cos^{-1}(\sqrt{1 - R_1}) \tag{2-1}$$

$$\varphi(R_2) = 2\pi R_2 \tag{2-2}$$

To transform this into a 2-D probability density function, the ray direction given in spherical coordinates (θ, φ) is converted to polar coordinates (θ_2) by projecting it onto the x-y plane. The two angles in the spherical domain collapse to one angle in the 2-D domain, as shown in Figure 2.3. As mentioned previously, the z-component of the ray does not affect the ray penetration depth as defined here. Equation 2-3 gives the 2-D probability density function.

$$\theta_2(R_2, R_3) = \begin{bmatrix} tan^{-1}\left(\frac{\sqrt{1-R_2}}{\sqrt{R_2}\,sin(2\pi R_3)}\right) & for\ sin\theta sin\varphi > 0 \\ \pi + tan^{-1}\left(\frac{\sqrt{1-R_2}}{\sqrt{R_2}\,sin(2\pi R_3)}\right) & for\ sin\theta sin\varphi \le 0 \end{bmatrix} \tag{2-3}$$

This ray probability density function (PDF) is used to generate the angles of the diffuse incident radiation and reflections. Figure 2.4 demonstrates that the resulting polar angle, θ_2, PDF for the incident radiation follows Lambert's Cosine Law which predicts the maximum emission in the direction normal to the surface and zero emission tangent to the surface.
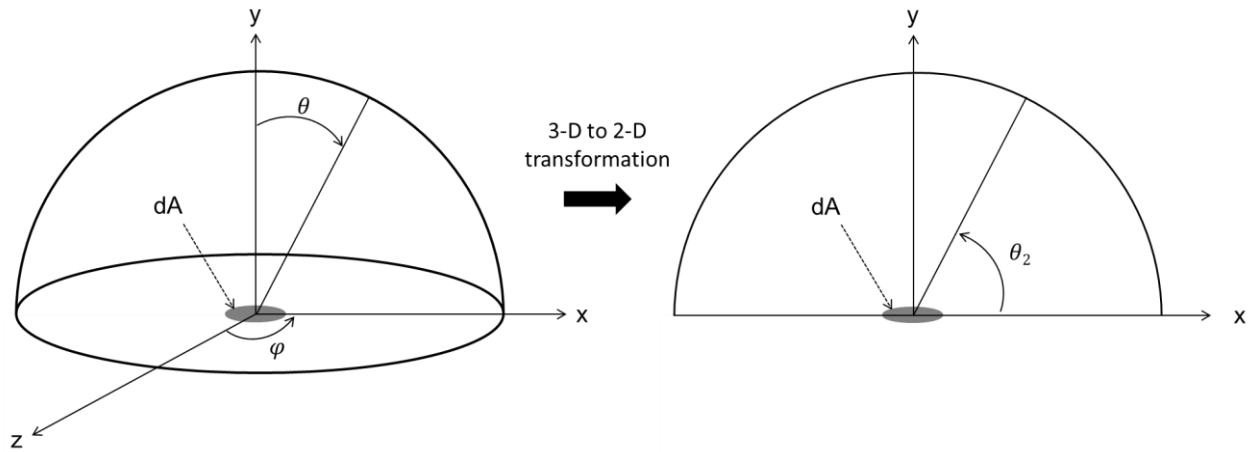
Figure 2.3: Angles of hemispherical radiative emission from a boundary element, dA, in 3-D (left), and the transformation into 2-D (right)
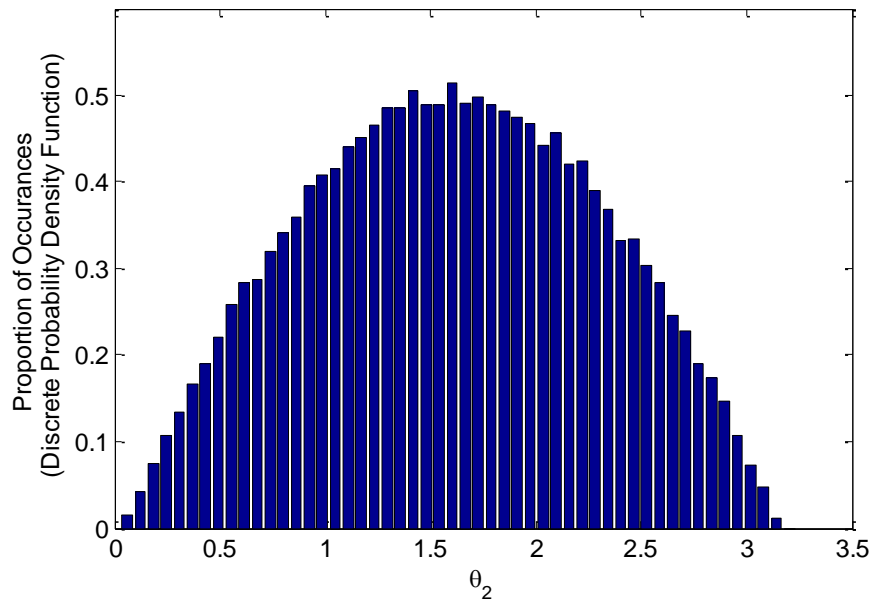
Figure 2.4: Probability density function for θ_2, demonstrated using 100,000 rays

2.3.3   Methods Verification and Validation

Characteristic of Monte Carlo simulations, the results should converge to the solution with increasing number of trials. To validate the diffuse radiation PDF, used for ray emission and reflection, as well as the 2-D simplification, the MCRT algorithm was used to solve for the known view factor between two infinitely long cylinders with the same diameter, as shown in Figure 2.5. Equation 2-4 is

the known view factor relation for this arrangement. Figure 2.6 shows that the simulation converges to within 2% of the analytical solution in about 50,000 rays. This confirms that the 2-D simplifications to the MCRT model preserve the PDF of directions of rays as given in 3-D.

$$F_{1-2} = F_{2-1} = \frac{1}{\pi\left(\sqrt{X^2-1}+\sin^{-1}\left(\frac{1}{X}\right)-X\right)} \qquad \text{where: } X = 1 + \frac{s}{2r} \qquad (2\text{-}4)$$
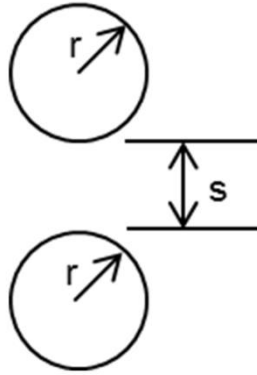
Figure 2.5: Configuration of two infinitely long cylinders with uniform radii, used for the view factor validation
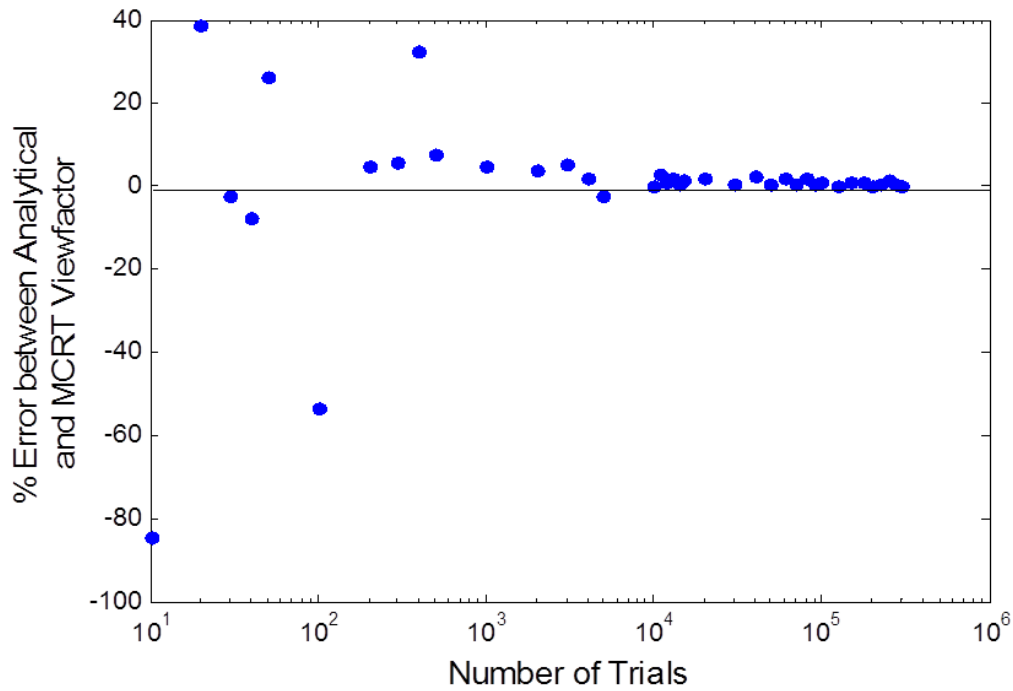
Figure 2.6: Percent error between the analytical and MCRT view factors versus number of trials (rays) in the simulation

To verify the number of rays required for solution convergence, convergence at multiple design points was tested. Figure 2.7 is a convergence plot for the effective emissivity for a 0.5 mm thick fiber array with a volume fraction of 0.2267 and individual fiber emissivity of 0.8 for multi- and single-photon

rays. After 50,000 multi-photon rays, the effective emissivity converged to approximately 0.883. The

single-photon rays converge to 0.883 after approximately 100,000 rays.
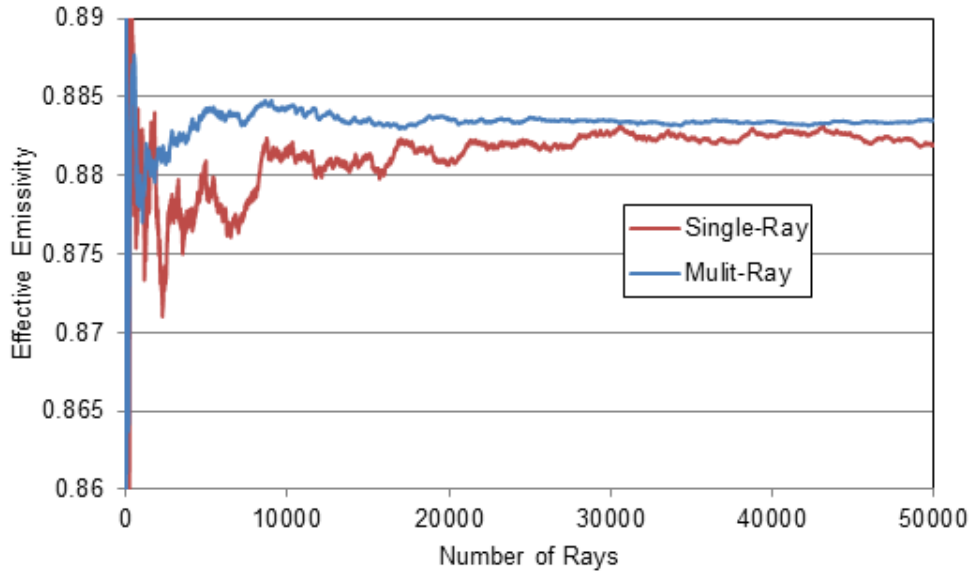
Figure 2.7: Convergence of effective emissivity with increasing number of multi-and single-photon rays for an array thickness of 0.5 mm, fiber emissivity of 0.8, and 50,000 rays

To validate the effective emissivity results, these results were compared with other published

results and tested limiting cases. Two limiting cases that were evaluated include the maximum volume

fraction condition and a very sparsely packed fiber array. As the fiber volume fraction approaches 1, the

scattering effects diminish and the effective emissivity should tend toward the fiber surface emissivity.

Conversely, when fibers are spaced very far apart, the array becomes transparent and the effective

emissivity tends toward zero as very few fiber-ray interactions occur. Figure 2.8 shows agreement with

both limits.
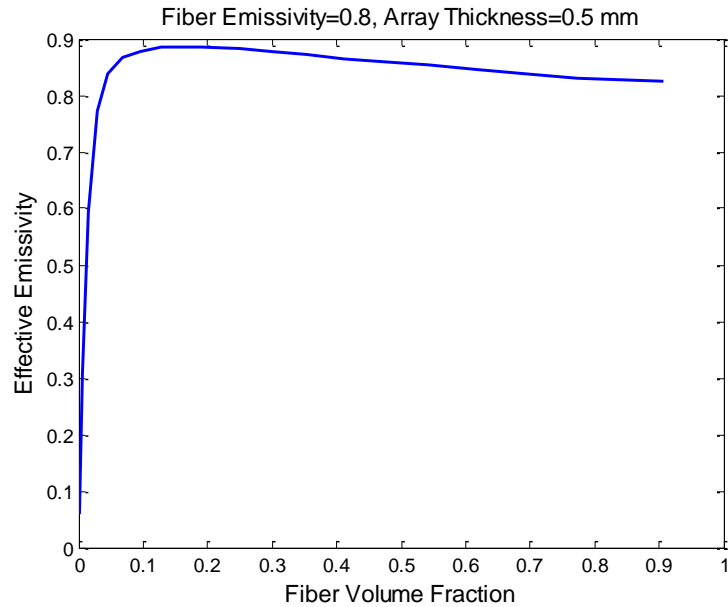
Figure 2.8: Effective emissivity versus fiber volume fraction for a 0.5 mm thick fiber array with fiber surface emissivity of 0.8, using multi-photon-rays

Further validation was achieved by demonstrating agreement with Arambakam's (2011) results on transmittance versus fiber volume fraction for opaque, uniformly-spaced scattering fibers [67]. Arambakam evaluated the effects of microstructural parameters (i.e., fiber diameter, emissivity and volume fraction) on the transmittance of incident radiation through a fiber array using a similar MCRT method for the purpose of predicting the temperature gradient across a slice of fibrous insulation. There were a few differences in the model construction and material properties, including that the fibers were arranged in a rectangular configuration, not close-packed, and the fibers reflected radiation specularly instead of diffusely. Figure 2.9 shows graphical results from Arambakam for the transmittance versus depth for various volume fractions and fiber emissivities. Figure 2.9 shows results from this model at two fiber absorptivities. These show good agreement for high fiber absorptivities. For high absorptivities, the differences in reflection behavior are less pronounced because fewer fiber interactions are required for total ray absorption. For low fiber absorptivities around 0.1 the results differed by a factor of approximately 2, which demonstrates how the significance of reflection angles increases with the average number of fiber interactions.
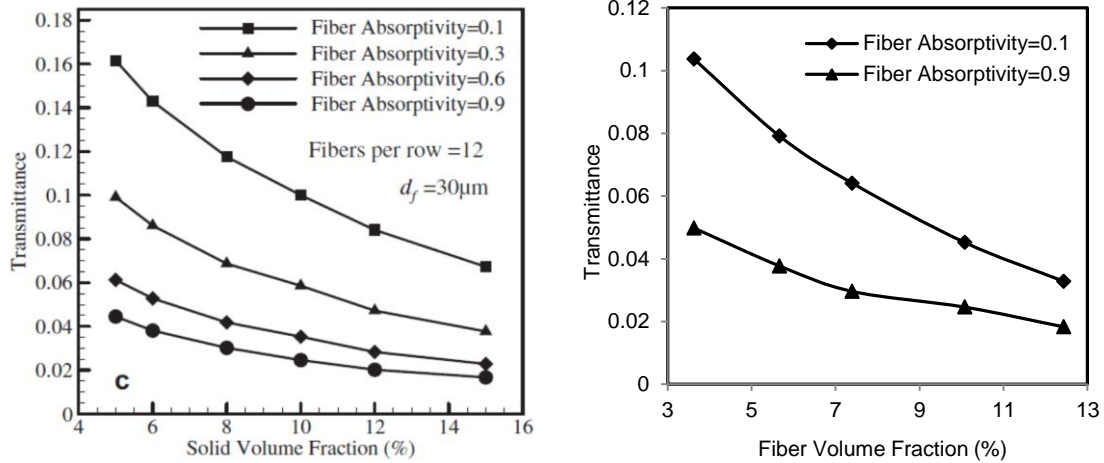
Figure 2.9: Influence of fiber absorptivity and volume fraction on energy transmittance from Arambakam [67] (left) and this work (right) for a 12-fiber-thick array

After the work of Arambakam [67], open questions remained about the effects of fiber volume fraction, fiber emissivity, array thickness, and ray type on the array's effective emissivity. These points are addressed in the new work presented below.

2.4   Results and Discussion

There are several ways to present the model results including visualized ray paths, the effective emissivity dependence on fiber volume fraction and fiber emissivity, and the intensity attenuation dependence on depth. Ray path plots provide a quick verification that the model is functioning properly. This demonstrates how each ray has a unique path due to the random path parameters. Figure 2.10 shows the ray path results for 5 single-photon rays in a model with a fiber volume fraction of 0.2. Various rays demonstrate the diffuse reflection off of fibers, specular reflection off of symmetry boundaries, and ray absorption at fiber surfaces.
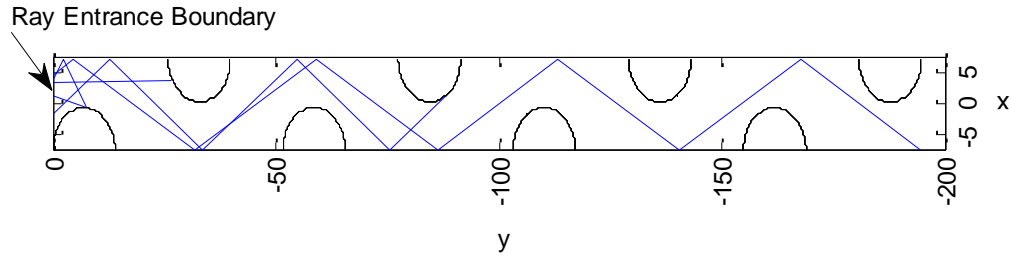
Figure 2.10: Five single-photon ray paths in a simulation with a fiber volume fraction of 0.2 and an array thickness of 0.195 mm

To determine the dependence of the array's effective emissivity on the fiber volume fraction

and fiber surface emissivity, a 0.5 mm thick array was used with different fiber densities and a sufficient

number of rays were used to achieve solution convergence. The array fiber volume fraction ranges from

0.0011 to 0.9069, which contain 2 and 38 fibers respectively in the domain. The 0.9069 volume fraction

was obtained when the fibers touch, thus was the maximum achievable volume fraction. Figure 2.11

gives the results of the total fraction of incident energy absorbed (i.e., effective emissivity), transmitted,

and reflected versus fiber volume fraction for a fiber surface emissivity of 0.8, an array thickness of 0.5

mm, and 50,000 multi-photon rays per simulation.
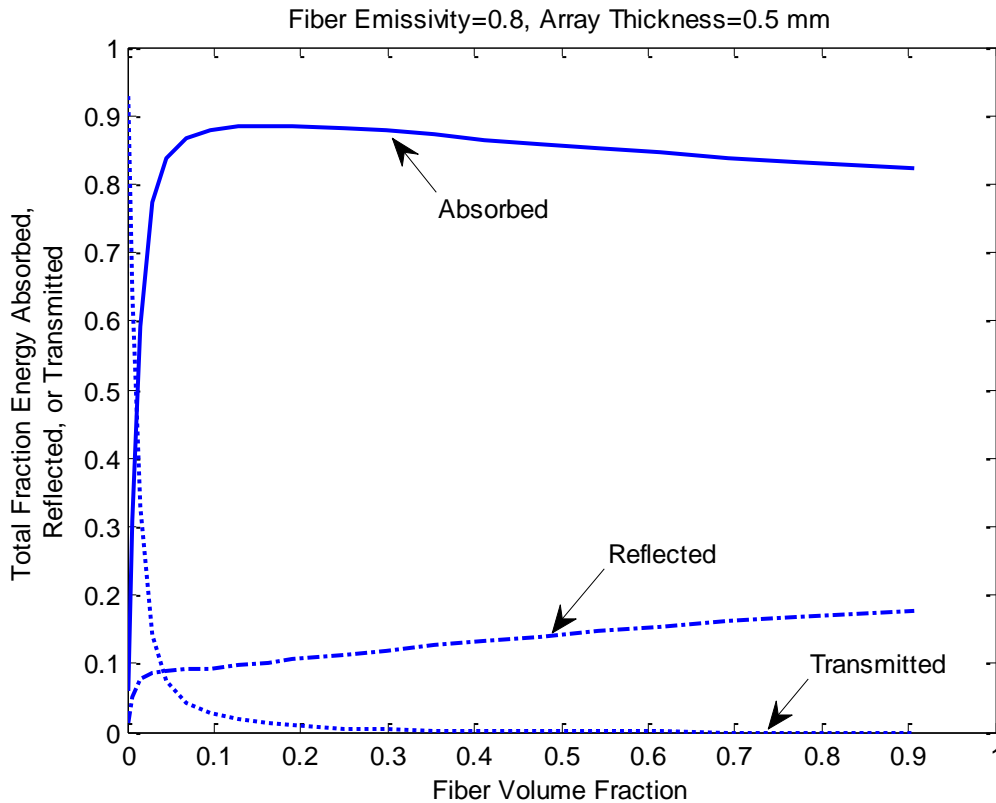
Figure 2.11: Fraction of total incident energy absorbed, reflected and transmitted versus fiber volume fraction for an array thickness of 0.5 mm, 50,000 multi-photon rays, and a fiber emissivity of 0.8

As shown in Figure 2.11, for very small volume fractions of less than about 0.01, the rate of transmission was dominant since the array was optically thin. As the fiber density increased, the transmittance decreased dramatically while the reflectivity increased slowly because more incident rays reflected out of the domain from the top rows of fiber. The transmittance dropped below 0.10 and 0.01 for volume fractions above about 0.05 and 0.15 respectively. Volume fractions above 0.15 for this 0.5 mm array were considered optically thick. The maximum effective emissivity occurred at a fiber volume fraction of about 0.16, which is due to a rapid increase in optical thickness as the area of the projected fibers onto the incident ray entrance plane approaches 100% of the plane. For optically thick arrays, the effective emissivity of the array was greater than the fiber surface emissivity due to multiple scattering events allowing for greater total emission to space. The range of volume fractions that yield optically thin conditions can be reduced by thickening the array, however thicker arrays will not significantly

affect the results for volume fractions above 0.15. As the array thickness decreases, the maximum

effective emissivity will occur at higher volume fractions that optimally balance transmission and

reflection, as the 0.16 volume fraction does for the 0.5 mm thick array.

Mitsubishi K13D2U carbon fiber tows are approximately 2 mm wide and 0.5 mm thick and

contain 2000, 11 μm diameter fibers, which yields a volume fraction of about 0.19. Since the fiber

volume fraction of the as-received fiber tows is very close to the predicted optimum volume fraction,

the Mitsubishi fiber tows have a near-optimal packing density for maximizing the effective emissivity.

Figure 2.12 shows the transmittance and effective emissivity as functions of fiber volume

fraction and number of fiber rows (i.e., array thickness). Transmittance decreased monotonically with

both volume fraction and fiber rows as the number of fibers a ray may encounter decreases. Effective

emissivity increased monotonically with number of fiber rows, but varied non-monotonically with fiber

volume fraction.
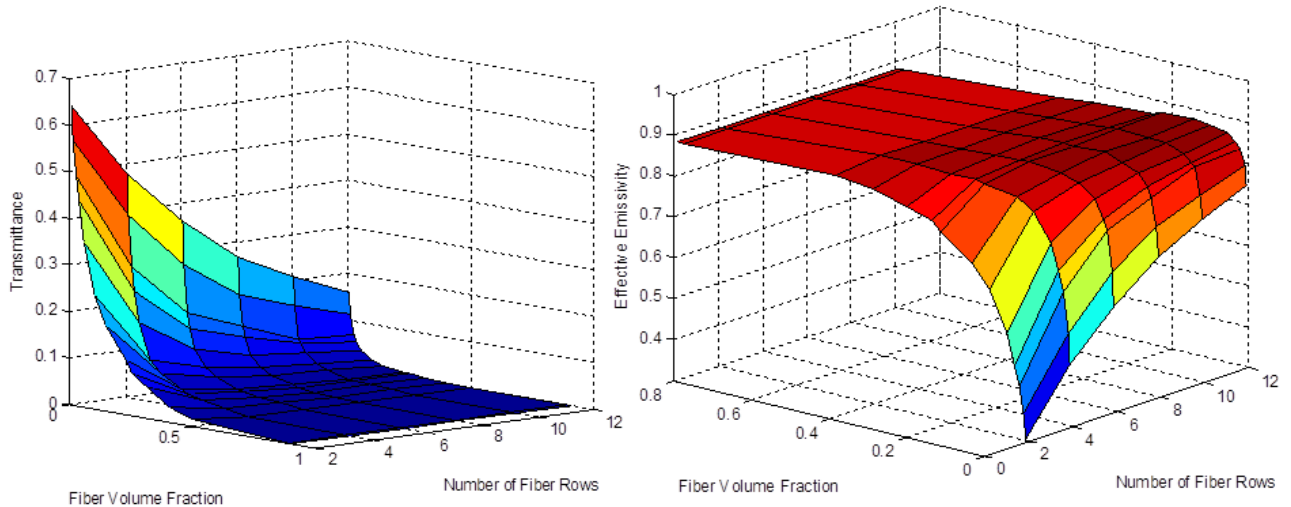
Figure 2.12: Surface plots of transmittance (left) and effective emissivity (right) versus fiber volume
fraction and the number of fiber rows for simulations with fiber emissivity of 0.8

To understand why the peak of the effective emissivity curve falls near a fiber volume fraction of

0.16, a validation exercise was conducted using normal, collimated incident radiation. By removing the

variability in the angle of incidence, a set fraction of the incident rays will be directly transmitted for

each volume fraction. As Figure 2.13 demonstrates, a definite peak in absorptivity occured at exactly

the volume fraction (0.2267) associated with the critical fiber spacing where the fibers start overlapping

as viewed from above. This volume fraction optimizes the balance between minimizing transmittance,

achieved by higher volume fractions, and minimizing total reflectance, achieved by lower volume

fractions.
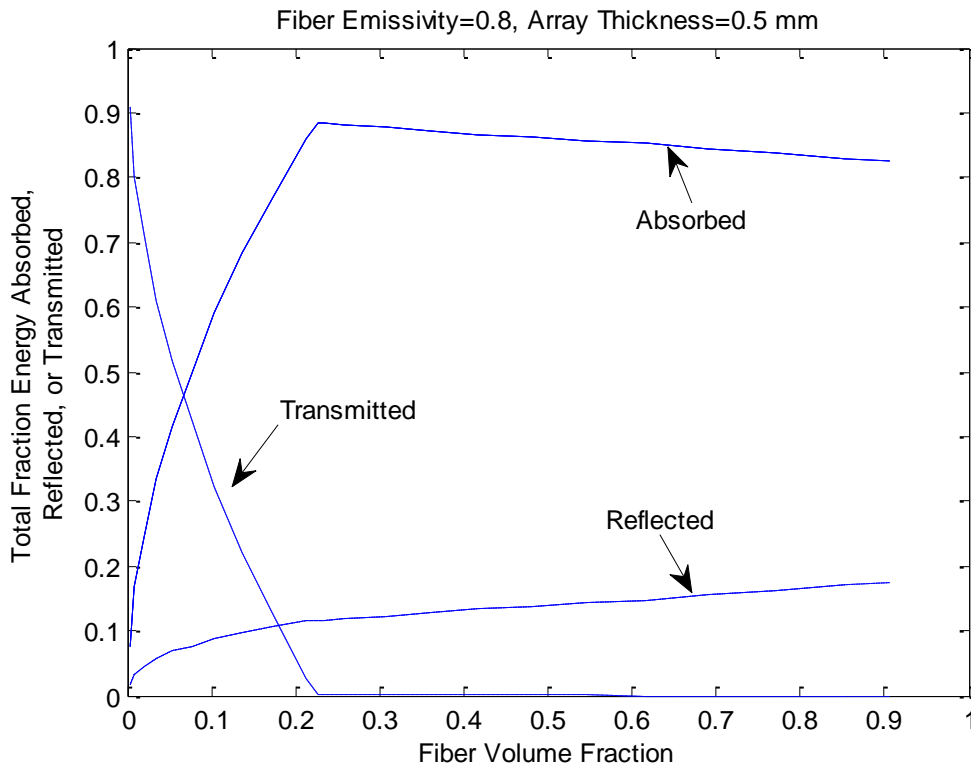
Figure 2.13: Fiber volume fraction versus total fraction of absorbed, reflected or transmitted energy for a 0.5 mm thick fiber mat, and fiber emissivity of 0.8

In terms of incident radiation normal to the array, having a zero degree angle of incidence, every

other angle of incidence will have a unique critical spacing value for fiber overlap that allows for direct

transmission. In other words, normal incident radiation has a single critical fiber spacing value, while

diffuse radiation does not. Thus, for diffuse incident radiation the effective emissivity curve has a less

defined peak because of the averaging effect of the critical spacing value over all incident angles.

Next, the effects of fiber surface emissivity are discussed. The total fraction of energy absorbed

increased with fiber surface emissivity since each time a ray collided with a fiber, more of its energy was

absorbed. This was demonstrated by the results shown in Figure 2.14, which gives the effective

emissivity versus fiber volume fraction for fiber surface emissivities of 0.6, 0.7, 0.8, and 0.9 for a 0.5 mm

thick array, and 50,000 multi-photon rays per simulation.
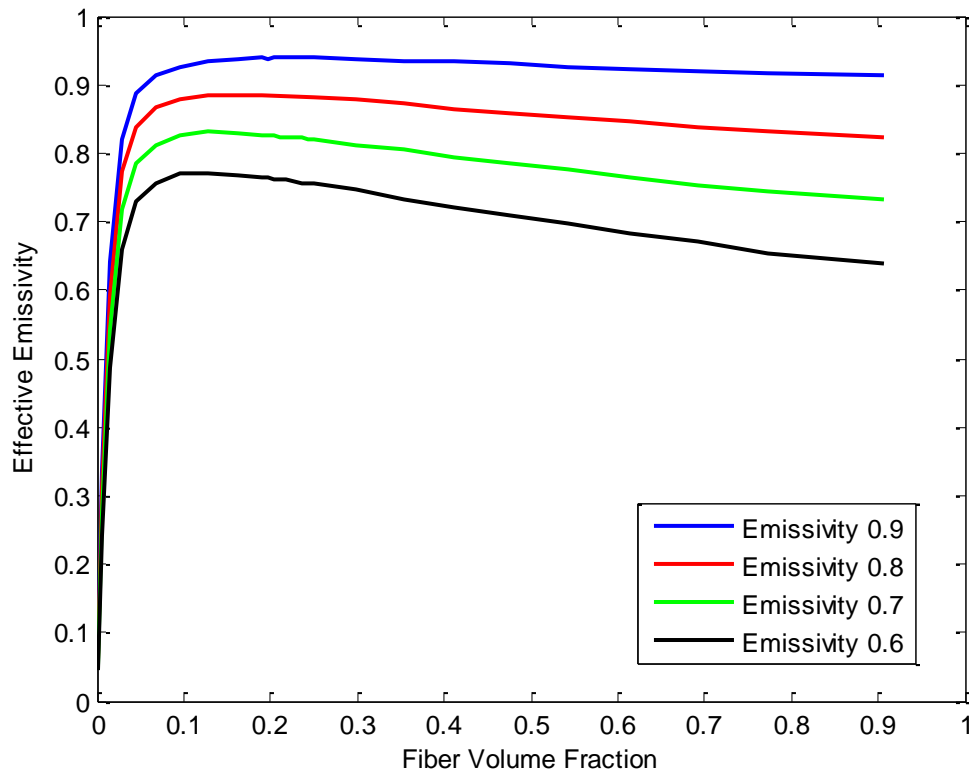
Figure 2.14: Effective emissivity versus fiber volume fraction for fiber surface emissivities of 0.6, 0.7, 0.8, and 0.9 for a 0.5 mm thick array, and 50,000 multi-photon rays per simulation.

The effective emissivity was greater than the fiber surface emissivity for volume fractions above

about 0.05. The maximum effective emissivity was generally greater than the fiber emissivity by slightly

less than half of the difference between one and the fiber emissivity, as shown in Figure 2.15. At

volume fractions higher than about 0.16, where the maximum occurs, the effective emissivity curves

decreased again approaching the fiber surface emissivity. The curves diverged slightly as reflectivity

effects became increasingly significant. Figure 2.16 gives the reflectivity versus fiber volume fraction for

the same set of simulations, which shows that the lower the fiber emissivity, the greater the slope of the

reflectivity curve. For lower fiber emissivities, more energy was reflected after each fiber interaction,

which makes the reflectivity more sensitive to volume fraction for the upper range of volume fractions.

For optically thick arrays, the added benefit of internal scattering, permitted by smaller volume

fractions, was more significant for lower fiber emissivities.   This was because direct reflection out of the

array after one fiber hit resulted in a significant loss of energy; however if the ray had hit two or more

fibers as it scattered in the array, most of the energy would have been absorbed. In the upper limit of

fiber surface emissivity of 1.0 (i.e., reflectivity=0), the peak of the effective emissivity curve, at the value

of 1.0, occurred at the volume fraction at which transmission is zero and remains at 1.0 for all greater

volume fractions. Finally, Figure 2.17 shows that the transmittance versus volume fraction was nearly

identical for all fiber emissivities since most of the transmitted rays were due to direct transmission (i.e.,

geometrical factors) versus transmission due to reflection from a fiber.
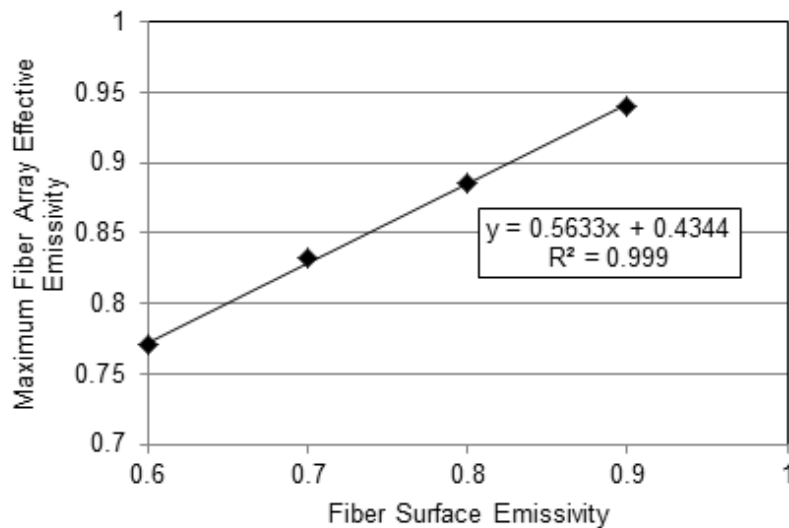
Figure 2.15: Maximum fiber array effective emissivity versus fiber surface emissivity for an array
thickness of 0.5 mm
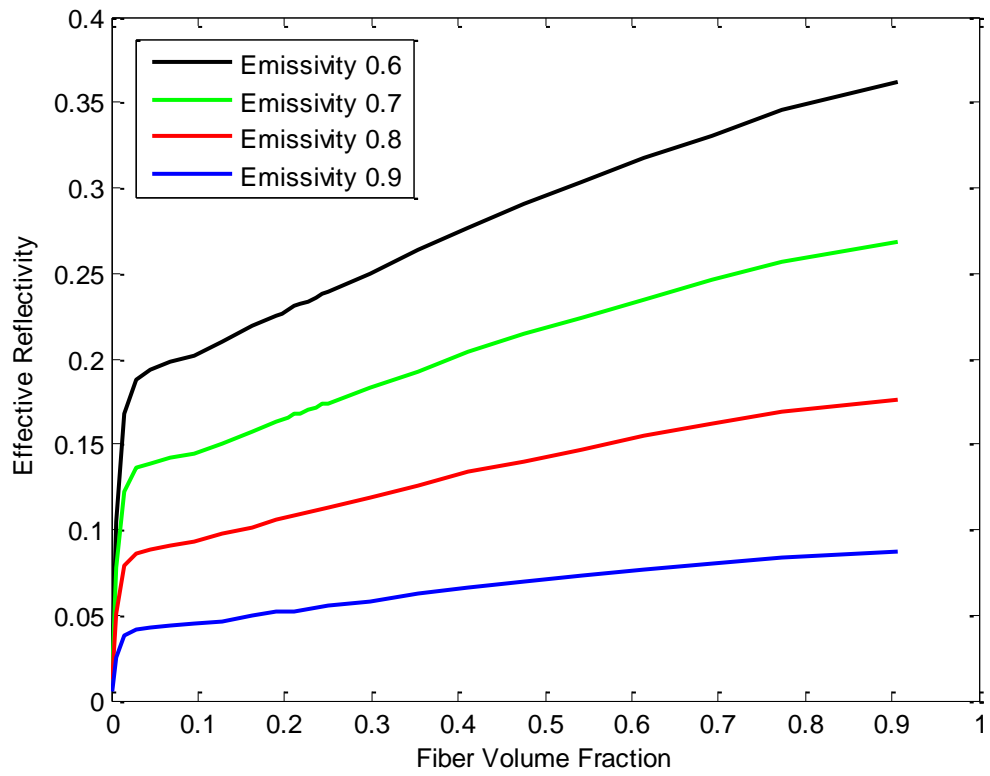
Figure 2.16: Effective reflectivity versus fiber volume fraction for fiber surface emissivities of 0.6, 0.7, 0.8, and 0.9
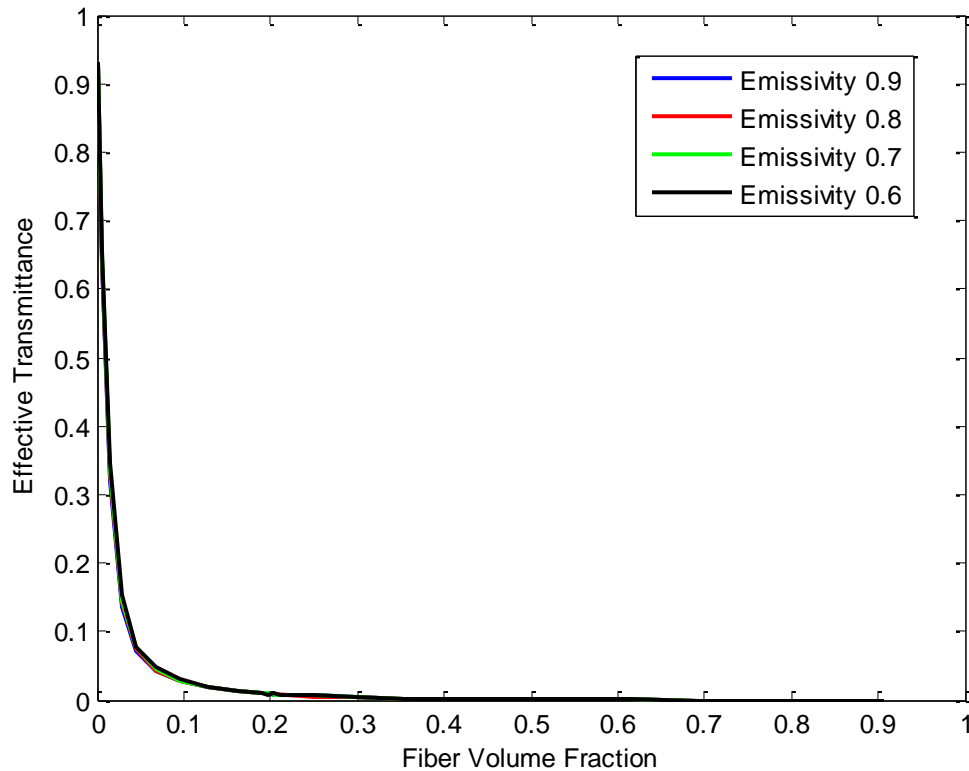
Figure 2.17: Effective transmittance versus fiber volume fraction for fiber surface emissivities of 0.6, 0.7, 0.8, and 0.9

Next, results from different ray types are presented. As long as the solution converges, the effect of ray type is negligible. Figure 2.18 gives results for simulations with single- and multi-photon rays for an array thickness of 0.5 mm and fiber emissivity of 0.8. As before, 50,000 rays were used for the multi-photon rays, but 100,000 single-photon rays were used since single-photon ray simulations converge slower. The percent error between the absorptivity values from the two ray types was less than 0.05% for all volume fractions. Therefore, these ray types can be used interchangeably.
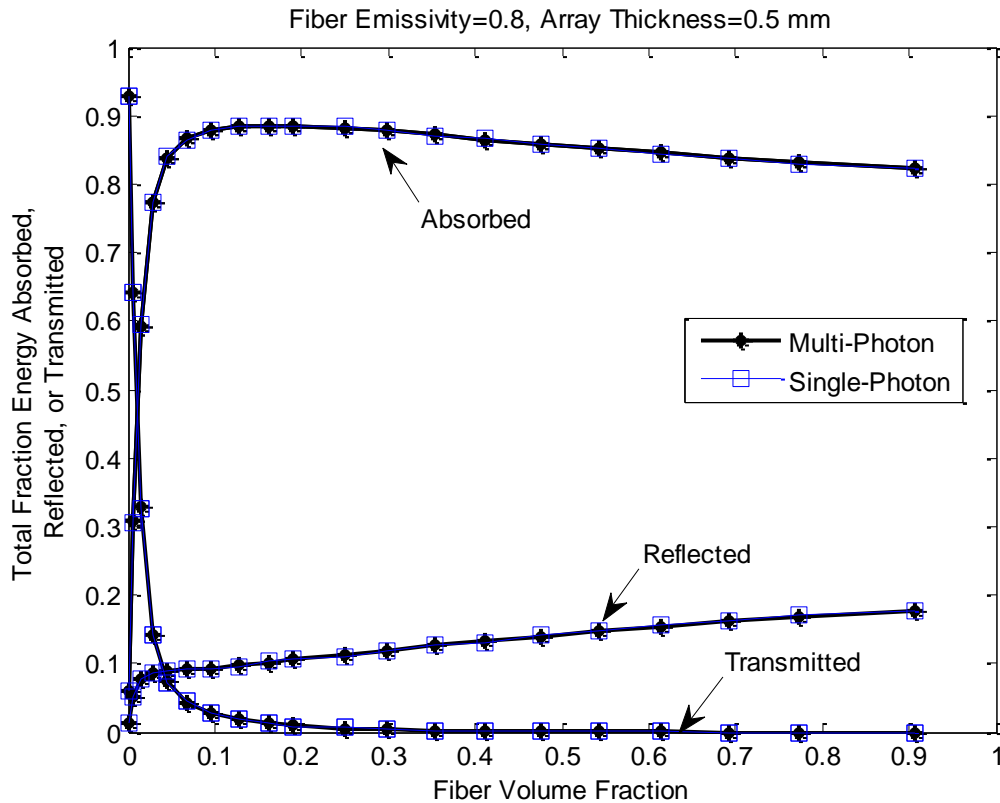
Figure 2.18: A comparison of absorptivity, transmittance, and reflectivity versus fiber volume fraction for single-photon and multi-photon rays, for a fiber emissivity of 0.8

One benefit of single-photon rays is that they allow for simple attenuation monitoring. The attenuation versus array depth can be determined by recording the depth at which each absorbed photon is absorbed. Figure 2.19 shows the percent of incident energy absorbed versus array depth for a wide range of fiber volume fractions. The stepped nature of these curves is due to the fact that radiation was absorbed only at depths containing fibers. It was clear at the lower volume fractions how many fibers were in the array by counting the steps in the attenuation curve. As the fiber density increases, the steps became less pronounced. For optically thick arrays, the attenuation curve reached 100% before the bottom boundary of the array.
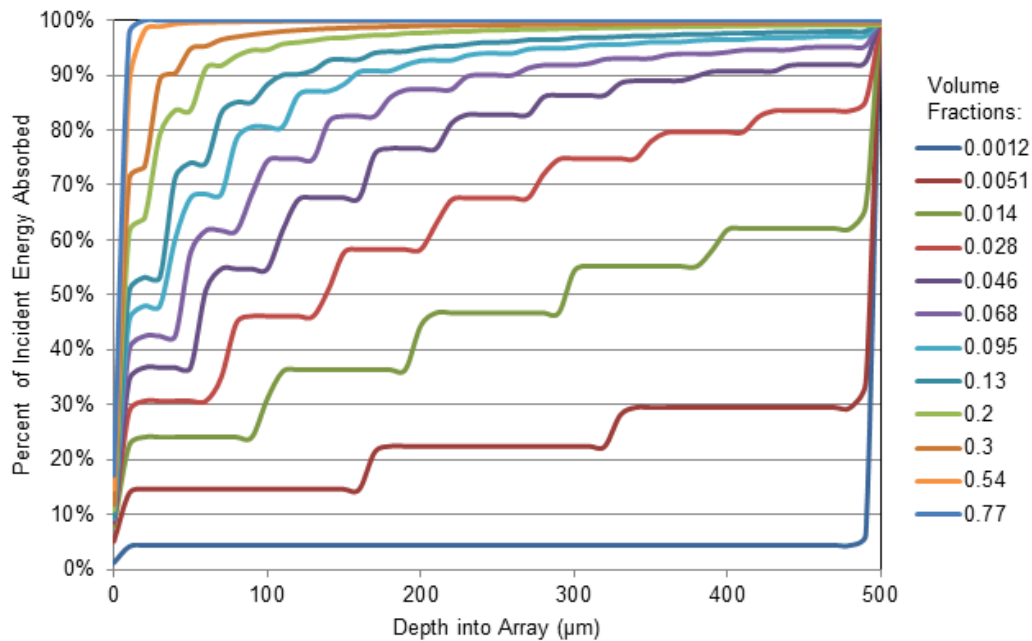
Figure 2.19: Percent of incident energy absorbed versus depth into array for a range of fiber volume fractions (array thickness=0.5 mm, fiber emissivity=0.8, 100,000 rays)

2.5   Conclusions

This study confirmed that as long as a carbon fiber weave is optically thick, the porosity in the weave improves the effective emissivity. The significance of fiber volume fraction increased with decreasing fiber surface emissivity. The effective emissivity was greater than the fiber surface emissivity for volume fractions above about 0.05. The maximum effective emissivity was generally greater than the fiber emissivity by slightly less than half of the difference between one and the fiber emissivity. Volume fractions above the point at which the maximum effective emissivity occurs, 0.16 for 0.5 mm thick arrays, the effective emissivity tended toward the fiber surface emissivity. However, even at the maximum fiber packing density the effective emissivity was greater than the fiber emissivity.

CHAPTER 3

DESIGN AND FABRICATION OF HIGH THERMAL CONDUCTIVITY CARBON FIBER RADIATOR TEST ARTICLES

3.1   Introduction

This chapter describes the work done to design and build novel carbon-fiber-heat-pipe radiator test articles, which are used to test the feasibility of the proposed concept. The test article design involves identifying a sub-scale section of the radiator that sufficiently represents the important characteristics of a full-scale radiator. Since the ultimate goal of this project is to develop a radiator that meets NASA's areal density targets, the test articles are designed with that goal in mind by optimizing the dimensions to maximize specific power (kW/kg). Test article fabrication involved much experimental work on developing best practices for building the carbon fiber fin and attaching the fin to a heat pipe. Protocols and recommendations were developed for these fabrication steps.

This chapter consists of four main sections. The first section describes the basic design of the test article. The following three sections detail the more focused design and fabrication work on the fin, fin and heat pipe joint, and heat pipe.

3.2   Test Article Design

The test articles were designed to be as small as possible while demonstrating the key physics of the system. Based on previous studies [20][26][27][28], a full-scale radiator for NEP will require hundreds of parallel heat pipes with fin material spanning the distance between pipes as shown schematically in Figure 3.1. To capture the primary building units of the radiator, the test article was designed to include a small section of a heat pipe with a fin that is half of the distance between heat pipes in length, with the following considerations. It was estimated that a 3-inch-long heat pipe section with a fin would be sufficient to eliminate significant thermal edge effects in the fin. Using half of a fin uses the natural symmetry boundary to reduce redundancy and will not affect the heat rejection

performance. There is no heat flux at the symmetry line in the full-scale model. The only heat flux from

the free edge of the test article (i.e., the cut ends of the fibers) is by radiation, which is negligible since

the radiating surface area is extremely small relative to that of the front side of the fin. Lastly, since the

radiator panels in the full-scale system are expected to be entirely co-planar, fins will have a view factor

to space approaching unity. This can be approximated by testing the articles in a black, isothermal

vacuum chamber, ideally with a liquid nitrogen cold wall that can maintain the chamber wall

temperature as low as to 77 K.
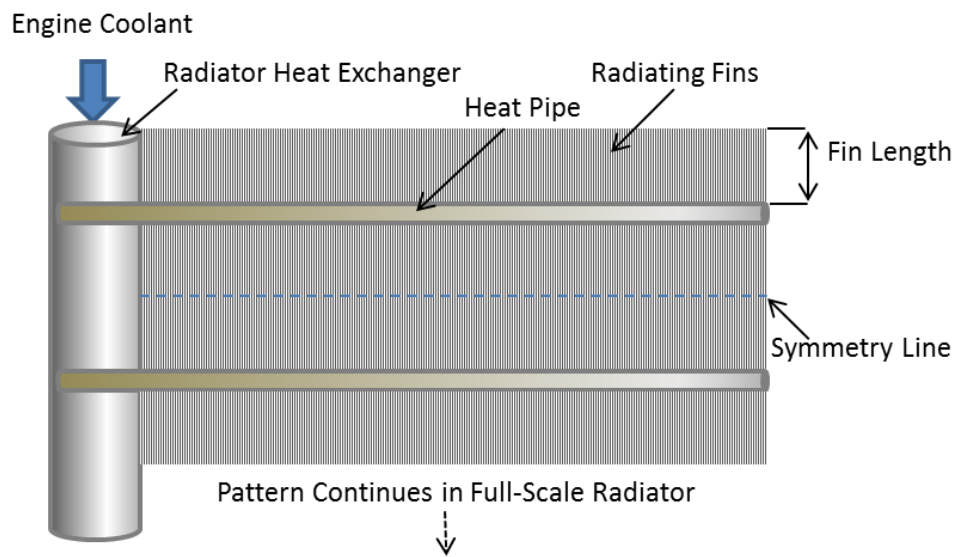
Figure 3.1: Schematic of full-scale radiator section

The first test article design consisted of a 3-inch-long simulated heat pipe and a carbon fiber

mat, as shown in Figure 3.2. The initial fin thickness and length were selected by running a parameter

sweep in the numerical model described below over the two dimensions and finding the combination

that maximized the specific heat rejection (W/kg) of the heat pipe and fin assembly. Matlab was used to

execute the parameter sweep, calling the finite element software Comsol Multiphysics (Comsol) to

calculate the specific heat rejection for each parameter set.
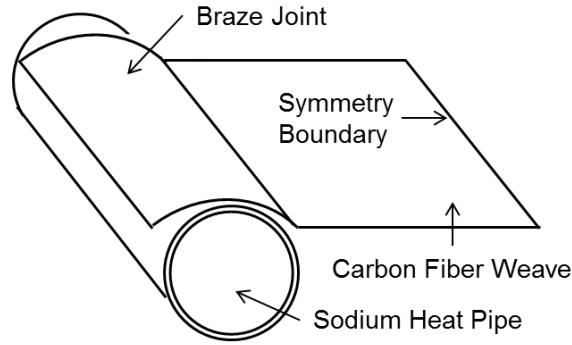
Figure 3.2: Schematic of radiator fin test article

The heat rejection was calculated using a 2 dimensional heat transfer model of the fin cross-section shown in Figure 3.3 with the governing equation and boundary conditions given in 3-1 through 3-5. The heat pipe temperature at the fin root, T_1, is assumed to be 600°C, which is a reasonable target heat rejection temperature of the high-power NEP systems. This model neglects variations in the z-direction (along the heat pipe) as the heat pipe is assumed to be isothermal. Radiation between the heat pipe and fin was considered negligible in this model for simplicity. Using more sophisticated models in Chapter 5 showed that adding the heat pipe radiation changes the power rejected by no more than 10%. Even with these simplifications, the problem cannot be solved analytically. Comsol was used to solve for the fin surface temperature profile. The total radiated power per unit length of heat pipe was determined by integrating Equation 3-5 over the fin surface, as given in Equation 3-6. In these equations, L_f and t_f are the fin length and thickness as shown in Figure 3-3, and L_{HP} is the length of the heat pipe normal to the page. When modeling a carbon fiber fin with a finite percentage of void space, t_f is taken as the effective thickness when the fiber volume fraction is 1.
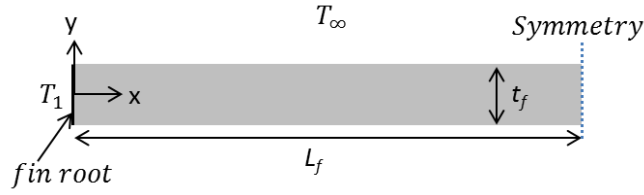
Figure 3.3: 2-D fin heat transfer problem solved in Comsol

$$\frac{\partial^2 T}{\partial x^2} + \frac{\partial^2 T}{\partial y^2} = 0 \tag{3-1}$$

$$T(0, y) = T_1 \tag{3-2}$$

$$\frac{\partial T}{\partial y}(x, 0) = 0 \tag{3-3}$$

$$\frac{\partial T}{\partial x}(L_f, y) = 0 \tag{3-4}$$

$$q\left(x, \pm \frac{t_f}{2}\right) = \varepsilon\sigma\left(T\left(x, \pm \frac{t_f}{2}\right)^4 - T_\infty^4\right) \tag{3-5}$$

$$Q = L_{HP} \int_{x=0}^{x=L_f} \varepsilon\sigma\left(T\left(x, \pm \frac{t_f}{2}\right)^4 - T_\infty^4\right) dx \tag{3-6}$$

Dividing the power rejected by the total mass of the fin and heat pipe gives the specific heat rejection (W/kg). The assumed heat pipe for this calculation was a 0.75-inch diameter Inconel shell with sodium working fluid. The results from the fin parametric study are given in Figure 3.4. The maximum specific heat rejection occurs near the point $L_f = 8$ cm, $t_f = 0.3$ mm. The radiator test articles were built with these approximate dimensions.
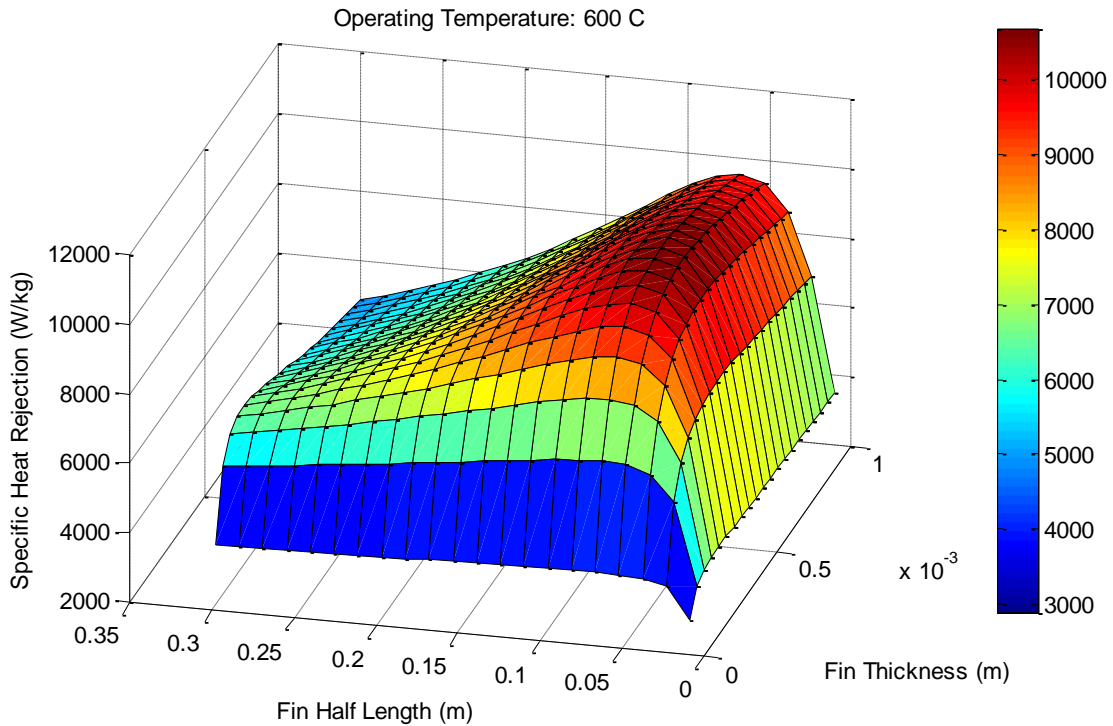
Figure 3.4: Specific heat rejection for various fin lengths and thicknesses given a 600°C heat pipe, fiber emissivity of 0.85, and fiber thermal conductivity of 800 W/m-K

Figure 3.5 shows the trends of optimum fin thickness and length versus heat pipe temperature. This may be of interest during the design of a full-scale heat rejection system, since the heat pipes would not all operate at the same temperature. For example, the coolant temperature decreases as it dissipates energy to the radiator, so the heat pipes near the radiator inlet would be much hotter than those near the outlet. As part of a system-level design study, the heat pipe spacing could be varied with the decrease in coolant temperature to minimize the radiator mass. For such a design, the trends shown in Figure 3.5 are useful. Figure 3.6 shows the heat rejection per unit length of heat pipe versus heat pipe temperature for fins of the optimal dimensions given in Figure 3.5.
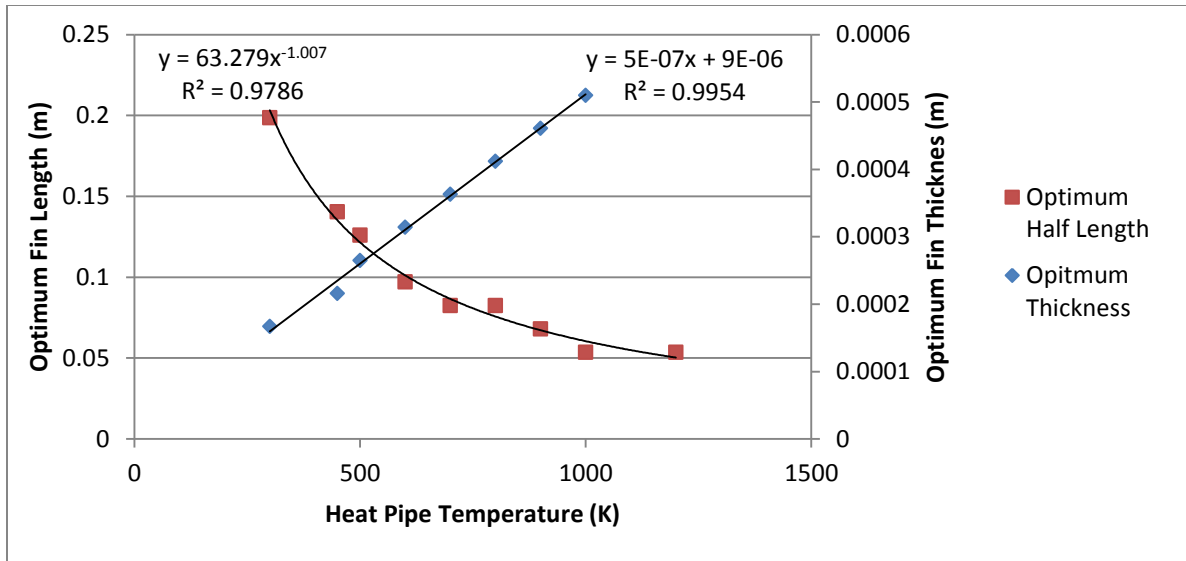
Figure 3.5: Carbon fiber fin length and thickness dimensions that maximize specific heat rejection of the fin and heat pipe versus heat pipe temperature. Length decreases with temperature because fin radiation is dominated by the hottest section. Thickness increases because the radiative flux in each differential area of fin is greater with temperature, thus more heat must be supplied by conduction.
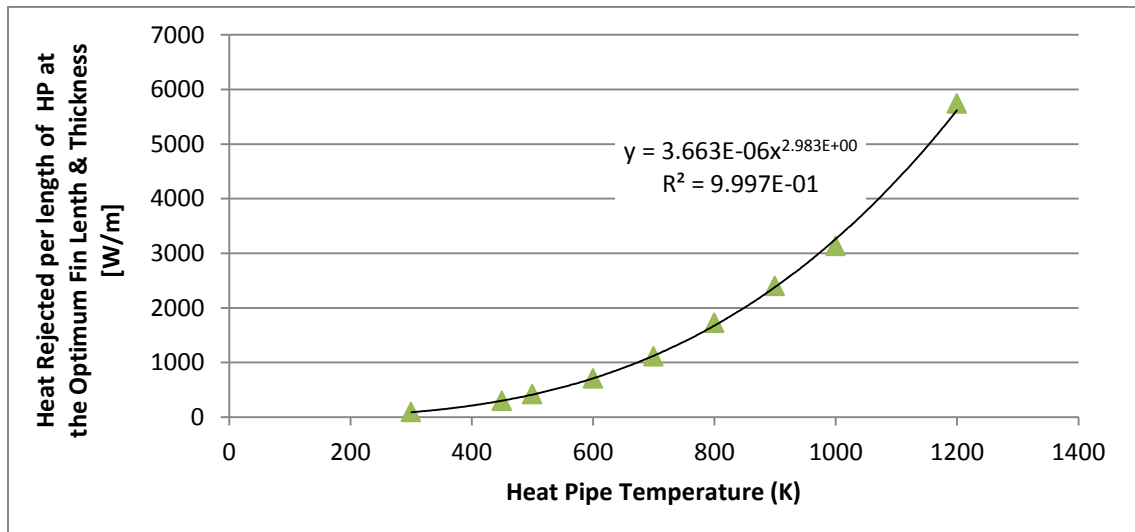
Figure 3.6: Heat rejected per unit length of heat pipe for fins with the optimal dimensions shown in Figure 3.5 versus heat pipe temperature. This trend shows a power law relationship slightly less than T^4 because the fins are not isothermal and the fin dimensions vary with temperature.

After establishing the target test article dimensions, experimental fabrication studies were

conducted.

3.3 Fabrication of Carbon Fiber Fins

With a target test article design, fabrication work commenced. The first step was to develop protocols for forming the carbon fiber fin. The pitch carbon fiber used here was manufactured by Mitsubishi, product Dialead K13D2U. This product has the highest thermal conductivity of all the carbon fiber products currently available from Mitsubishi or any other carbon fiber manufacturer. Higher-conductivity fibers have been fabricated for research applications but were not available in bulk for purchase at the time of this work [78]. Table 3.1 gives the material data provided by Mitsubishi.

Table 3.1: Dialead K13D2U Product Typical Properties

Number of Fibers per Tow	2,000
Fiber Diameter	11 μm
Carbon Content	>99%
Sizing Amount (Epoxy)	2%
Thermal Conductivity	800 W/m·K
Electrical Resistivity	1.5×10^{-6} ohm·m
Density	2.21 g/cm^3
Tensile Strength	3.7 GPa
Tensile Modulus	935 GPa
Ultimate Elongation	0.40%
"Yield" (linear density)	3.65 mg/cm

At this time, there is no commercially available textile made from the Dialead K13D2U fibers, so fiber handling and weaving methods were developed. The as-received fiber comes as a spool of continuous fiber tows. This section describes the evolution of the carbon fiber fin from initial attempts at constructing fins from bundles of unwoven fibers to successfully commissioning an industrial textile company to produce a textile suitable for this application.

At the start of this research, it was unclear whether or not the fibers could be woven, so the first test article, TA-A, was made with unwoven fibers by Trudy Allen and Mike SanSoucie of NASA MSFC.

Due to the high fiber modulus, the fiber tows were hard to handle and form into flat mats. The resulting

attempt is shown in Figure 3.7. There were two major issues with using unwoven fiber tows: 1) the tows

were not held in place prior to brazing, so keeping the tows well-organized was infeasible, and 2) with

the highly non-uniform and curved fin surface, recording the surface temperature using IR imaging was

impractical. As described in Chapter 4, the ability to record the temperature profile along the fin length

was a key capability in order to estimate the thermal conductivity and quantify the fin heat rejection.

For these reasons it was decided that weaving the fiber tows was important to the design.

Figure 3.7: Test article A with an unwoven carbon fiber fin

Five main objectives were identified for the fiber weaving method: 1) achieve a high density of

tows in the longitudinal fin direction (i.e., normal to the heat pipe), 2) use a minimum number of cross

tows (i.e., parallel to the heat pipe) while keeping the longitudinal fibers in order, 3) ability to control the

thickness of the weave, 4) ability to produce a uniform weave, and 5) demonstrate or propose how the weave could be mass-produced. Through several iterations, all of these objectives were met.

Two weaving methods were developed using a table-top hand loom built with hair combs, cardboard, and knitting needles. Two combs were arranged with the teeth pointing upward and carbon fiber tows were threaded between the combs and taped at each end to hold them in tension. In the textile industry, these tows held in the loom frame are called warp tows. This was the starting point for both methods. Without advanced weaving tools available, this inexpensive loom design was used for experimentation and demonstration purposes.

The intent of this first method was to make a fin with many parallel fiber tows in a flat sheet so that they could be more easily transferred to the heat pipe. Woof tows were sparsely woven through the warp tows for the sole purpose of keeping the warp fibers organized. Smooth knitting needles helped guide the delicate weaving process. Figure 3.8 shows test article B, TA-B, made using the first weaving method where the warp fibers are normal to the heat pipe axis. This was a great improvement over the unwoven fin because the fibers were easier to handle and the weave was nearly flat, however it did not meet objectives 1, 3 and 4. The biggest issue was that the comb teeth limited the packing density of the warp fibers. Undesirable voids between the longitudinal tows can be seen in Figure 3.8.
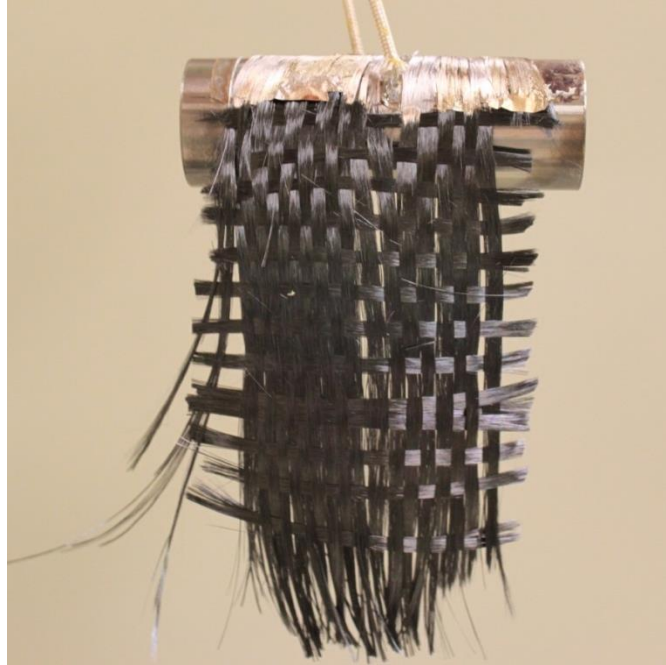
Figure 3.8: Test article B with a fiber fin generated using the first weaving method

Driven by the packing density limitations of the comb-tooth spacing, the second weaving

method was developed. In this method, the intent was for the woof tow orientation to be aligned with

the longitudinal fin direction instead of the cross direction. Since a high tow density is desired in the

longitudinal fin direction, changing the orientation of the weave facilitated that goal. Nothing limits the

packing density of the woof fibers except the ability to compress the tows in the loom. By using the

woof tows in the longitudinal fin direction, the packing density of the woof tows could be maximized

while keeping the density of the warp fibers as low as possible. A high-temperature ceramic adhesive

called Ceramabond 865 was used in small amounts to hold the fibers in place near the fin tip. Figure 3.9

shows TA-C, which was made with a sample of the weave generated using the second method, and

proved to be a vast improvement over TA-B. Figure 3.10 shows the hand loom.

Figure 3.9: Test article C with a fiber fin generated using the second weaving method
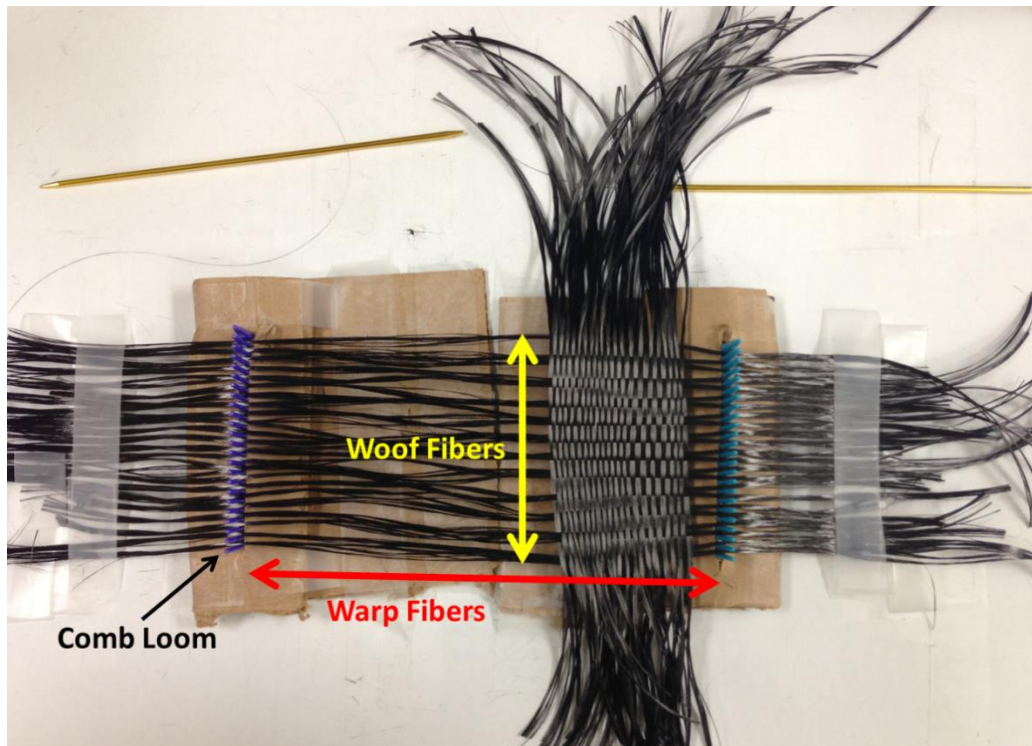
Figure 3.10: Hand loom used to weave carbon fiber fin test articles; second weaving method in use

The uniformity and longitudinal tow density, objectives 1 and 4, were vastly improved by the

second weaving method. Objective 2, achieving a low density of cross tows, was met by both methods

since spacing apart either the warp or woof tows was straightforward. Objective 3, the ability to control

the thickness, was still limited by the nature of a single-layer weave pattern. The target nominal thickness of 0.3 mm could not be achieved in one layer of weave. Stacking multiple layers of the weave would be required to achieve the desired thickness. To further improve the weave, a more advanced loom and weaving method was necessary.

Objective 5 was met by consulting a textile manufacturing company. A survey of textile manufacturers was conducted to assess the feasibility of creating a textile using the K13D2U material. A company called Textile Engineering and Manufacturing Inc. (TEAM) was contacted because they had experience weaving Mitsubishi's lower conductivity K13C2U pitch carbon fiber and had a loom that could weave thick 3-dimensional textiles. Without having direct experience with K13D2U fiber, TEAM predicted that they could fabricate a textile and meet the five objectives.

With financial support from MSFC, TEAM was commissioned to research and develop a weaving method to prove that the K13D2U fibers could be woven into a dense, thick mat on a mass-scale. To achieve a thickness of 0.3 mm, TEAM designed a 3-dimensional weave with 3 layers of pitch fiber tows as shown schematically in Figure 3.11. TEAM was asked to use K13D2U pitch carbon fiber supplied by MSFC as the woof fibers, as was done in the second hand-weaving method, and to use low modulus PAN carbon fibers as the warp fibers to increase the textile flexibility and likelihood of success for this first attempt. Since PAN fibers have a much lower modulus than pitch, using them in the warp direction was expected to provide the greatest chance of weaving without warp tow breakage. As discussed in Section 1.2.4, increasing crystallinity of the graphene layers in the carbon fibers increases the modulus, thermal conductivity and critical bend radius, and decreases the fracture resistance.
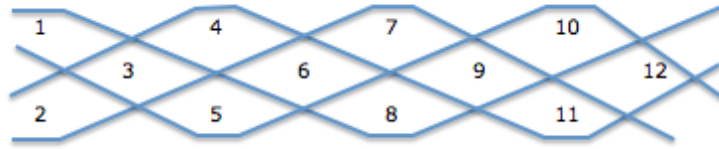
Figure 3.11: Cross section detail of the TEAM textile. Blue lines representing PAN tows and numbers representing pitch tows (courtesy of Steve Clarke at TEAM)

TEAM manufactured the textile in April, 2014, and was so successful that they delivered over twice the promised quantity. The end product had 50 pitch tows per inch and 20 PAN tows per inch.

TEAM reported that they were able to automate the process, proving the feasibility of mass-producing the textile. Confirming this ability was a crucial benchmark in the development of the carbon fiber radiator concept since most space power systems will require on the order of hundreds of square meters of fin surface area. Figures 3.12-3.14 show several images of the TEAM textile.
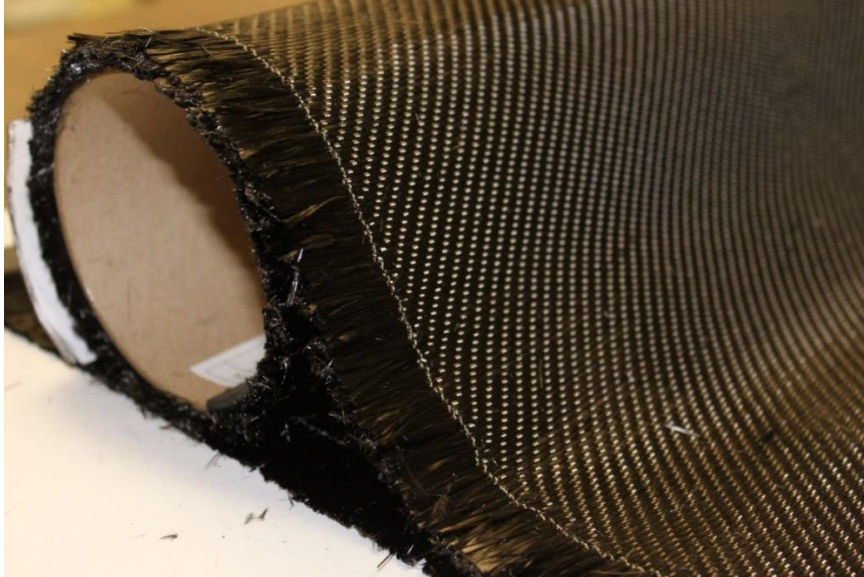
Figure 3.12: Carbon fiber textile manufactured by TEAM, showing the weave pattern

Figure 3.13: Carbon fiber textile manufactured by TEAM showing that a long, continuous sheet of the material can be produced
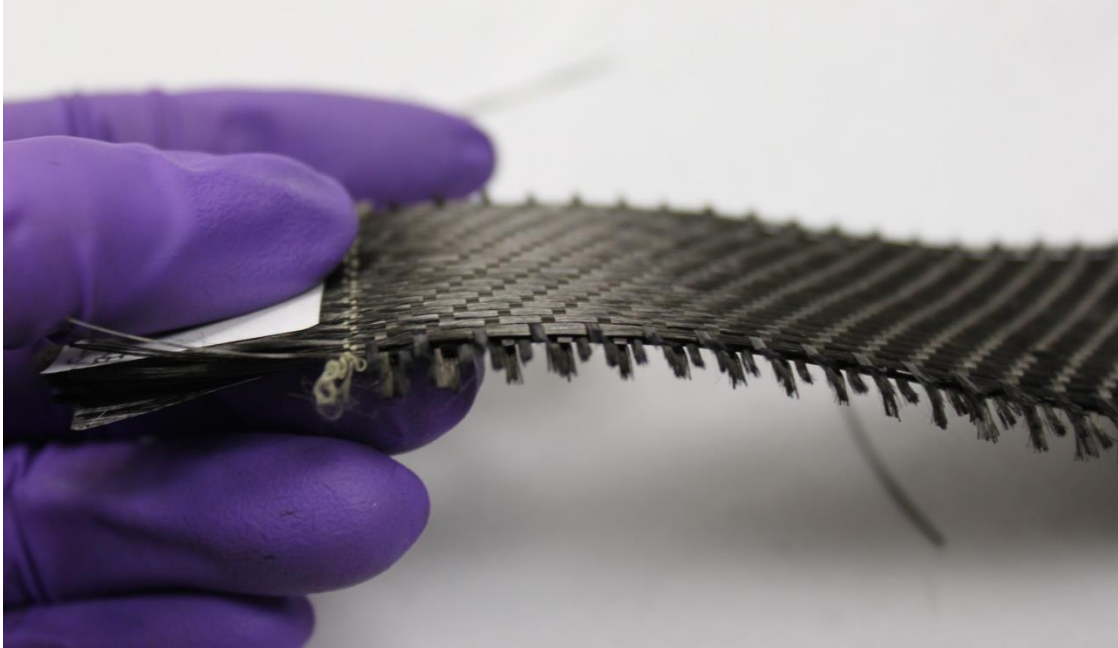
Figure 3.14: Carbon fiber textile manufactured by TEAM showing the cross section and the transverse PAN fibers

This textile was the most advanced fin material studied in this work. Future work on the weave design should involve replacing the PAN warp tows with K13C2U pitch tows. Now that TEAM has experience with the K13D2U fiber, they are confident that this same weave pattern could be achieved using K13C2U fiber in the warp direction.

3.4   Fin and Heat Pipe Joint

The second step was to select a fin attachment method and to develop a protocol for this process. Various attachment methods were explored for how best to secure carbon fiber fins to heat pipes.

3.4.1   Joint Design

The major considerations are summarized in Table 3.2. The attachment method must secure the fin to the pipe and promote efficient heat transfer. The attachment method must be able to function at the target operating temperature of 600°C, which disqualifies most polymeric materials

typically used as adhesives in lower-temperature radiators **Error! Reference source not found.**[26][27].

Lastly, chemical compatibility is important to avoid reactions that could degrade the thermal or

structural properties of the component over long-duration missions.

Table 3.2: Carbon Fiber Fin-Heat Pipe Attachment Considerations

1.)	Ability to keep fin securely attached to heat pipe during all phases of the mission (i.e., launch, deployment and operation)
2.)	Low thermal resistance between heat pipe and fibers
3.)	Withstand an operating temperature of 600°C
4.)	Chemically compatible with heat pipe shell and carbon fiber

Dry mechanical joints, such as tying or clamping the fin to the pipe, are typically simple to

assemble but the thermal resistance would be relatively high due to void spaces and smaller contact

areas at the interfaces. Liquid chemical attachment methods, such as brazing or ceramic adhesives, can

fill the voids between the fibers and pipe, providing a direct path for heat conduction. Chemical

methods are typically more complex than mechanical since there is a usually a phase change and

chemical interactions between the bonding agent and two substrates. Due to the promise of increased

contact area, chemical joining options were evaluated.

Operation at high temperatures limits the chemical bonding agents to ceramic and metallic

materials. Ceramic adhesives can be applied directly to the fin and heat pipe as a paste and then cured

at elevated temperatures, typically near 200°F. With the aid of auxiliary tie wires to secure the fibers

before curing, the ease of application is a benefit of the adhesive. The disadvantages of ceramic

adhesives include very low thermal conductivity (<1 W/m-K for most Aremco products), and wettability

issues with the metal heat pipe and fibers. Since ceramic pastes do not wet to carbon fibers, the edges

of the hardened ceramic are sharp. This introduces stress concentrations, which cause the fibers to

break easily at that boundary. Ceramic adhesive options were rejected because the disadvantages appeared more significant than those found with the simple mechanical clamp.

Of the metallic bonding methods (i.e., solder, welding, brazing), brazing is the most suitable for this application. Solder joints melt below 600°C, and typical welding processes are not suitable because the fibers would have to be welded in between a filler metal and the heat pipe shell, which would damage the fibers and is likely infeasible. Brazing is essentially a high-temperature solder where a filler material is added in between the substrates and melted to form the chemical bond. This liquid-phase process can be used for ceramic-metal joining since the molten filler metal can diffuse into both substrates and fill the voids between surfaces. The thermal expansion coefficient mismatch between most ceramics and metals can be a significant issue for using this type of bond in an application with thermal cycling. This mismatch can cause cracks and delamination of the ceramic. A heat pipe radiator study at NASA Glenn Research Center (GRC) showed that brazing a sheet of carbon-carbon composite to an Inconel heat pipe was very difficult and delamination challenges were not overcome [41]. Brazing small-scale fibers to a metal substrate, however, does not present the same thermal expansion issue because strain relief occurs at each fiber.

While brazing is one of the most complex joining methods, there are several significant advantages. First, since the filler melts and fills the voids between substrates, a direct heat conduction path forms with highly conductive metallic material. In that same study on brazing a carbon-carbon composite conducted at NASA GRC, the thermal resistance of the braze joint was negligible where delamination did not occur [80]. The other major benefit of brazing over a ceramic adhesive is that a braze filler can be selected that bonds very well with both carbon fiber and any potential heat pipe shell material. Based on the advantages of brazing over other chemical and mechanical bonding methods, brazing was selected for this work.

3.4.2   Evaluation and Selection of Brazing Material

There are several classes of brazing filler metals appropriate for various combinations of substrate materials and operating temperatures. The class of filler metals used to join ceramics and metals is called "active braze alloys." These contain titanium, the active component, that wets especially well to carbon-based ceramics [80][81][82]. When the filler melts, the titanium tends to diffuse to the ceramic surface forming an interfacial layer. Adding titanium to a silver or copper braze alloy has been shown to improve the wettability with graphite by reducing the wetting angle from around 140° to nearly 0° through the formation of carbides [80]. Table 3.3 lists the active braze alloys commercially available from Wesgo Metals.

Active braze alloys are often used for brazing refractory metals including stainless steel and nickel-based alloys, since active brazes can wet to surface oxides. Compatibility with nickel alloys and other refractory metals is important to this work since the heat pipe shell will likely be Inconel (Nickel-Chromium-Molybdenum). While any of these filler alloys should work with carbon fiber, Ticusil was selected for this project because it is available as a foil, which is easy to handle, and it has a moderate mole fraction of titanium. A certain amount of titanium is required to wet to all carbon surfaces, but since titanium has a much lower thermal conductivity than silver and copper, excess titanium is not desirable. Ticusil, having only 4.5 % titanium, offered a balance between the two competing factors and was a good candidate for this work. In addition, Ticusil is the most commonly used active braze alloy for ceramic-to-metal joints [82], so it was a low-risk option.

Table 3.3: Wesgo Metals Active Braze Alloys [83]

Name	Nominal Composition %	Liquidus (C°)	Solidus (C°)	Thermal Conductivity (W/m-K)	Form Availability
Tini-67	Ti -67.0 Ni-33.0	980	942	Not Available	Paste
Ticuni	Ti-70 Ni-15 Cu-15	960	910	Not Available	Paste
Ticuni-60	Ti-60 Ni-25 Cu-15	940	890	Not Available	Paste
Silver-ABA	Ag-92.75 Cu-5 Al-1 Ti-1.25	912	860	344	Paste
Ticusil	Ag-68.8 Cu-26.7 Ti-4.5	900	780	219	Foil, Paste
Cusil-ABA	Ag-63 Cu-35.25 Ti-1.75	815	780	180	Wire, Foil, Paste

3.4.2.1 Brazing Procedure

The basic brazing steps are summarized as follows:

(1) Assemble component to be brazed: insert filler foil/paste between substrates and compress the joint.

(2) Insert assembly into furnace and remove the oxygen by evacuating the volume or purging with inert gas, typically argon.

(3) Heat assembly to just above the liquidus temperature of the filler metal and hold there until it melts completely. Some manufactures provide a heating profile as a guideline, but the hold durations vary depending on the heat capacity of the assembly. Ideally, all joining surfaces are isothermal when the filler melts so that the hotter surfaces do not deplete the active component from the bulk of the filler metal, thus reducing the wettability of the filler with the cooler surfaces [84]. Experimentation is required to

determine a suitable heating profile for a specific joint. For joints where the filler

material is visible, a furnace viewport can be used to observe the melt, helping to

determine when the process is complete.

(4) Cool the sample. Joints between two dissimilar materials sometimes require a

controlled cool-down to help relieve the stresses caused by thermal expansion

differences. Fortunately when brazing carbon fibers, thermal strains do not build up

across the joint because each fiber acts independently, allowing only negligible strains

to accumulate at the fiber surfaces. Thus, natural cooling is permitted when brazing

fibers.

(5) Remove sample when the furnace cools below 100°C.

To prepare the sample for brazing, the fiber weave was layered between rectangular pieces of

Ticusil foil, 2 cm by 5 cm, and then secured to the heat pipe using a temperature resistant metal wire

(e.g., Constantan or stainless steel). The wire kept the three layers tightly compressed to help the filler

wick into the weave and bond with the pipe. Figure 3.15 shows the pre-braze assembly.
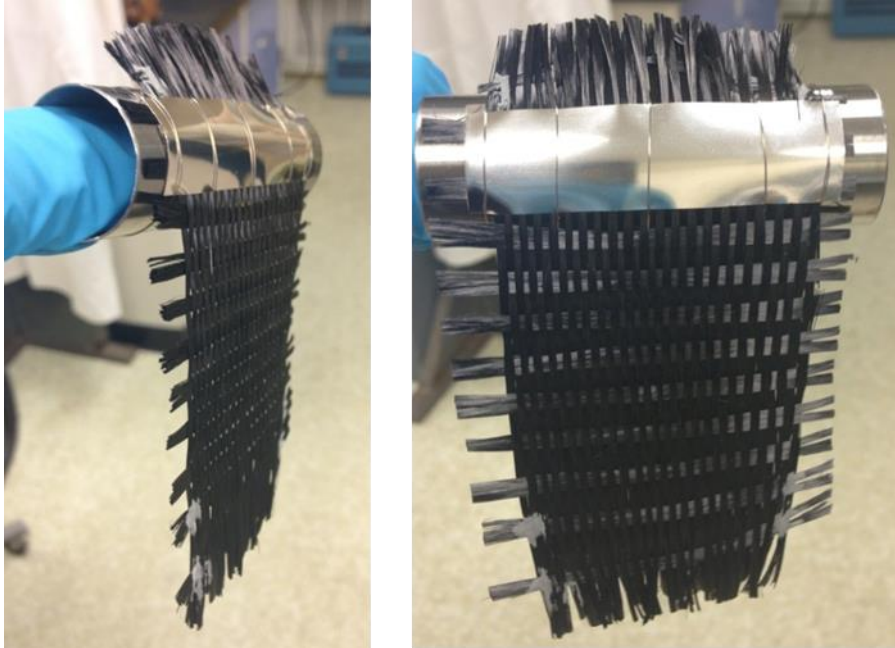
Figure 3.15: Pre-braze assembly for two articles: carbon fiber weave and Ticusil foil wired to a 3-inch Inconel tube

Ideally, the brazing process should be conducted in a large vacuum furnace. Since this was not available for this work, brazing trials were conducted in a bell jar vacuum chamber at MSFC, shown in Figure 3.16. The chamber had a 6-inch viewport so the braze melt can be monitored visually. The chamber could be evacuated to 10^{-7} torr and has no built-in heater elements. Two styles of heaters were designed for the various test articles. For test articles fabricated earlier in the study that had Inconel tubes in place of heat pipes, a cylindrical heater was fabricated with electrical resistance wire coiled around an alumina core. The test articles were then slid onto the heater and heated radially from the underlying heater wires. After a few trials, an IR lamp was added to provide extra heat to the external foil surfaces during brazing. Figure 3.17 shows the heater core, IR lamp, and supporting structure for the simulated heat pipe test articles.
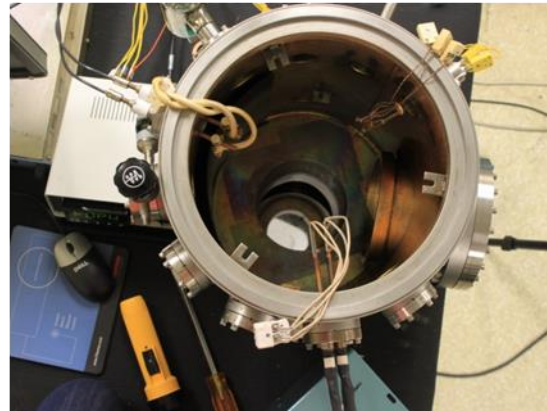
Figure 3.16: Bell jar vacuum chamber at MSFC used for brazing and testing

Figure 3.17: Heater assembly used for brazing (left): heater coil that supports and heats the sample, and an IR lamp above for added heat. With mounted sample (right).

For the test articles with working heat pipes, the heater consisted of a 2.5-inch, 300 W Thermcraft clamshell resistance heater that clamped onto the hot end of the heat pipe. Alumina housing was used to insulate the heater. The IR lamp was used for these samples too. Figure 3.18 shows the heat pipe heater assembly.
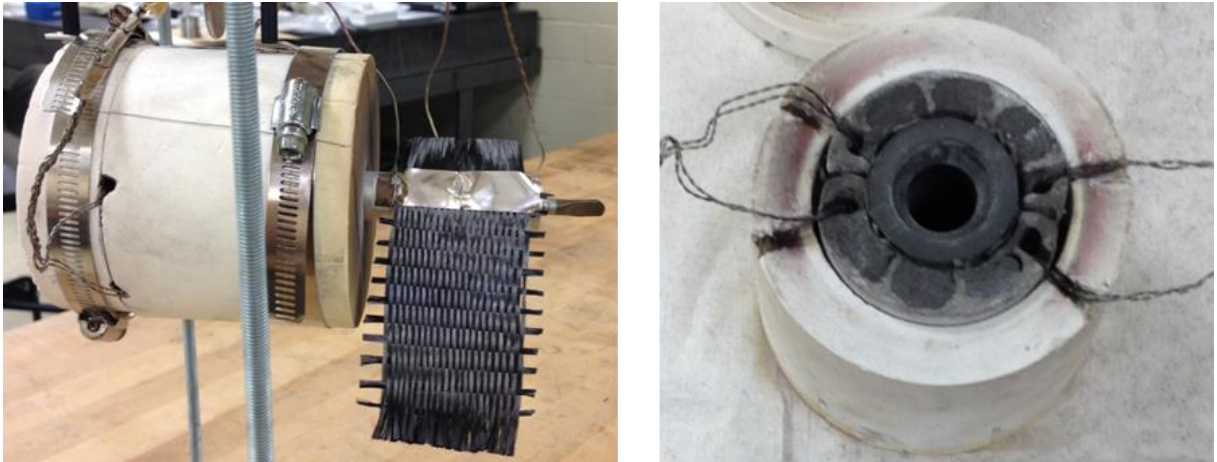
Figure 3.18: Heat pipe heater assembly with a test article (left), detail of clamshell heater and alumina housing (right)

Once the test article was assembled and mounted on the heater, the assembly was placed into the chamber and the chamber was evacuated. The test article was heated directly to 900-950°C and held until the top layer of braze melted. Once the foil melted completely, the heater was turned off and the system cooled naturally.

3.4.3 Brazing Results

Brazing trials were conducted on five test articles. The first three test articles consisted of Inconel tubes and hand-woven fins. Test article B had a fin woven using the first weaving method and TA-C and TA-D had fins woven with the second method. Test article E consisted of a heat pipe and a weave using the second method and TA-F had a heat pipe with a TEAM textile fin. The braze joints of TA-B, C and D are shown in Figure 3.19. Of the three, TA-B had the most successful braze. The sample was heated to nearly 950°C and the Ticusil foil completed melting within five minutes of the melt

97

initiation. When heating TA-C and D, more power was required to reach 950°C, which caused several

heater coils to fail due to current overload. This increase in power was attributed to the denser fins that

radiated much more power away from the braze joint. While this bodes well for the heat dissipating

abilities of the fibers, it proved detrimental to the brazing process. After the less-successful braze melt

with TA-C, several modifications were added to the heater assembly, attempting to increase the power

supplied to the braze joint. The IR lamp was added above the sample, and a stainless steel reflector was

added around the fin to reduce the direct radiation from the fin to the chamber walls, shown in Figure

3.20.
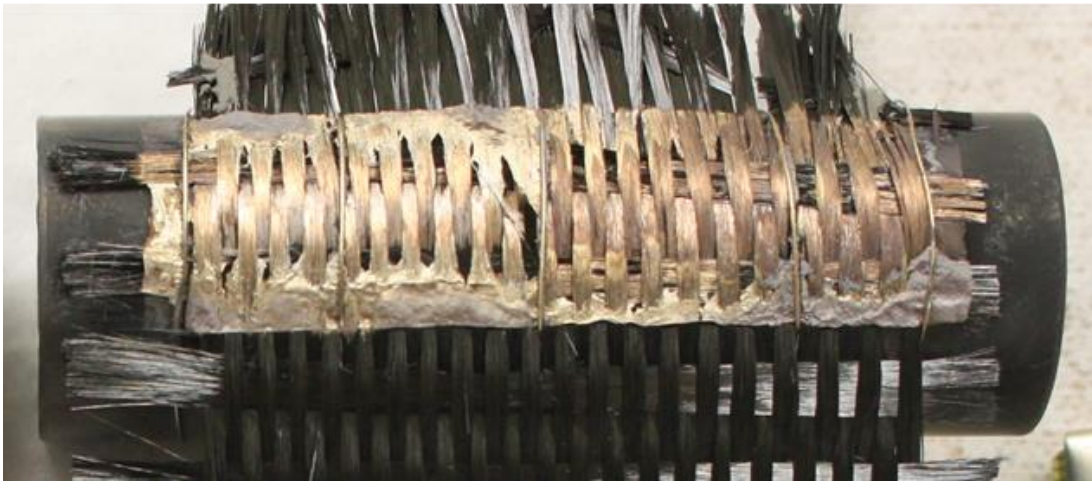
Figure 3.19: Braze joints on test articles B, C and D (top to bottom)

Figure 3.20: Stainless steel reflector added to the heating assembly for brazing

The heater modifications helped, but melting the top foil layer on TA-D required an extended

hold of about 20 minutes over 900°C, and was still not as complete as TA-B. In vacuum, the longer it

takes for the entire foil to melt, the more material volatizes. Condensed silver was detected on the

chamber walls after long braze trials. Thus, improvements should be made to decrease the melt time.

Improvements in a non-furnace vacuum chamber include minimizing radiative heat losses by adding

reflective shields or insulation around the sample, and adding more external heaters. This series of tests

demonstrated that the thicker the fin, the more important it is to use a proper brazing furnace so that

the sample melts uniformly and quickly.

None of the heat pipe test articles achieved a successful melt of the top foil. As with the heater

coil used in the simulated heat pipes, several of the clamshell heaters failed during braze attempts.

While the foil on TA-E did demonstrate signs of softening and melt initiated at several points under the

tie-wires, thorough melting could not be achieved, see Figure 3.21. Since the textile was thicker than

the hand-woven fins, it was clear that brazing TA-F would be even more challenging. Thus, only a

narrow fin was used and another block of insulating alumina was added to the free end of the heat pipe.

Again, softening of the top foil layer was observed while the bottom layer melted completely, see Figure

3.22.

Figure 3.21: Test article E consisting of a heat pipe with a hand-woven fin

Figure 3.22: Test article F consisting of a heat pipe with a textile fin

There was no way to add more power to the samples given the geometric constraints of the

chamber and standard clamshell heaters. Additionally, with the large clamshell heater assembly, the

chamber itself overheated before the braze melted because the heater block radiated excessive heat to the walls. Even with a cooling tube wrapped around the outside of the chamber, the wall temperature exceeding 150°C. The bell jar has a rubber gasket that should not be exposed to temperatures above 150°C. For these reasons, complete braze melting was not achieved.

Inert gas brazing is another alternative to the vacuum furnace with several advantages, including heat transfer by conduction that would promote uniform heating, and minimal filler vaporization due to the gas pressure. Argon, dry hydrogen, and helium are suitable for active braze alloys, however nitrogen and hydrogen should not be used for this application because nitrogen reacts with titanium to form a nitride, and hydrogen can combine with graphite [84]. A small study was conducted at UMass to test the feasibility of brazing carbon fibers to a stainless steel substrate using Ticusil in a pressurized argon atmosphere. Qualitative results indicated that the environment had no negative effects on the braze joint or fibers. No vaporized silver was observed on the walls of the brazing chamber, confirming that the pressurized environment inhibits filler metal vaporization.

Several attempts were made to build a sealed furnace large enough to fit a test article that could be pressurized with argon gas for brazing, but none were successful. Thus, the vacuum chamber remained the only option for this work.

3.4.3.1 Braze Joint Thermal Resistance

The order of magnitude of the thermal resistance of the braze joint relative to the fin was estimated in two ways: 1) modeling the thermal resistance of each layer in the joint, and 2) measuring the temperature drop between the Inconel tube and the top layer of the brazed fiber during a test. First the thermal resistance was modeled using estimated thermal conductivity and thickness values for the titanium carbide and copper-silver layers. The thermal conductivity of titanium carbide is about 5.64 W/m-K at room temperatrue and 30.93 W/m-K at 1000°C [85]. Silver and copper have thermal

conductivities near 400 W/m-K in their pure forms, however as an alloy, the Ag-Cu thermal conductivity tends to be reduced due to electron and phonon scattering in the lattice structure. The thermal conductivity of Ticusil, given in Table 3.3, is 219 W/m-K, which is assumed to be slightly lower than that of an Ag-Cu alloy due to the small percentage of Ti. For this calculation the thermal conductivities of the Cu-Ag and TiC layers are assumed to be 250 W/m-K and 20 W/m-K respectively. The thicknesses of the layers are assumed to be 101.6 μm for the Ag-Cu (the thickness of 2 foil layers), and 0.3 μm for the TiC (from the SEM examination). For a joint area of 2 by 5 cm and 100 W of power delivered to the joint during test article operation, the temperature drop across the joint is less than 50 milli-Kelvin, which is insignificant compared with the thermal resistances of the Inconel tube wall or the fin.

The second evaluation of the thermal resistance of the braze joint involved measuring the temperature difference between thermocouples placed on the Inconel pipe and on the exterior of the brazed fibers during a test. Figure 3.23 shows the test article with the two reference thermocouples, placed close together to minimize heat pipe temperature variations. A temperature difference of about 20 K was measured between the two thermocouples at an operating temperature of 600 K. Similar measurements were made using a heat pipe test article. This difference could be explained by the low transverse thermal conductivity of the fibers and the less than optimum penetration of the melted braze into the fiber weave. This temperature drop should represent an upper bound. It is expected that the thermal resistance of the joint can be reduced with more advanced brazing techniques. The temperature drop along the fibers is on the order of several hundred degrees, and since the temperature drop across the braze is on the order of 20 K, a detailed property measurement of the joint was not justified for this work.
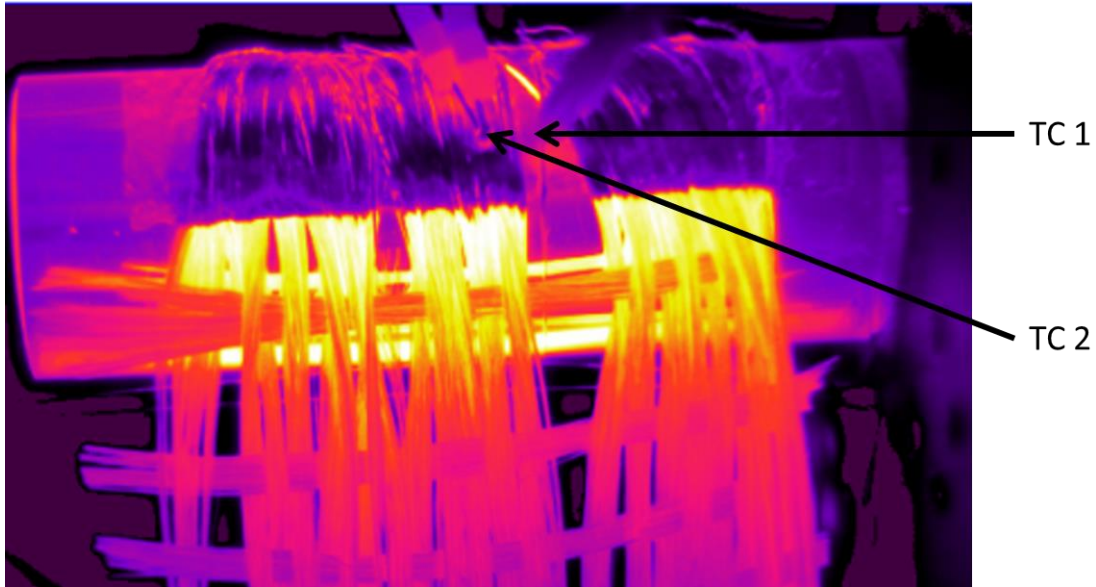
Figure 3.23: IR image of test article B with thermocouples 1 and 2

3.4.3.2 SEM and Thermodynamic Analysis

A Ticusil-brazed carbon fiber sample was analyzed using scanning electron microscopy (SEM) and energy dispersive spectroscopy (EDS) to determine the composition and microstructure of the interphase layer near the fibers and the bulk of the braze. The results of the analysis show a clear layer of titanium carbide roughly 0.3 µm thick around the perimeter of each fiber as shown in Figure 3.24. Figures 3.25 through 3.27 are the EDS results from the locations indicated on Figure 3.24. In the temperature range of 920-1050°C the Gibbs free energy change for the reaction Ti+C→TiC is −(174 to 169) kJ/mol so the formation of Ti-C is thermodynamically favorable [80]. This carbide layer is expected to serve as a diffusion barrier to titanium, preventing further carbide formation, but only a life test at the operating temperature could establish this definitively. Figure 3.28 is the phase diagram for titanium and carbon showing that at most compositions titanium will react with carbon to form a carbide. Figures 3.29 and 3.30 are the copper-carbon and silver-carbon phase diagrams showing that those metals do not react with carbon, explaining why titanium is necessary for the braze to adhere to carbon fiber. These phase diagrams were generated at NASA GRC using FactSage.

The silver and copper components of the braze remained as a two-phase bulk material surrounding the fibers. Figure 3.31 is the binary alloy phase diagram for silver-copper, showing that at the mole fractions present in Ticusil, two phases are expected to form. Figure 3.32 shows an SEM image of the end of a Ticusil-brazed carbon fiber tow and Figure 3.33 shows the EDS results of the location indicated as "EDS-A" in Figure 3.32, confirming again that most of the titanium migrates to the carbon surface during the braze process leaving no detectable concentration at the braze surface.
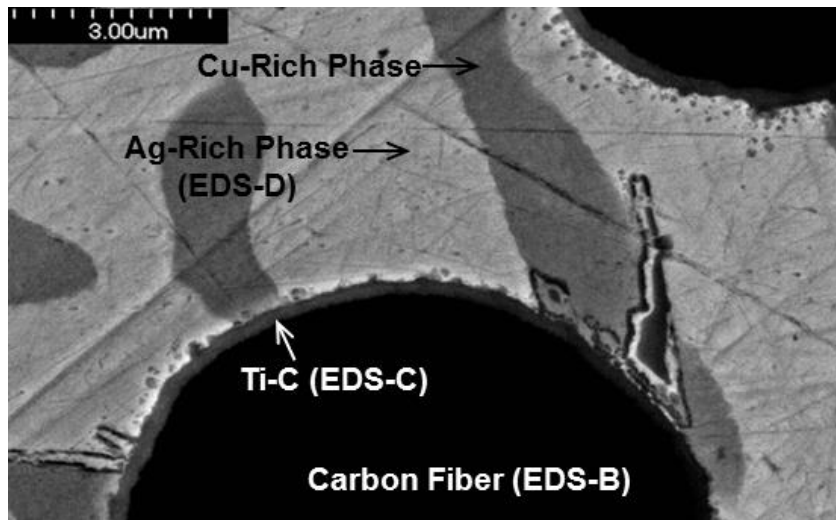
Figure 3.24: SEM image of a Ticusil-brazed carbon fiber sample
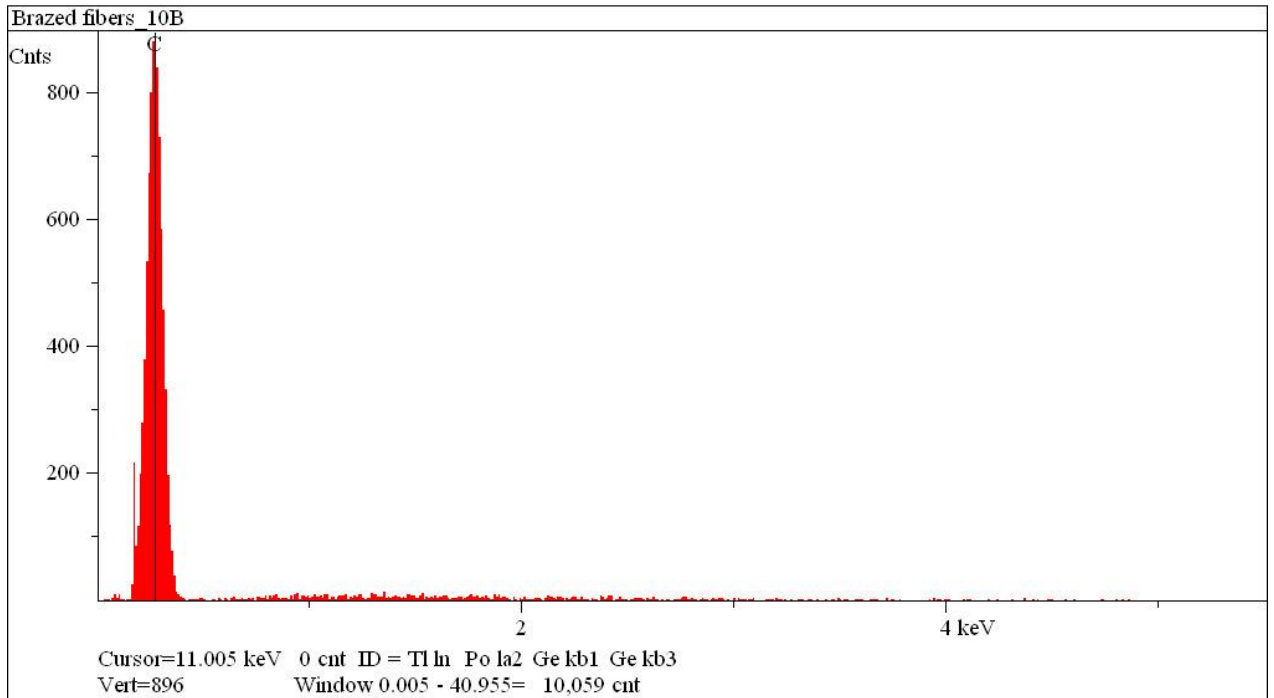
Figure 3.25: EDS results from EDS location B in Figure 3.24 showing the pure carbon composition of the fiber
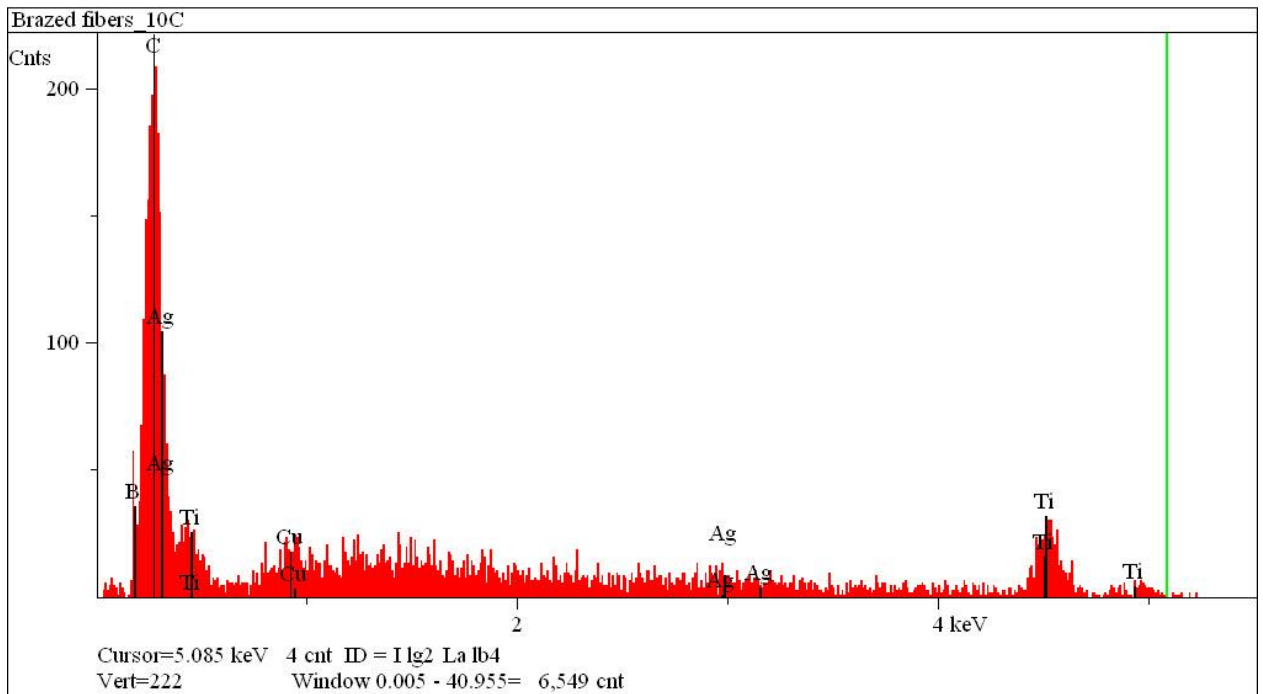
Figure 3.26: EDS results from EDS location C in Figure 3.24 showing the titanium and carbon composition of the layer around the fiber
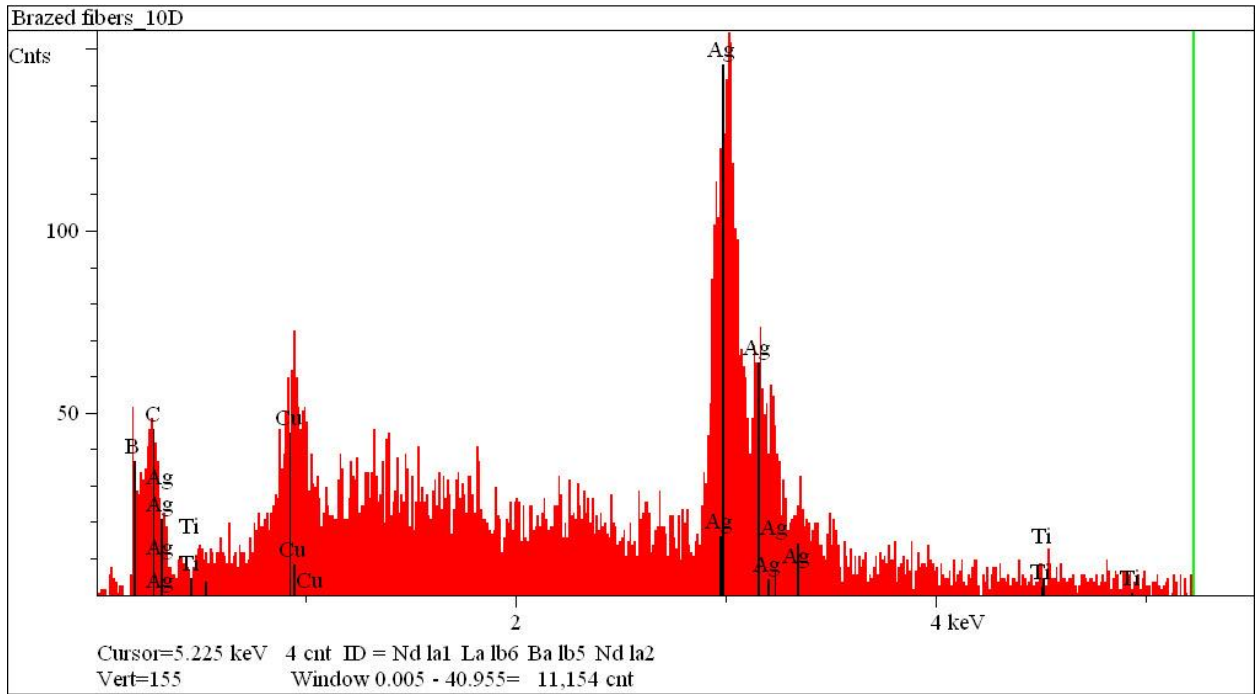
Figure 3.27: EDS results from EDS location D in Figure 3.24 showing the high silver content in that phase of the bulk braze material
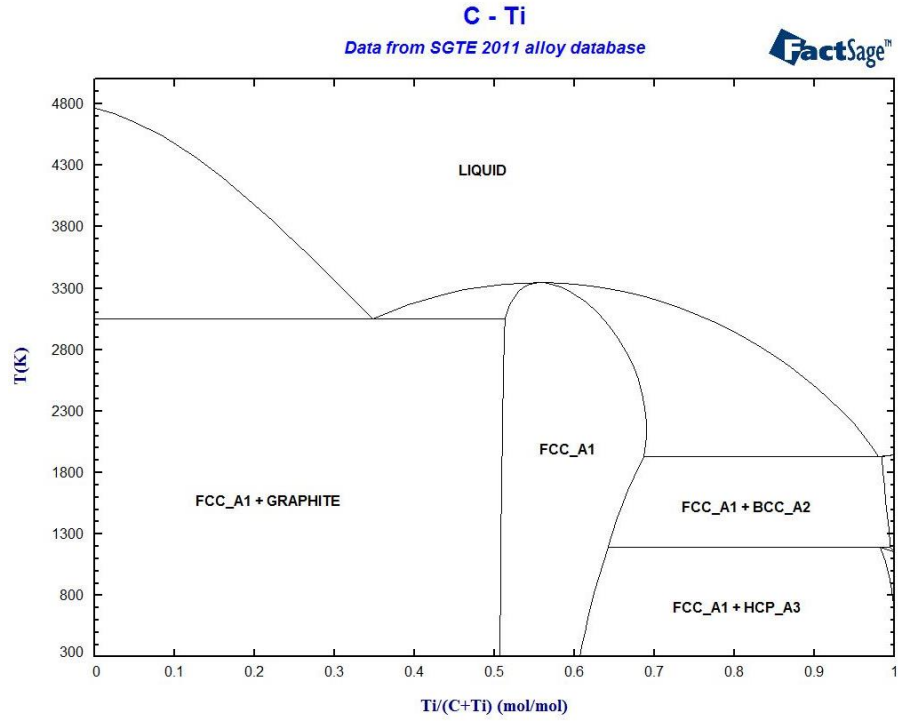
Figure 3.28: Titanium-carbon phase diagram
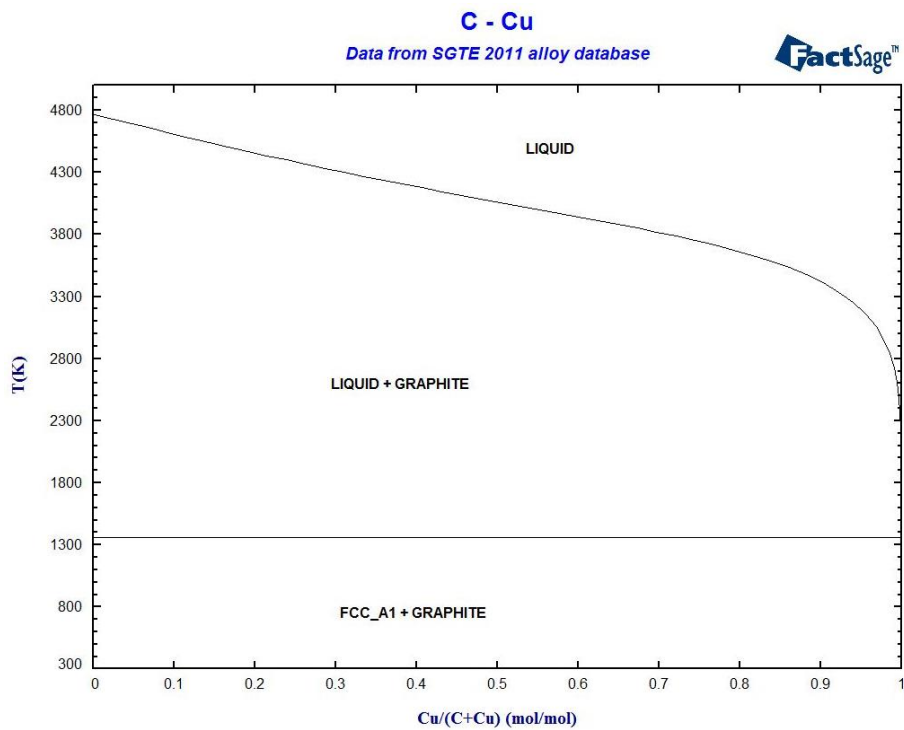
Figure 3.29: Copper-carbon phase diagram

Ag - C

Data from SGTE 2011 alloy database

FactSage™

LIQUID

LIQUID + GRAPHITE

GRAPHITE + FCC_A1

C/(Ag+C) (mol/mol)

T(K)
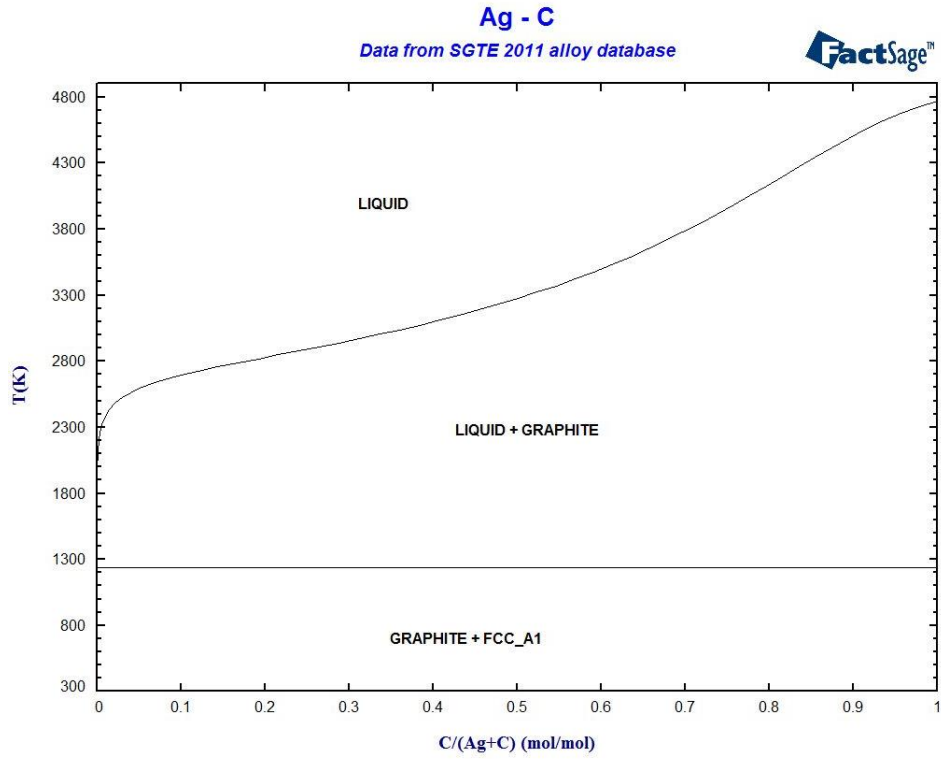
Figure 3.30: Silver-carbon phase diagram

Cu - Ag

Data from FScopp alloy databases (2012)

FactSage

LIQUID

FCC_A1

FCC_A1

FCC_A1 + FCC_A1#2

mole Ag/(Cu+Ag)

T(C)
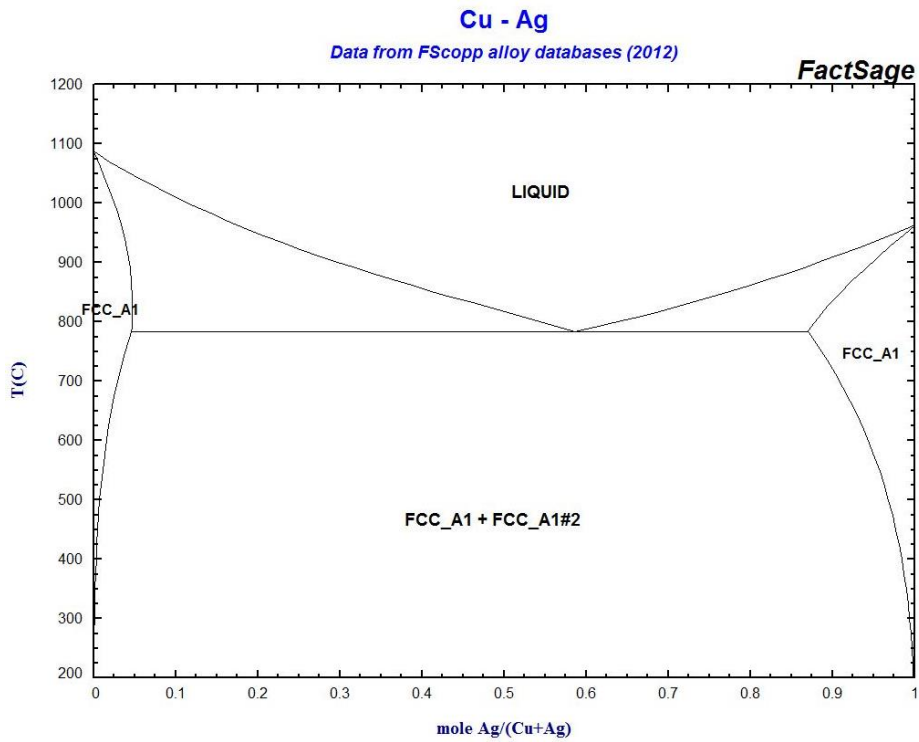
Figure 3.31: Silver-copper phase diagram

109
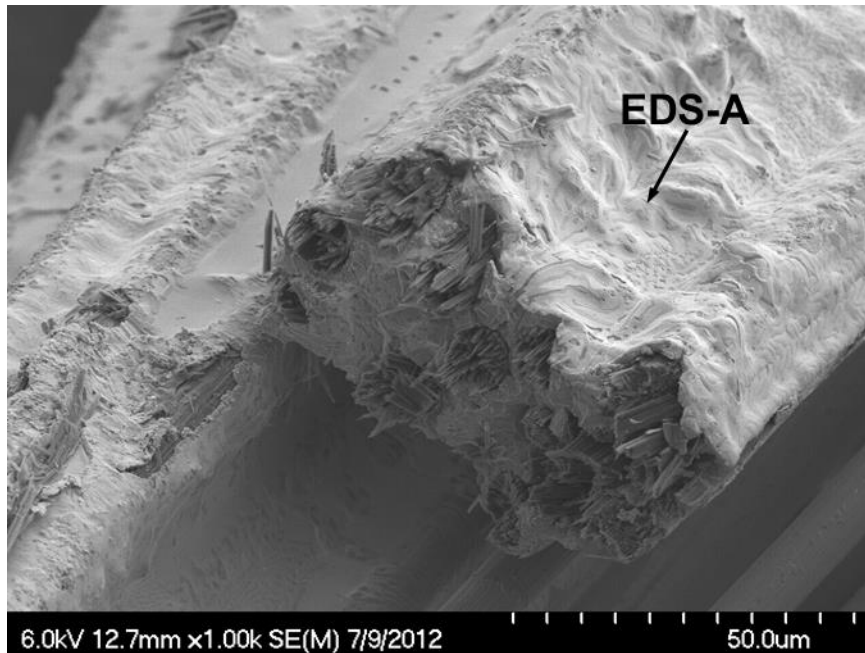
Figure 3.32: SEM image of the end of a Ticusil-brazed carbon fiber tow and the location of EDS-A
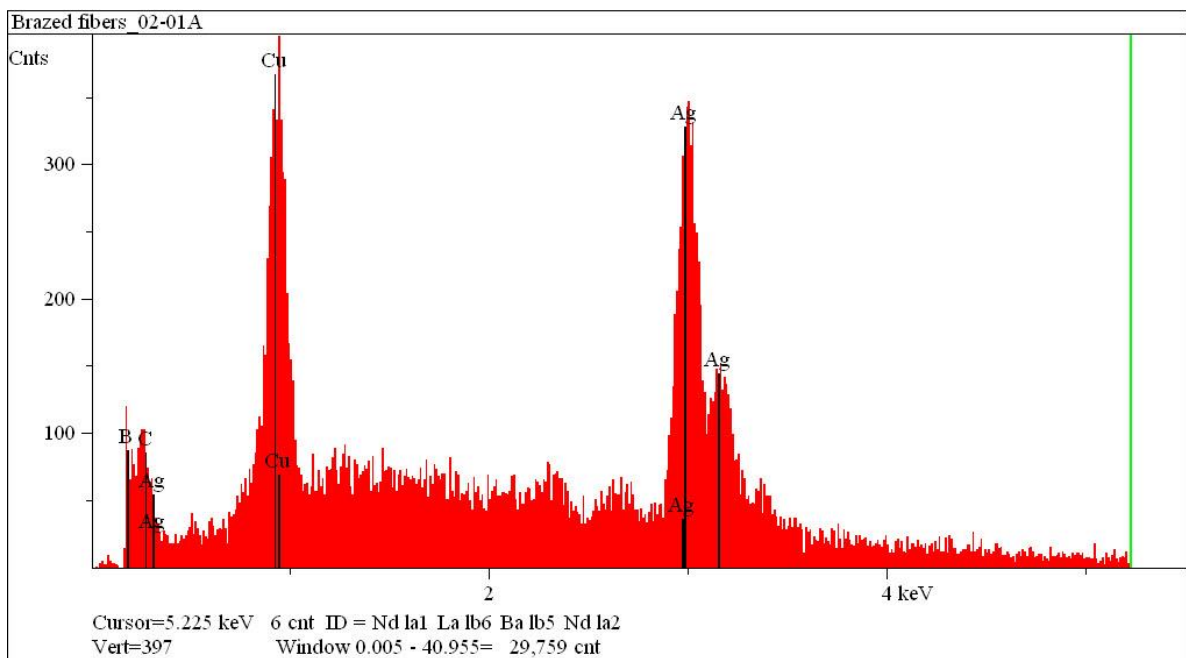
Figure 3.33: EDS results from the location in Figure 3.32 indicated as EDS-A showing large concentrations of copper and silver

3.5   Heat Pipes

The heat pipe is the last major component of the test article assembly. For the first generation

test articles, heat pipes were not available, so simulated heat pipes were built using 1-inch diameter

Inconel tubes mounted on the aforementioned 3-inch heater core. The heater was a Kanthol K1

resistance heating wire coiled around an alumina core. As shown in Figure 3.34, the core structure was

wider at the supported end. More heat conducted to, and radiated from, this exposed alumina than

from the opposite side of the support, which caused an asymmetry along the Inconel tube shown in the

IR image and accompanying temperature profile, Figure 3.35.
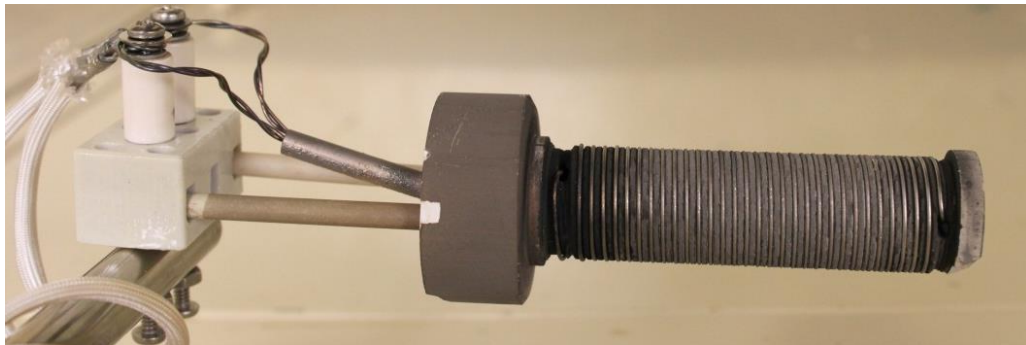
Figure 3.34: Electrical resistance heater used to heat the Inconel pipe test articles
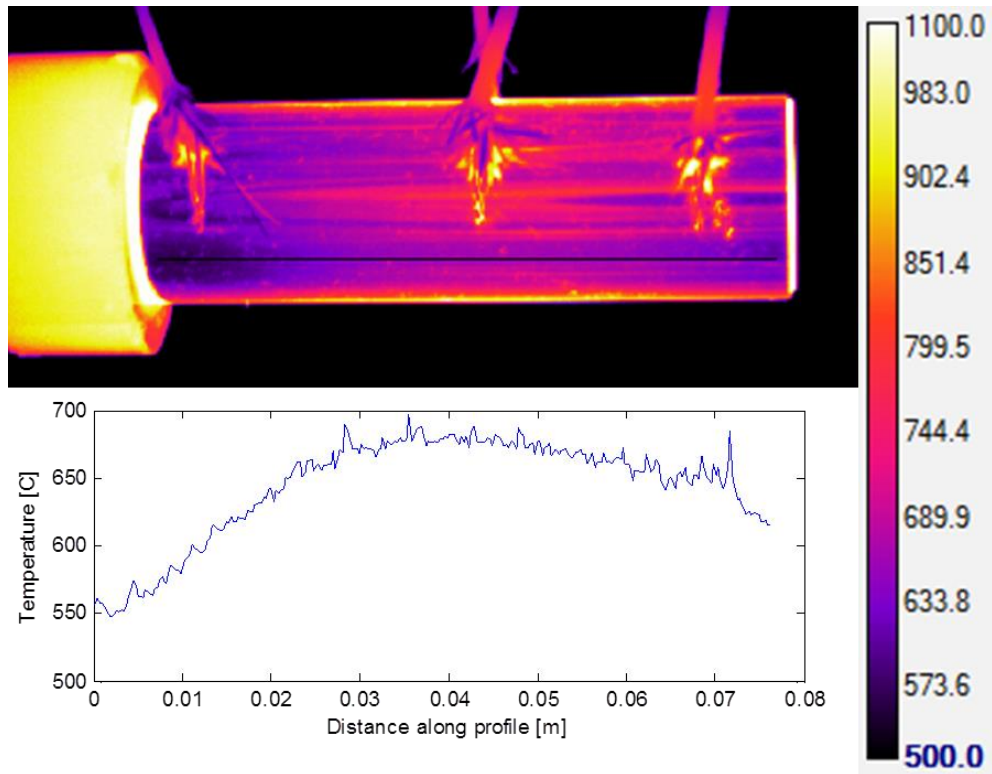
Figure 3.35: Top: IR image (in°C) of a bare Inconel tube on the heater with four thermocouples. The emissivity was set to that of the Inconel tube, ε=0.16. Bottom: Temperature profile along tube corresponding with the IR image. Noise in the profile is due to surface reflections and variation in emissivity due to surface preparation.

After test articles B, C and D were fabricated using Inconel tubes, the next step in increasing the fidelity of the test articles was to use real heat pipes. Custom, small-order sodium heat pipes are available from two heat pipe manufacturers, Thermacore and Advanced Cooling Technologies, but the estimates ranged from $6,000-$9,000 per pipe which was out of range for the project budget. James Sanzi, a heat pipe expert at NASA GRC, was able to fabricate custom pipes for this work and fabricated three sodium heat pipes. The shell material was Inconel 600 with a wall thickness of 0.062-inches. The interior was lined with stainless steel mesh wick and filled 5% by volume with high purity sodium working fluid. The pipes are approximately 6-inches long with an outer diameter of 0.75-inches, and designed to allow for a 3-inch evaporator and a 3-inch condenser onto which the fin could be brazed. Figure 3.36 shows a finished heat pipe.

Figure 3.36: Six-inch long sodium heat pipe fabricated at NASA GRC

As previously described, the heat pipe evaporator was heated by a clamshell heater. Heat pipe

initiation occurs at about 500°C, when the sodium melts fully and the vapor pressure is sufficient for

significant heat transfer. The upper limit on the heat pipe operating temperature is around 1200°C,

when the wick dries out as too much of the sodium enters the vapor phase. Unlike the simulated heat

pipes, the real heat pipes were isothermal along the condenser to within a degree at steady state.

Figure 3.37 is an image of a heat pipe operating at steady state. Figure 3.38 is an IR image of the same

working heat pipe and a temperature profile along the pipe axis. Reflections from the pipe account for

most of the variation in the temperature profile. The two thermocouples in the image were reading

within a degree of each other at 571°C, verifying that it functioned as designed. The ability of heat pipes

to transfer heat over long distances efficiently and passively makes them very desirable for space

applications.
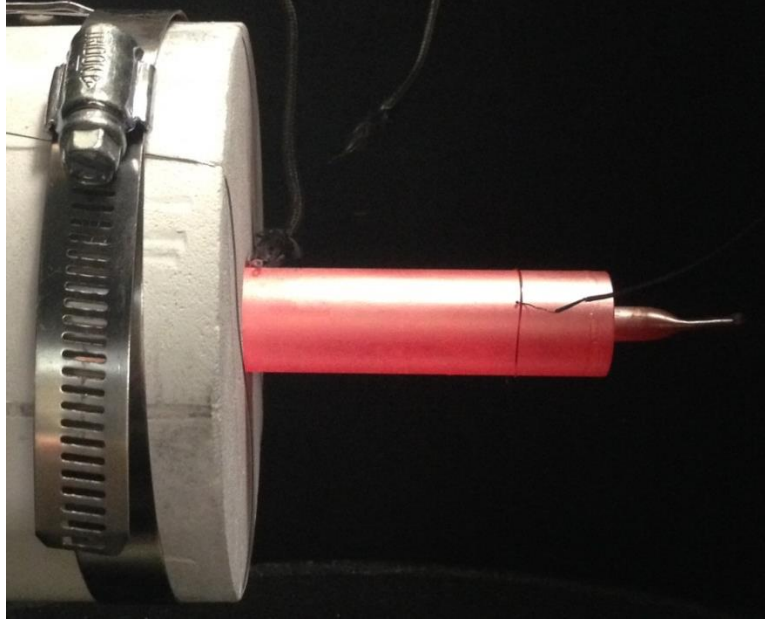
Figure 3.37: Image of a sodium heat pipe operating at 571°C
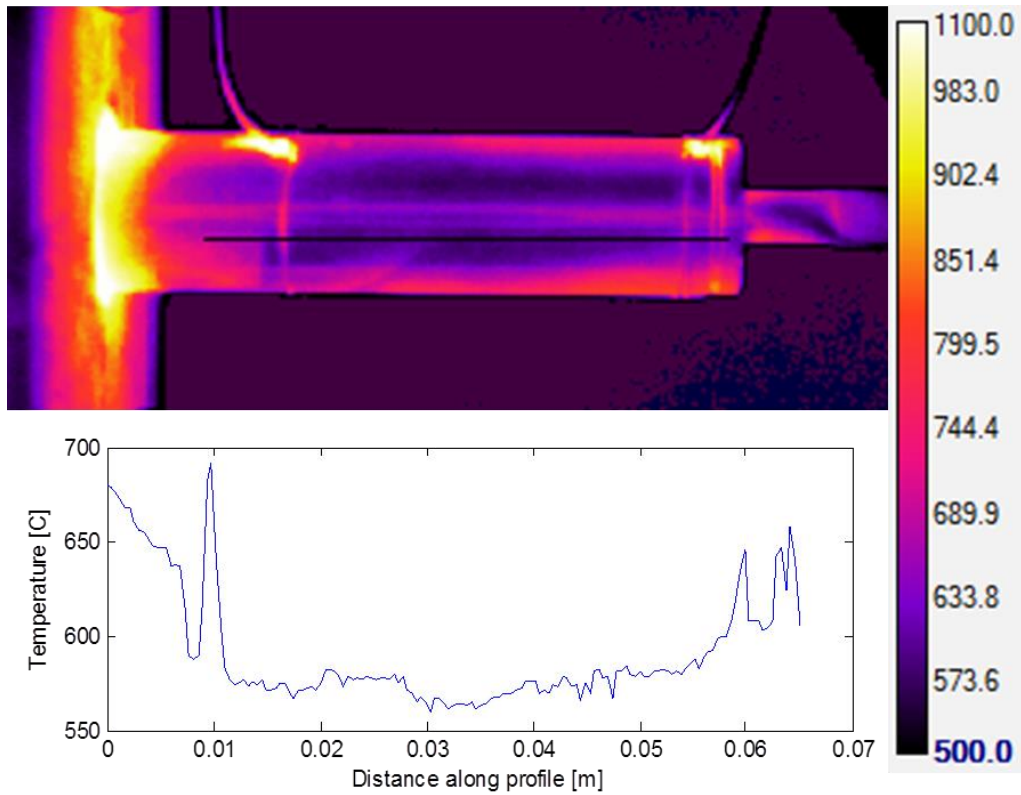
Figure 3.38: Top: IR image (in°C) of sodium heat pipe with two thermocouples reading 571°C. The emissivity was set to that of the pipe, ε=0.19. Bottom: Temperature profile along pipe corresponding with the IR image. Noise in the profile is due to the thermocouple wire, surface reflections and variation in emissivity due to surface preparation.

3.6   Conclusion

In summary, the work described in this chapter increased the technology readiness level (TRL) of the concept from a 2, basic understanding of the principles of the technology, to a 4, component validation in the laboratory environment. To accomplish this, the fin, attachment method and heat pipe were all designed and tested. Mass-production of a high quality, high thermal conductivity K13D2U fiber textile was proven to be feasible. Brazing with Ticusil was selected as the joining method since it is chemically compatible with carbon fibers and a variety of heat pipe materials, provides a good thermal conduction path between the fibers and pipe, and is suitable for extended use at 600°C. Methods and recommendations for how to effectively braze the fin to the pipe were presented. This work demonstrated that higher-fidelity fin-heat pipe test articles could be fabricated.

This concludes the discussion on test article design fabrication. In the next chapter, properties and performance of the test articles are evaluated.

CHAPTER 4

NON-CONTACT THERMAL PROPERTY MEASUREMENT AND HEAT REJECTION PERFORMANCE TESTS

4.1   Introduction

A principal goal of this work is to demonstrate and quantify the heat rejection capabilities of a carbon-fiber-heat-pipe radiator. Models predict that carbon fiber fins should out-perform carbon-carbon composite fins in terms of specific power (kW/kg), however this assertion has never been tested. Experiments were designed to measure the power rejection of the carbon fiber fins using infrared imaging. Measurements of the power rejection from the fin are used to calculate the specific power rejection, a metric for comparing the carbon fiber with other high-temperature fin materials. Additionally, literature on the thermal conductivity of pitch carbon fibers at elevated temperatures in bulk form is very limited, so experimental results were employed to estimate the thermal conductivity of the carbon fiber fins. The thermal conductivity estimate adds fidelity and predictive capabilities of the fin models. The methods of measuring the fin surface temperature and thermal properties are presented here.

4.2   Non-Contact Temperature Measurement

Non-contact temperature measurements of the fins during tests were acquired using a FLIR infrared (IR) camera (Model A655 sc) and the accompanying data processing software called ExaminIR. The camera senses infrared radiation in the range of 7.5-14 µm and thus must be used in combination with a vacuum chamber window transmitting those wavelengths. A zinc selenide vacuum window with an anti-reflection coating was employed, which transmits around 98% of the radiation in the camera's sensitive waveband as shown in Figure 4.1 The transmission decreases slightly between 12 and 14 µm, however this is considered insignificant since tests were conducted at elevated temperatures where the majority of thermal radiation is emitted at shorter wavelengths. A standard quartz glass window

absorbs a large fraction of the infrared radiation, so the camera requires this specialized window. The

camera and zinc selenide window mounted on the vacuum test chamber are shown in Figure 4.2.
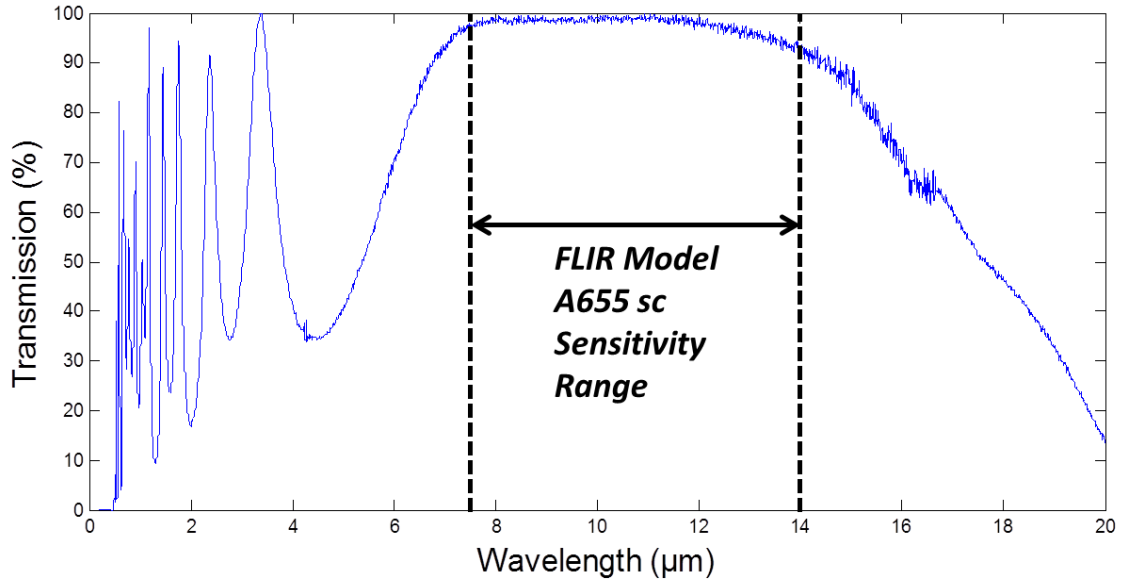
Figure 4.1: Zinc selenide window transmission curve (5 mm thick with AR coating) [86]
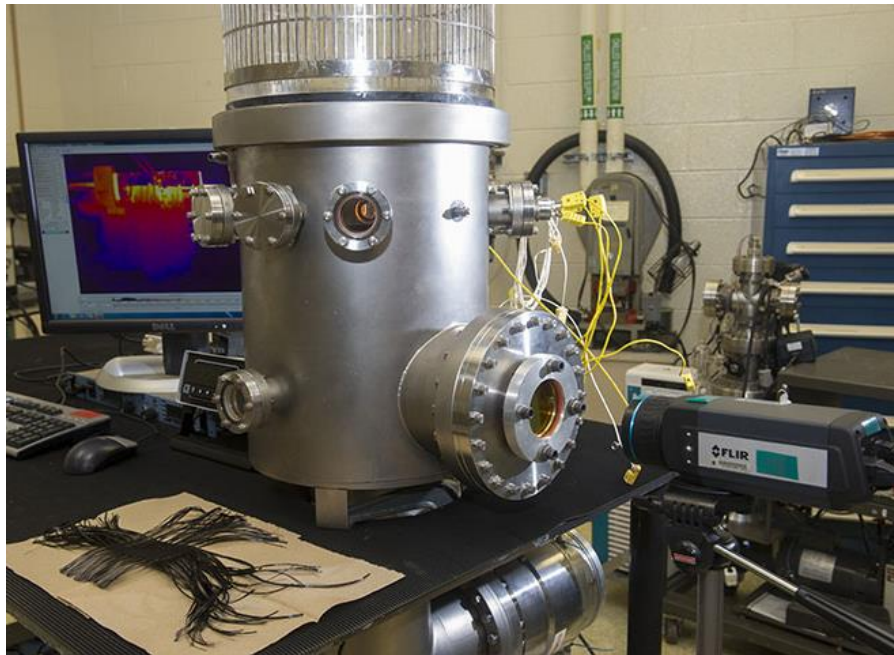
Figure 4.2: FLIR IR camera aimed at the zinc selenide window on the vacuum test chamber

The IR camera has an array of sensors (i.e., pixels) that measure the intensity of the radiation. At each pixel the single intensity is an integrated value over all of the wavelengths in the camera's range. The IR camera is similar to a typical digital camera except for it senses radiation in the infrared band instead of red, green and blue. The ExaminIR software uses the intensity at each pixel and combined with the camera's settings (i.e., focal length, user-supplied effective spectral emissivity, window transmission, reflected temperature), calculates a single temperature per pixel. To measure accurate temperatures, appropriate emissivity and window transmission values must be defined in ExaminIR. The algorithm cannot correct for unwanted reflections, so if the viewed object is not a diffuse reflector, care must be taken to minimize reflections in the enclosure (this is the case for viewing the bare heat pipe and the braze surface). Fortunately, the carbon fiber weave is a diffuse surface, so as long as the emissivity of the weave surface is known, the temperature measured by the IR camera can be considered accurate. The temperatures in the entire field of view can be exported for further analysis.

4.3   Emissivity Measurement

The literature contains scarce information on the emissivity of bulk carbon fiber, mostly because using carbon fiber as a radiative component is quite rare. The emissivity of a sample of the carbon fiber weave was measured at the NASA Glenn Research Center with the help of Dr. Don Jaworske using a Surface Optics Corporation reflectometer, model SOC-400T. This device uses an FTIR Michelson-type interferometer to measure the spectral reflectance of an opaque material over the wave band 2-25 μm [71]. The room-temperature sample is illuminated with near-normal beams and the reflected energy is detected hemispherically.   The spectral reflectance response gives the spectral absorptivity since the reflected and absorbed energy sum to unity (i.e., $1 - \rho_\lambda = \alpha_\lambda$ when $t_\lambda = 0$). The spectral emissivity is obtained through Kirchoff's Law (i.e., $\alpha_\lambda = \varepsilon_\lambda$ at thermal equilibrium). The total hemispherical emissivity is then calculated at any desired temperature using Equation 4-1 assuming the spectral emissivity is temperature independent, a typical assumption up to about 1200°C.

$$\boldsymbol{\varepsilon(T_i)} = \frac{\int_0^\infty \varepsilon_\lambda(\lambda) e_{\lambda b}(\lambda, T_i) d\lambda}{\sigma T_i^4} \qquad\qquad (\,4\text{-}1)$$

Figure 4.3 gives the results from the reflectance versus wavelength measurement for a sample of the carbon fiber weave as well as gold and black calibration standards that are nearly perfect reflectors and absorbers respectively in this waveband. The spectral reflectivity profile of the carbon fiber weave increases slightly with wavelength from about 0.15 at 2.5 μm to 0.35 at 25 μm. While these results indicate that the carbon fiber weave is not perfectly gray, the majority of thermal radiation emitted from hot surfaces (>300°C) is below 10 μm, so the rise in reflectivity with higher wavelengths has little effect on the integrated total hemispherical emissivity values.
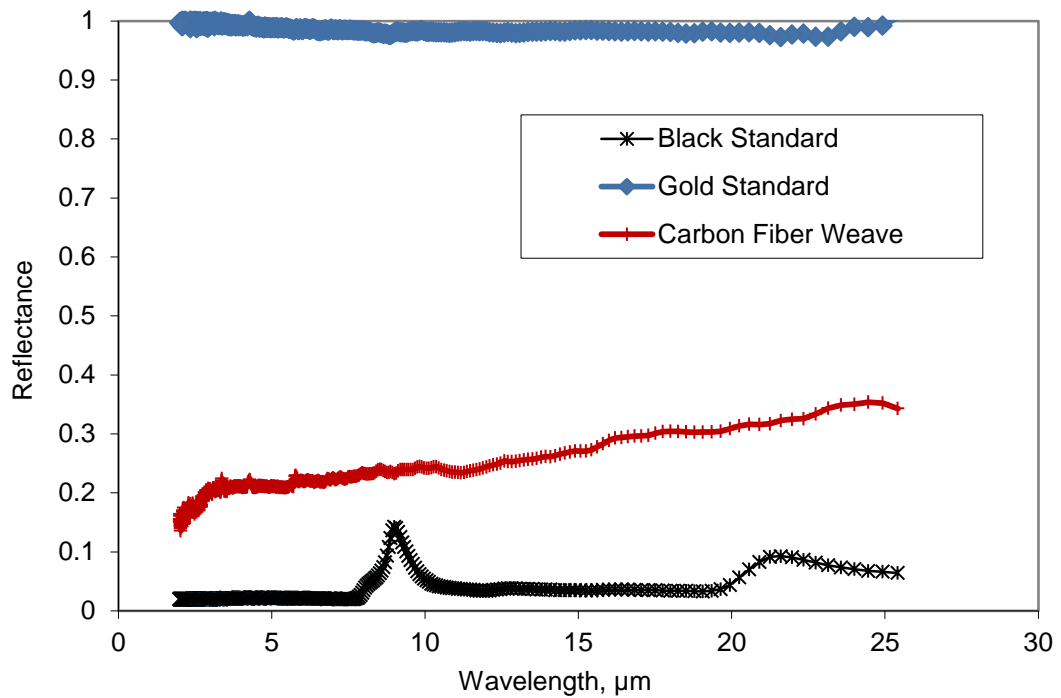
Figure 4.3: Reflectance versus wavelength for a black standard, a gold standard, and a carbon fiber weave sample measured at NASA GRC using a SOC-400T reflectometer

Using the spectral reflectance data and Equation 4-1, the total hemispherical emissivity versus temperature was calculated; Figure 4.4 shows the results. The emissivity increases with temperature because the peak in the blackbody curve moves to lower wavelengths with temperature and the spectral emissivity of the fibers is higher at lower wavelengths. The total hemispherical emissivity ranges from about 0.74 at room temperature to 0.78 at 900 K to nearly 0.8 at 1300 K, within the normal range for graphitic materials.
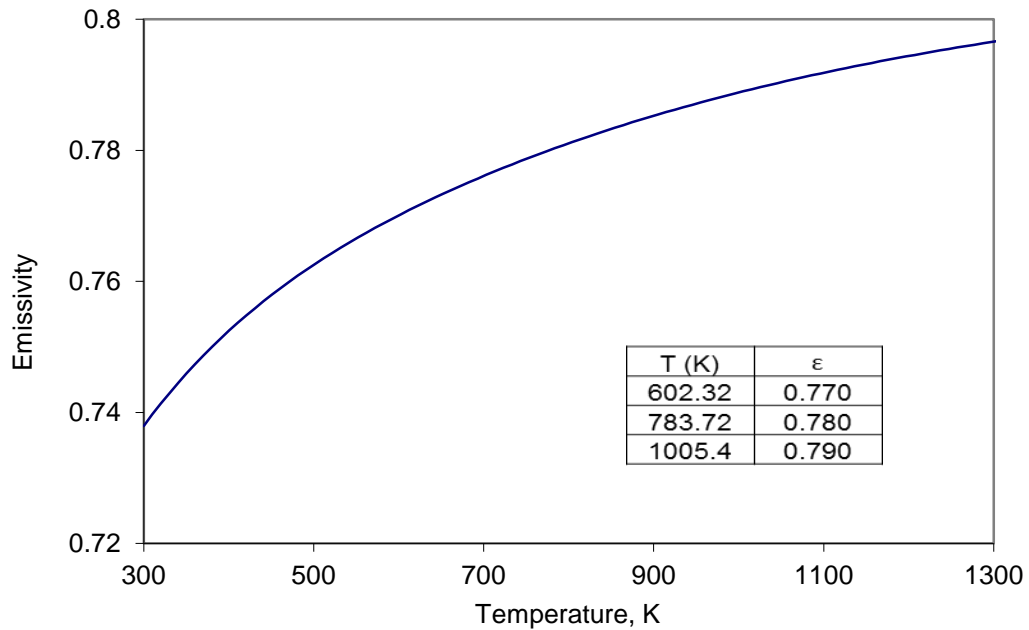
Figure 4.4: Calculated total hemispherical emissivity versus surface temperature for the carbon fiber weave sample

A well-designed radiator fin should exhibit a temperature variation no more than 300 K along the fiber axis, so a fin whose surface temperature ranges from 600 to 900 K would expect to experience a change in the total hemispherical emissivity of less than 2%. This justifies assuming no temperature dependence of emissivity for this work.

With a good estimate of the total hemispherical emissivity of the fiber weave, temperature data from the IR images can be used with confidence. Fin surface temperature data can be used to determine the specific heat rejection and axial thermal conductivity of the fin.

4.4   Indirect Measurement of the Fin Axial Thermal Conductivity

Axial thermal conductivity is the second thermal property important to the fin design. It has been shown that the thermal conductivity of lower-modulus pitch carbon fibers (Amoco P-100) has a maximum near 300 K and decreases slowly with higher temperatures as a result of Umklapp phonon scattering [87][88]. Umklapp scattering is a process by which thermal conductivity is reduced in

121

crystalline materials when phonons interact with surfaces or lattice defects. Pradere *et. al.* showed that the thermal conductivity of P-100 fibers decreases from about 190 to 170 W/m-K as the temperature increases from about 750 to 1500 K [88]. The thermal conductivity of higher-modulus pitch fibers at high temperatures is not available in the literature, but it is likely that Umklapp scattering will also cause the thermal conductivity to decrease slightly with temperature. Thus, it is expected that the thermal conductivity of the K13D2U fibers used in this work will be slightly lower than 800 W/m-K at elevated temperatures.

Much of the literature on carbon fiber thermal conductivity provides measurements using a single fiber. One study that measured the bulk thermal conductivity of pitch carbon fibers at room temperature found that the conductivity was consistently lower than that of the single fiber measurements [41]. Since bulk carbon fiber contains void space, measuring the bulk conductivity was found to be quite challenging. The standard guarded plate method for measuring thermal conductivity that steadily heats one end of a sample and measures the change in temperature across the sample is difficult with fibers without solid, flat surfaces. That is why single fiber measurements are often preferred. While the manufacturer states that the single-fiber axial thermal conductivity at room temperature is 800 W/m-K, estimating this property using the fiber weave at higher temperatures was of interest.

4.4.1   Method

The method developed here to estimate the fin axial thermal conductivity combines IR surface temperature data and finite element models. First, a fin test article is tested at about 600°C and IR data are collected. Next, fin surface temperature data extracted from the image is compared with results generated by a fin finite element model (as described in Section 3.2) where axial thermal conductivity is

the only free model parameter. A Matlab optimization code is used to find the thermal conductivity

value in the model that minimizes the error between the IR data and the thermal model.

The model assumes temperature-independent thermal properties, zero void fraction in the fiber

weave, and simple radiation boundary conditions. For this first order property estimation, assuming

temperature independent properties is consistent with available data. The fin temperature varies from

about 900K to 600K, which could have a slight impact on thermal conductivity as demonstrated by

Parede, who showed less than a 5% change in thermal conductivity between 600 and 900 K [88]. The

surface emissivity is assumed to be 0.78±0.01 based on the emissivity measurements from NASA GRC

presented in Section 4.3. The effective fin thickness (i.e., the thickness of a dense, flat sheet of the same

mass, with no void space between fibers) was determined to be 0.1374±0.0034 mm. This was

determined by measuring the width of fiber tows in the weave and calculating the effective thickness

using the known tow density and linear density (kg/m-tow).

The radiation boundary conditions are the collection of parameters with the greatest

uncertainty. These boundary conditions include the temperatures and emissivities of the heat pipe,

heater support structure, chamber walls and windows. The model includes radiation heat transfer

between the heat pipe and fin. Because of the large ratio of areas, the rest of the enclosure is idealized

as a black, isothermal enclosure. The heat pipe temperature was measured during the tests using a

thermocouple, and the emissivity is taken as 0.15, typical of unoxidized nickel at elevated temperatures.

The environmental temperature was based on several measurements of the chamber wall.

The optimization code was written in Matlab and is run in Comsol LiveLink with Matlab. The

code uses the Matlab function *fminunc*, which is a gradient-based search algorithm for unconstrained

optimization problems. Using a user-defined initial value for the axial thermal conductivity (k_x), the

function searches for the value of k_x that minimizes the mean squared error (MSE) between the IR and

model-generated data sets. Within the optimization program, the following steps are performed to

calculate the MSE value:

(1) Read the IR temperature data from an excel file

(2) Call the Comsol model file and send it the current k_x value.

(3) Run the Comsol model

(4) Return model results in an array of the fin surface temperature at every point along the

fin

(5) Fit the model results to a fourth-order polynomial (R^2 =1.00) to get a continuous

T_model(x) function

(6) Evaluate T_model(x) at every x-point in the real data set.

(7) Calculate MSE between the model set and the real data set:

$MSE = \frac{1}{n}\sum_{i=1}^{n}(T_{model}(i) - T_{IR}(i))^2$, where n is the number of IR data points.

The function iterates k_x until the change in the function value between successive iterations is

less than 10^{-10}. The optimization code was verified by plotting the MSE versus k_x, as shown in Figure 4.5.

This confirms that the MSE dependence on k_x is monotonic and that the algorithm found the true

minimum.
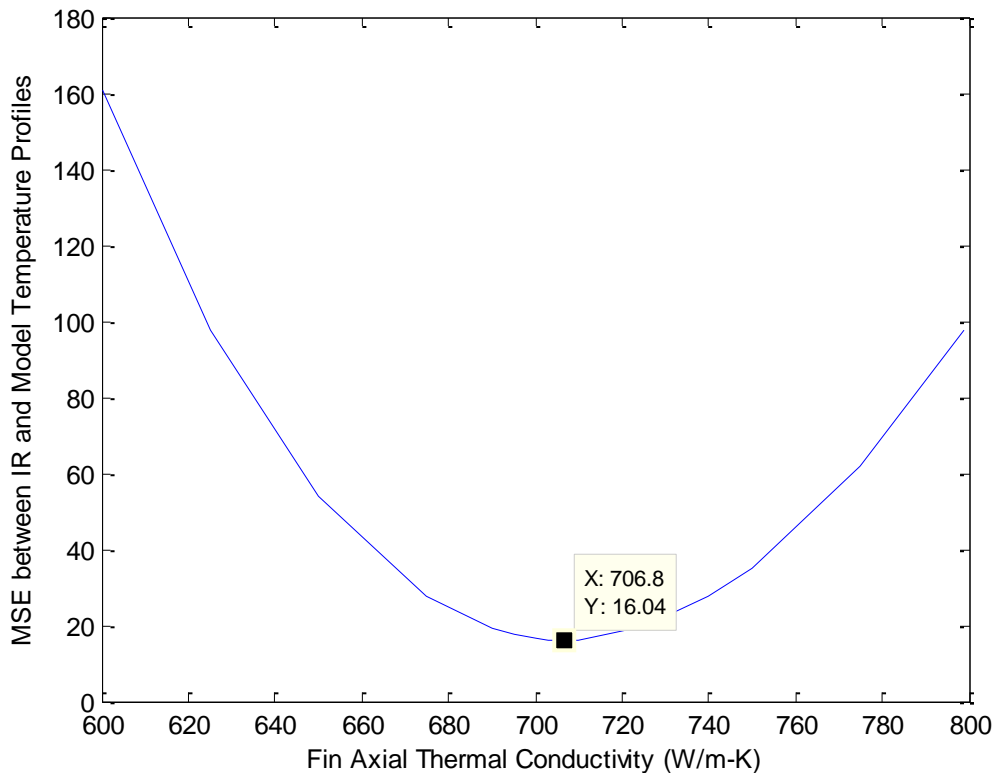
Figure 4.5: Mean square error versus fin axial thermal conductivity for the optimization case using test article E, showing monotonic behavior

4.4.2   Results

The first step in this analysis was to collect IR data from a test of one of the test articles. Test article E (TA-E) was employed because the fiber weave is highly uniform, which reduces the uncertainty in the effective thickness. Figure 4.6 shows the IR image from the performance test of TA-E. The green box shows the region from which temperature data was extracted. The temperatures were averaged across the width of the region to capture the average trends. The profile of average temperatures was used in the optimization.
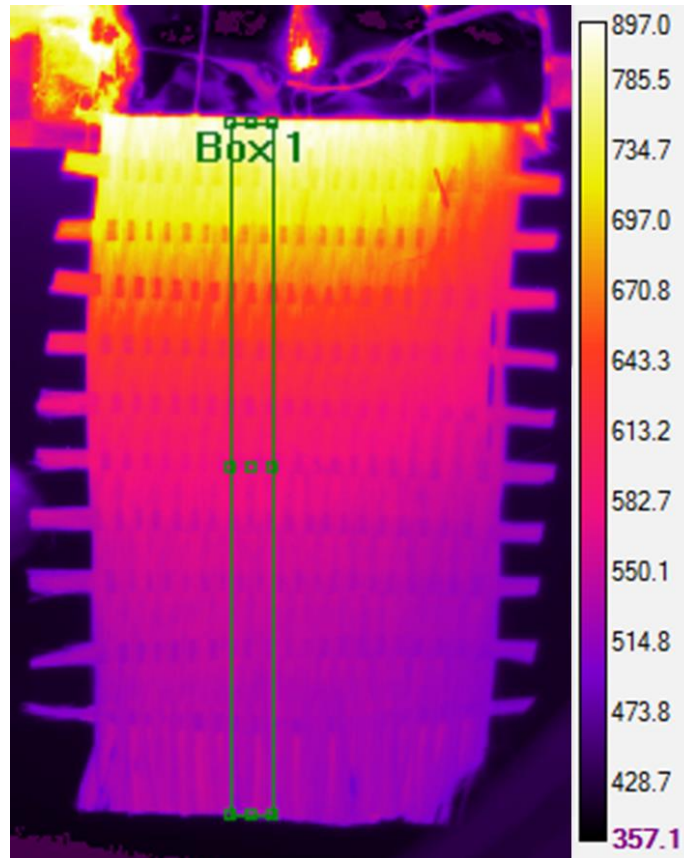
Figure 4.6: IR image of TA-E during a performance test. Temperature given in degrees K. The black line indicates the location from which the temperature profile was extracted for the thermal conductivity optimization analysis.

The result of the optimization was a thermal conductivity value of 702.5 W/m-K. Figure 4.7

shows the temperature profiles from the IR data and corresponding thermal model for an emissivity of

0.78 and effective thickness of 0.137 mm. The optimum thermal model matches the IR data very well,

with an R^2 value of 0.996. The majority of variation in the IR temperature data is attributed to the finite

thermal resistance between the longitudinal and cross tows. The uncertainty of k_{opt} with respect to

thickness is ±2.5% (±19 W/m-K). The uncertainty of k_{opt} with respect to emissivity is approximately

±1.3% (±10 W/m-K). The uncertainty of the result with regard to the radiation boundary conditions

cannot be readily quantified for this experiment due to the complexity of the surfaces and temperature

profiles in view of the fin. Based on models with extreme radiative boundary conditions (i.e., a set of

high heat pipe temperature, emissivity and environmental temperature and a set of low heat pipe

temperature, emissivity and environmental temperature) the uncertainty of k_{opt} with respect to

radiative boundary conditions is likely ±15%.

Since k_x was assumed to be constant, part of the uncertainty may be due to the variability in the

property instead of true uncertainty. Using thermal conductivity at room temperature specified by the

manufacturer and the predicted value at the average temperature of the fin, 600 K, the uncertainty of

temperature dependence of thermal conductivity was estimated to be ±2%. This uncertainty is on the

order of the uncertainty with respect to thickness and emissivity, and much less than the radiative

boundary conditions, so it was reasonable to assume a constant value.
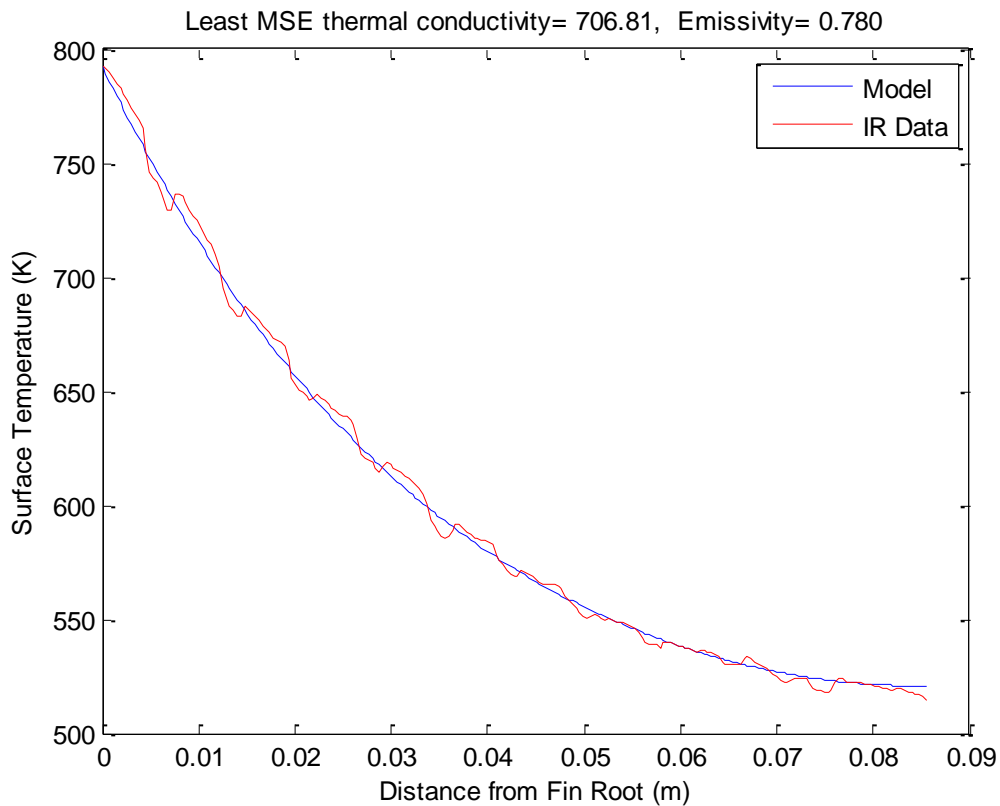
Figure 4.7: TA-E fin surface temperature data extracted from the IR image (red) and the surface temperature from the model with the optimum k_x (blue)

The same analysis was conducted on TA-F, which has an effective thickness of 0.32 mm. The IR

image in Figure 4.8 shows the region from which the temperature data was collected. As before, the

temperatures were averaged across the width of the region to reduce the variation observed in a single

profile. The k_{opt} was 495 W/m-K and Figure 4.9 shows the temperature profiles from the IR data and corresponding thermal model.

There are several reasons why this value is lower than that of TA-E. The textile has PAN fibers as the cross tows. As shown in Figure 4.10, the temperature of the PAN fibers is much less than that of the adjacent pitch fibers (about 50°C on average), since the PAN fiber thermal conductivity is on the order of 10 W/m-K. In addition to affecting the net surface temperature of the fin, the high density of PAN cross tows reduces the through-thickness thermal conductivity. Since the textile consists of three layers of pitch fibers through the thickness, the assumption that the fin has a zero void fraction is much less accurate for this configuration than for the fins with one layer. This is because each tow has a much larger fiber volume fraction than the net fiber volume fraction of a multi-layer weave. As mentioned in Chapter 3, TA-F had a narrower fin due to brazing challenges. Edge effects may have had a significant effect on the result since the numerous cross tows were conducting heat way from the centerline and the width of the fin was probably not greater than the thermal boundary layer. Lastly, the textile was handled more than the hand-woven samples, which could have caused more micro-cracks in the fibers, thereby decreasing the thermal conductivity. For all these reasons, a more rigorous test is necessary to verify the thermal conductivity of the textile.
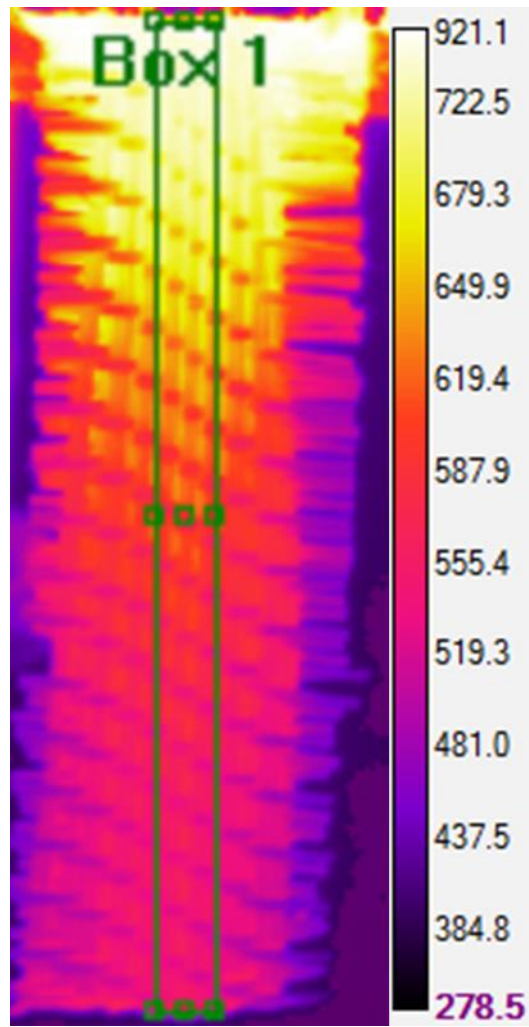
Figure 4.8: IR image of TA-F showing the area from which temperature data (in K) was collected
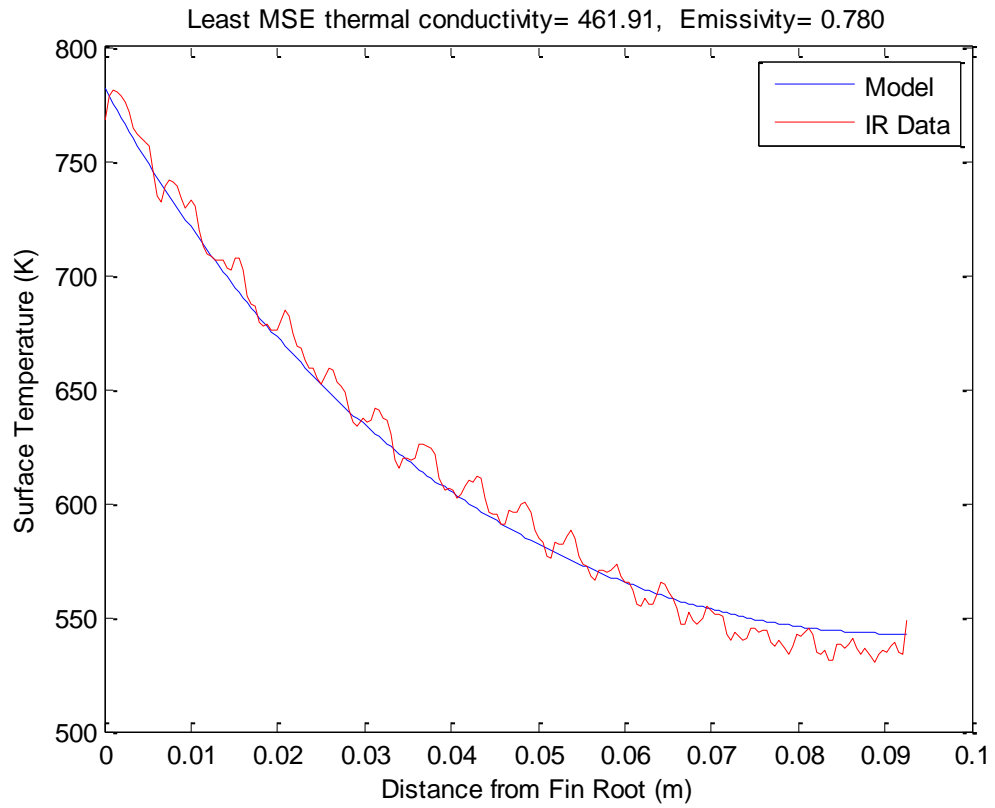
Figure 4.9: TA-F fin surface temperature data extracted from the IR image (red) and the surface temperature from the model with the optimum k_x (blue)
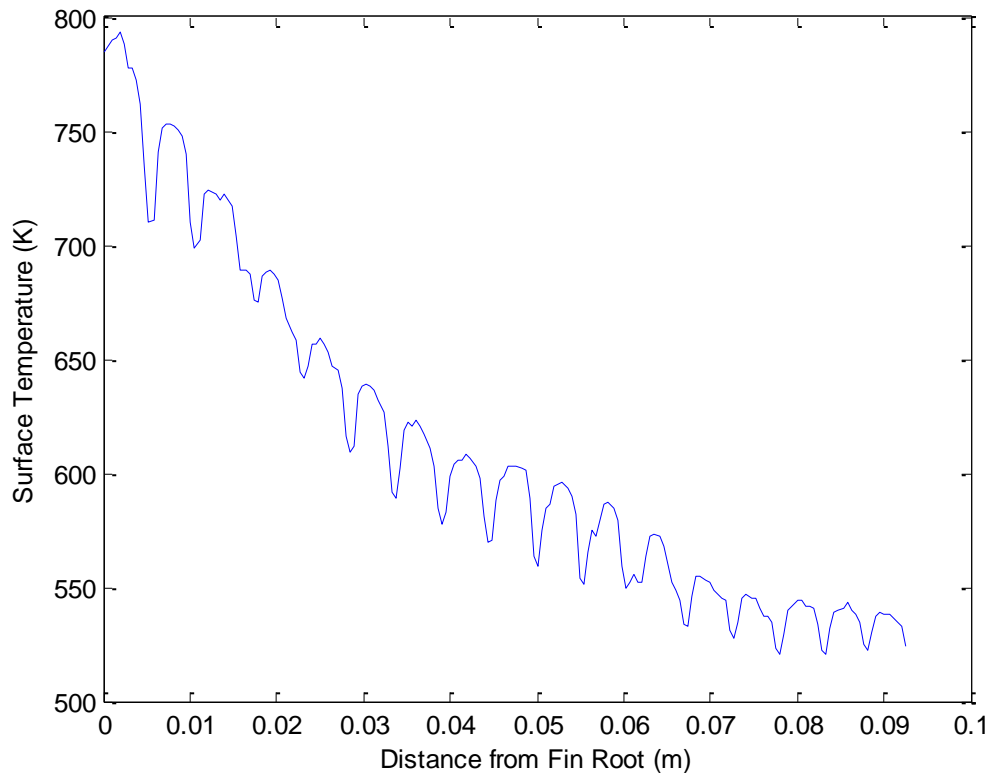
Figure 4.10: A single temperature profile from TA-F showing the steep temperature dips due to the low thermal conductivity PAN fibers in the cross direction of the textile weave

This result leads to several hypotheses about the ideal fin weave. The multiple layers in the textile were added to achieve the 0.32 mm thickness, which was predicted early in the study to maximize specific power (kW/kg). Due to the low transverse thermal conductivity of the fiber weave and the thermal resistances added by cross tows, dense, single-layer weaves may be preferred over multi-layer weaves. To achieve a net fin thickness much larger than 0.15 mm, it is suggested that two parallel fins, each half as thick as the net thickness, are attached to the heat pipe to provide a larger interface with the heat pipe and less thermal resistance through the cross section of each fin.

The hand weaves had about 20 tows per inch in the longitudinal direction and 4 cross tows per inch. The textile had 50 tows per inch of the pitch fiber and 20 tows per inch of the PAN fiber. An ideal weave would have just enough cross tows to hold the longitudinal tows in place, and use pitch fiber instead of PAN. For this first textile, PAN tows were selected as the cross tows because they are the

very flexible and had the highest likelihood of success. Now that successful weaving has been achieved

using PAN cross fibers, it is suggested that future weaves use a lower conductivity pitch fiber, like

Mitsubishi K13C2U, as the cross tows. TEAM Inc. has confirmed the viability of using K13C2U cross tows,

which may strike a more desirable balance between thermal conductivity and stiffness than either PAN

fibers or K13D2U pitch fibers.

Precise measurements of the fin thermal conductivity will be of interest later in the

development of this technology so that models can be used reliably for predicting radiative capabilities.

To obtain more exact thermal conductivity measurements, more constrained experiments are required.

Improvements on this method include creating better radiation boundary conditions from the heat pipe

and environment by shielding the fin with a constant temperature cold wall except for a narrow opening

for viewing. In addition, the assumptions related to effective thickness should be evaluated to

determine the accuracy of idealizing the fin this way, especially for multi-layer weaves.

It should be noted that the transverse thermal conductivity of the weave is not known precisely,

but the design is not expected to be sensitive to that property because the fin's length to thickness ratio

is very high. For a fin that is 8 cm long, 0.3 mm thick, with a total hemispherical emissivity of 0.8, and an

axial thermal conductivity of 800 W/m-K, the difference in the fin tip temperature when the transverse

thermal conductivity is varied between 0.1 and 100 W/m-K is less than a degree Kelvin. This result

verifies that the fin approximation (i.e., thermal gradients through the thickness are negligible compared

to the axial dimension) is valid and that measuring the transverse thermal conductivity is not justified for

this work.

4.5   Specific Heat Rejection

The specific heat rejection of the carbon fiber fins is one of the most important metrics from a

systems engineering standpoint. When properly qualified, this metric is a simple way to compare

various fin materials. The specific power rejection for a fin is unique to the heat pipe temperature, fin thickness, length, and material. The power rejected by a given fin can be estimated through the Stefan-Boltzmann radiation law using fin surface temperature data. The heat flux from a differential area on the fin surface is given by Equation 4-2. When the surface temperature profile along the fin length is known, the total power radiated from a given fin width (w_f) is found by integrating the heat flux over the fin surface, Equation 4-3. Two methods of calculating the fin power rejection from a temperature profile include: 1) analytical integration using a polynomial line-fit of the surface temperature data, and 2) numerical integration using the raw temperature data points extracted from the IR image. When working with the fin model, Comsol has a numerical integrator that will evaluate the power rejected per unit width of fin. These three methods yield nearly identical results.

$$dQ = \varepsilon\sigma(T^4(x) - T_\infty^4)dA \qquad\qquad (4\text{-}2)$$

$$Q = \varepsilon\sigma w_f \int_{x=0}^{x=l_f}(T^4(x) - T_\infty^4)dx \quad [W] \qquad\qquad (4\text{-}3)$$

To estimate the power rejected from a carbon fiber fin by numerically integrating temperature data, TA-D was tested at about 600°C and fin surface temperatures were collected using the IR camera. Surface temperature data was extracted from the IR image using the fiber emissivity of 0.78. Each pixel in the IR image contains a single temperature value, so the pixel size was converted to actual size so that the power radiated by each pixel could be calculated. The total power radiated by the fin was determined by summing the power rejected by all the pixels in the image.

Figure 4.6 shows an IR image of TA-E and the region from which temperature data was extracted. The center section of the fin was used since the edges were significantly cooler. This section was 4.9 mm wide and 8.55 cm long. The total power rejected from this region was 2.4 W. This translates to approximately 493 W/m/side heat rejected per meter of heat pipe per side of fin, which agrees to within 1% of the Comsol model, which predicts 497 W/m/side. Heat rejection of 493

W/m/side corresponds to a fin specific power of about 38.1 kW/kg. This accounts for the fin only. To

compare fin materials, the heat pipe temperature and fin dimensions must be equivalent. Figure 4.11

compares the specific heat rejection of the carbon fiber fins with copper, molybdenum and a carbon-

carbon (C-C) composite fins at several temperatures to demonstrate the advantage of using the highly-

conductive, lightweight fibers. Copper is not a viable option for the higher temperatures since it melts

at 1084°C, but was added for comparison because it is one of the most highly conductive metals.

Molybdenum was added because it is a viable metal for operation at 600°C, and C-C composite was

added because it is the most closely related material to bare carbon fiber that has ever been evaluated

for space radiator fins.

The carbon fiber properties estimated in the previous sections were used to generate a thermal

model in Comsol. Likewise, a Comsol model was generated for copper, molybdenum, and C-C

composite. Standard temperature-dependent thermal conductivity values were used for the metals.

The thermal conductivity values for C-C composites were based on measurements by Denham *et. al.*

using unidirectional C-C panels designed for spacecraft radiators [41]. The thermal conductivity

variation with temperature for each material used for this analysis is given in Table 4.1. Space radiators

are typically coated with high-emissivity paint, so an emissivity of 0.8 is assumed for the copper,

molybdenum and C-C fins. Comsol was used to evaluate the total power rejected for each material and

temperature.

Table 4.1: Thermal Conductivity (W/m-K) for various fin materials at three elevated temperatures

Root Temp.	400 °C	600 °C	800 °C	Source
Copper	375	361	347	[89]
Molybdenum	128	123	118	[90]
C-C	400	350	300	[38]
Carbon Fiber	715	680	645	extrap. from Section 4.4.2

The carbon fiber fins provide an increasing advantage over molybdenum from about 5.6 to 9.6 times more rejected power per mass as the heat pipe temperature increases from 400 to 800°C. Similarly, the carbon fiber fin rejects from 5.0 to 5.2 times as much power per mass from 400 to 800°C as the copper fin. Lastly, carbon fiber fin rejects from 1.2 to 1.4 times as much power per mass from 400 to 800°C as the C-C fin. Compared to the metals, the carbon fiber's low density and high thermal conductivity result in unmatched specific power capabilities. Since the density of C-C is very close to that of the carbon fibers, the primary penalty to specific power of C-C fins is attributed to the lower thermal conductivity. Strictly from a thermal perspective, the C-C fin performs moderately compared with the carbon fiber fin, however, there are other design attributes that make C-C difficult to use including the brazing issues described in Section 3.4.
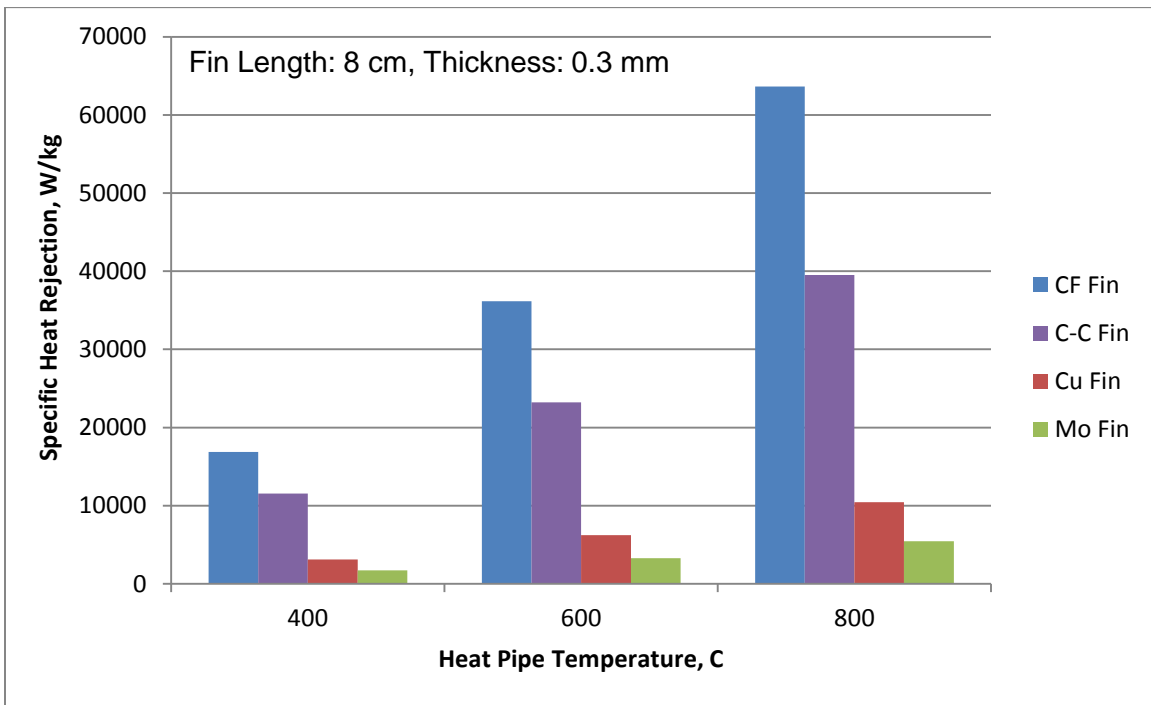
Figure 4.11: Comparison of specific heat rejection for carbon fiber, C-C, copper and molybdenum fins with the dimensions as noted

As research on lightweight materials continues, fibers and composites with higher thermal conductivity will likely be available in the future, further increasing the specific heat rejection potential.

For example, carbon fibers exceeding 1200 W/m-K have been fabricated [78], but were not available for this study.

4.6   Conclusions

The total hemispherical emissivity of the Mitsubishi K13D2U fiber weave was determined from measurements of the spectral reflectivity. The room temperature measurement of total hemispherical emissivity was 0.74±0.01. Using the spectral data, the emissivity at 600°C was found to be 0.78±0.01. The combination of fin models and experimental fin temperature data enabled a non-contact method of measuring the axial thermal conductivity of fiber bundles. This novel method overcomes limitations for fiber bundles that limited prior work to single fibers. The thermal conductivity of the hand-woven fiber mat was found to be 707±100 W/m-K for a fin with an average temperature of 600 K. In Section 4.5, the thermal conductivity was extrapolated to higher temperatures for predicting the specific power using the fin model. The radiated power calculated by the fin model was then compared with the calculated radiated power from the experiment and the results agreed to within 1%. Finally, the validated fin models showed that even with a thermal conductivity of about 700 W/m-K, carbon fiber fins have much better performance than competing materials and that the advantage increases with temperature. Further developments in higher-conductivity fibers should lead to even greater heat rejection capabilities.

CHAPTER 5

HEAT REJECTION SYSTEM MODELING AND OPTIMIZATION

5.1   Introduction

The previous chapters focused on details of the fin and fabrication methods, but it is the

performance of the radiator as part of a spacecraft heat rejection subsystem that determines the

viability of the carbon-fiber-fin. This study investigates effects of the radiator design on the heat

rejection subsystem (HRS) mass and efficiency. A thermal resistance model of the HRS with sodium heat

pipes and carbon fiber fins was built to predict the required radiator size for various subsystem

conditions. The thermal resistance model is a completely analytical model of the HRS, which can be

used to predict optimum design points for various HRS objectives. An optimization study was conducted

to find the minimum HRS mass design for a 300 kWe, high-temperature power conversion system test

case.

5.2   Analytical Formulation of the Radiation from a Fin

Since the radiator fin heat transfer problem can be solved only by numerical methods, having an

analytical approximation of the fin heat rejection is very useful for automating radiator design analyses.

A closed form approximation of the radiator-fin-efficiency was developed by Henry V. Chang to calculate

the power radiated from a finned heat pipe radiator valid for certain operating conditions [91]. Chang's

formulation is a generalized equation for fin efficiency with the following free parameters: fin thickness

(at the root and tip if thickness varies), length, thermal conductivity, surface emissivity, root

temperature (i.e., heat pipe temperature), and environmental temperature. Chang's formulation has

been useful for low-temperature heat radiators operating near 100°C [45], but Chang's model generates

large errors at temperatures above 600 K. To demonstrate the need for a high-temperature extension

of Chang's model, Chang's predictions are compared with results from a finite element model of a heat

pipe radiator for a range of fin-root temperatures and fin lengths. The finite element model was generated in Comsol Multiphysics, which solved for the temperature profile through the fin and determined the heat radiated by integrating the Stefan-Boltzmann equation over the fin surface. Figure 5.1 shows contour plots of the heat rejected from a heat pipe radiator versus fin-root temperature and fin length generated by Chang's model and by the Comsol model. The line in the upper right corner of the plot showing Chang's approximation is a boundary above which Chang does not define the approximation. This comparison shows that the error between the Chang model and the detailed finite element model solution is quite large, thus a new model is proposed.
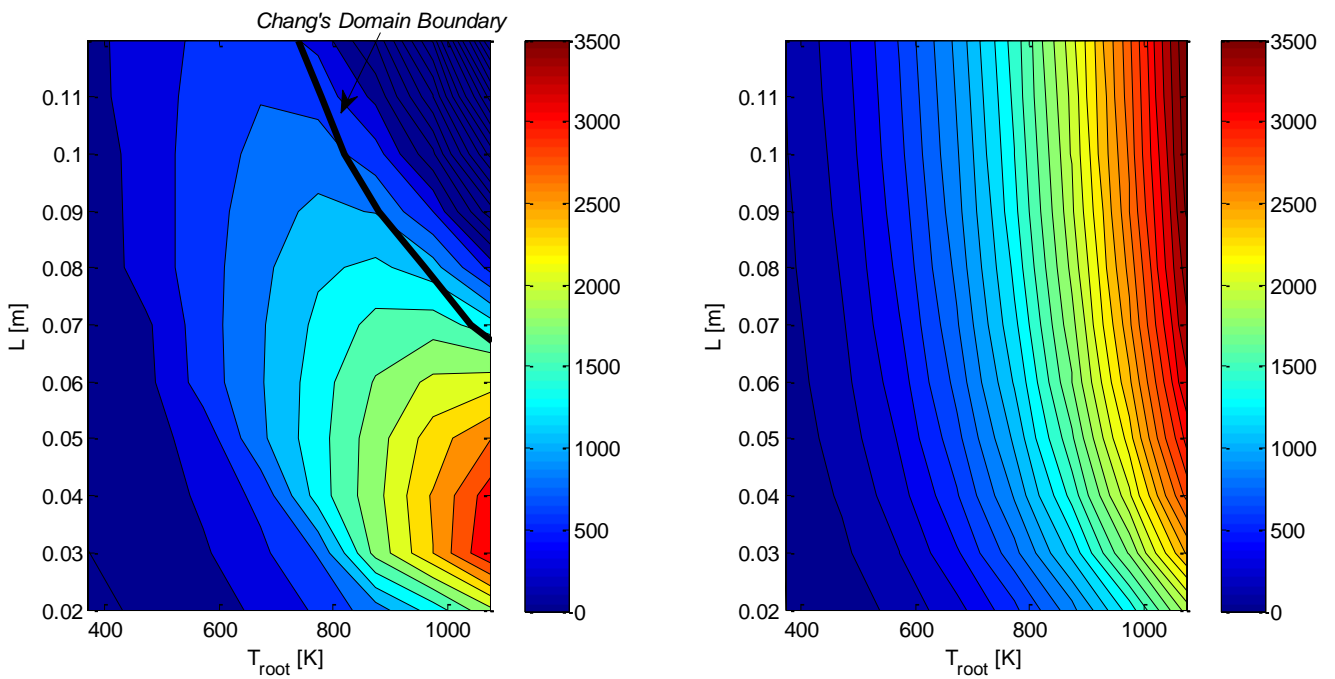
Figure 5.1: Contour plots of radiated power per unit length of heat pipe (W/m heat pipe) versus fin length and root temperature (for a 0.3 mm thick fin) as predicted by the Chang model (left) and by Comsol (right) using fin material that has a thermal conductivity of 800 W/m-K and emissivity of 0.78

A new analytical model for the heat radiated from a heat pipe with carbon fiber fins was generated. The model predicts the radiated power per unit length of heat pipe for various fin effective thicknesses, fin lengths, and fin-root temperatures (i.e. heat pipe condenser temperature). The effective thickness is the net thickness of the carbon fiber fin assuming 100% fiber volume fraction. The

heat pipe emissivity is set to 0.15 and the fin emissivity and thermal conductivity are set to 0.78 and 800

W/m-K respectively. These properties are specific to the carbon fiber used in this study; however, this

analysis can be quickly duplicated for other fin and pipe materials.

The study on fabrication of test articles in Chapter 3 indicated that using two thinner, parallel

fins instead of a single, thicker fin may be more efficient due to low through-thickness thermal

conductivity and increased thermal contact with the heat pipe. For this reason, the radiator design

assumed for this model was a heat pipe with two parallel fins attached to the pipe as shown in Figure

5.2. The model accounts for internal radiation heat transfer among the heat pipe and both fins, and

external radiation to space. Numerical solutions of the problem were obtained using Comsol for fin-root

temperatures, fin thicknesses and fin lengths ranging from 200-800°C, 0.1-1 mm, and 2-12 cm

respectively. These limits proved to bound the optimum design space sufficiently for high-temperature

radiator applications. A 3-dimensional, fourth-order polynomial was fit to the heat rejection data by

running a multivariate linear regression in Matlab. This polynomial model is referred to as

$Q_{fin}(L_f, t_f, T_1)$, where L_f is the fin length, t_f is the effective fin thickness, and T_1 is the fin-root

temperature. Equation 5-1 gives the condensed form of this 34-term polynomial. The error between

Q_{fin} and the detailed model data for all cases was below 6% and the average error magnitude was less

than 1%, where root temperature was in the range of 400-800°C, fin length was in the range of 3-12 cm,

and fin thickness was in the range of 0.2-1 mm. The R^2 value of Q_{fin} and the data was 0.9999 for that

design space. The error increases significantly when the fin length is below 0.03 m and when the root

temperature is below 300°C. Chang's formulation was generalized to include variations in thermal

conductivity and emissivity, which was accomplished by lumping parameters. While lumping

parameters simplified the final form of Chang's approximation, it resulted in significant errors in some

regions of the design space. Higher accuracy could be achieved with Q_{fin} by limiting the design space

and using a fourth order polynomial instead of lumping parameters. Since the uncertainties in the

carbon fiber thermal conductivity and emissivity measurements were relatively low, those properties

were not taken to be free parameters in the approximation developed here, but the approximation

could be extended in future work to include the fin's thermal conductivity and emissivity (i.e.,

$Q_{fin}(L_f, t_f, T_1, k, \varepsilon)$).

Figure 5.2: Heat pipe with the two parallel fin configuration used in thermal models accounting for
radiation heat transfer between surfaces and the symmetry boundary on the right

$$Q_{fin}(L_f, t_f, T_1) = \sum_{i=0}^{3} \sum_{j=0}^{i} \sum_{k=0}^{j} \sum_{l=0}^{k} a_{ijkl} x_i x_j x_k x_l \qquad (5\text{-}1)$$

where $x_1 = 1, x_2 = L_f, x_3 = t_f, x_4 = T_1$

Figure 5.3 shows a contour plot of a slice of $Q_{fin}(L_f, T_1)$ for a thickness of 0.3 mm showing the

locations of the data points from the parameter sweep. Figure 5.1 shows contour plots of Q_{fin} and the

percent error of Q_{fin}. The error plot shows that the error is greatest at lowest temperatures for the

shortest fins but remains below 10% for the entire region shown.
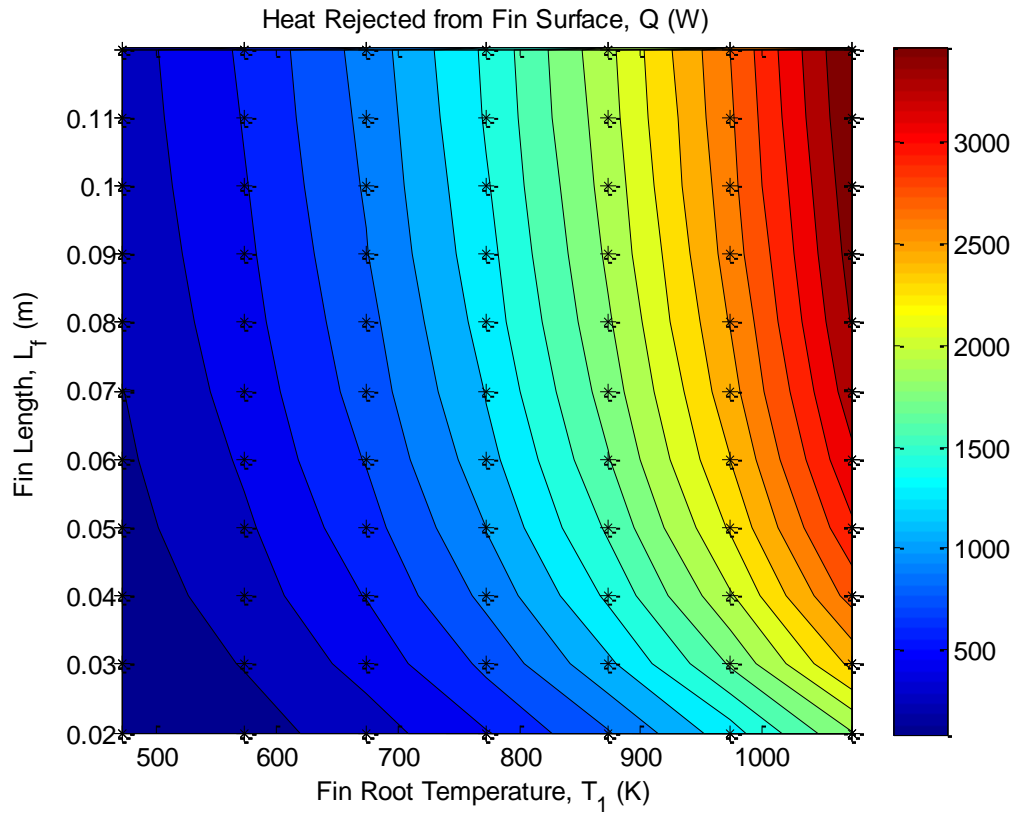
Figure 5.3: Contour slice of $Q_{fin}(L_f, T_1)$ (W/m length of heat pipe) for an effective fin thickness of 0.3 mm showing the data points (*) from the parameter sweep
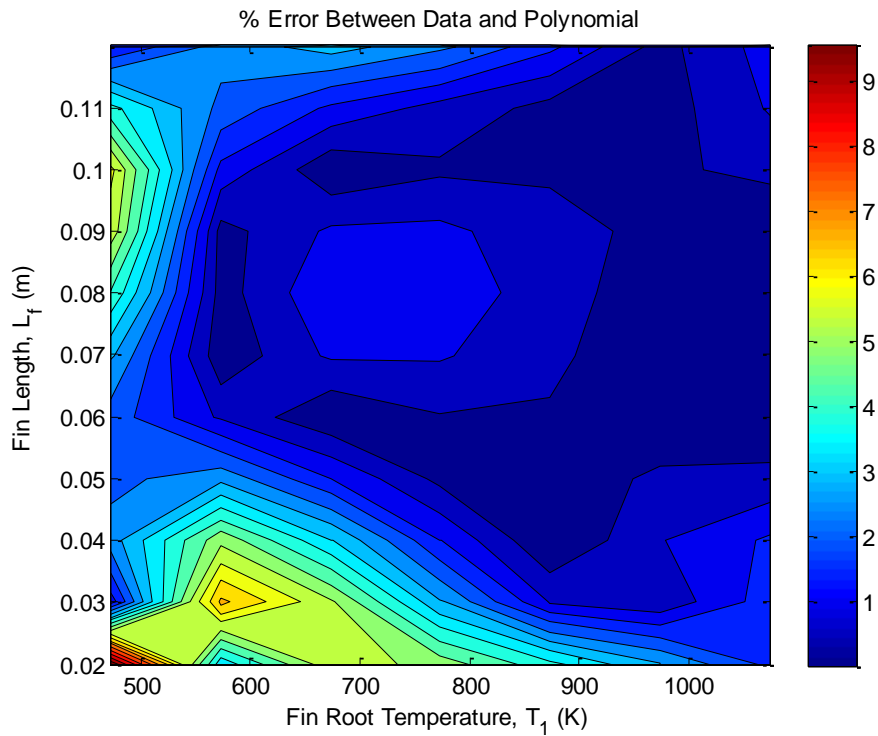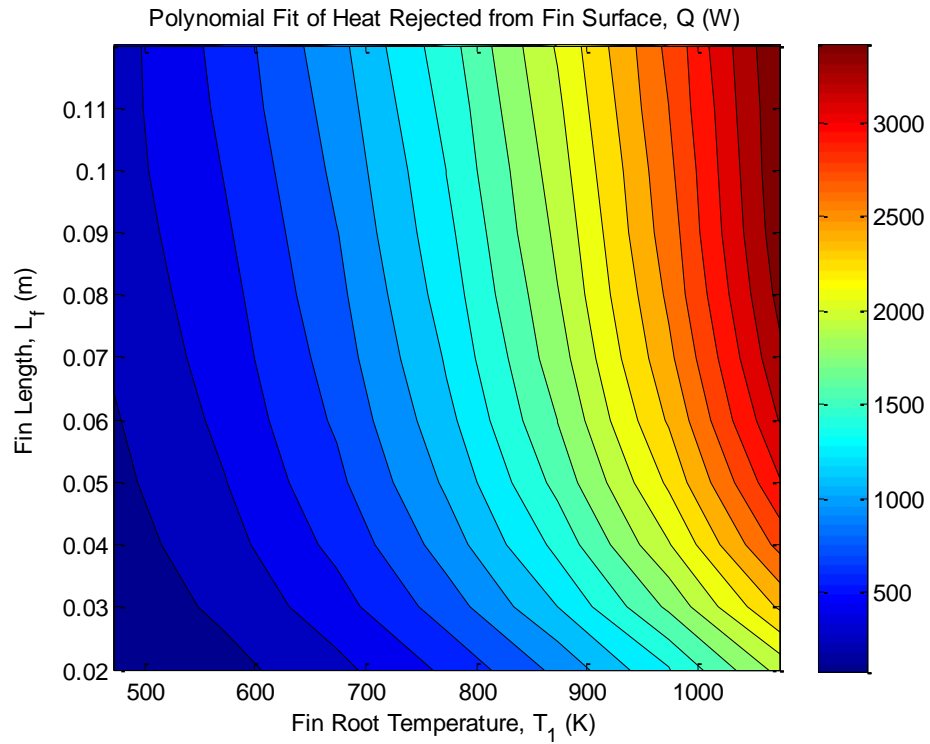
Figure 5.4: Contour plots of the fourth order polynomial fit of $Q_{fin}(L_f, T_1)$ for a fin thickness of 0.3 mm (top), and the percent error between the fit and the Comsol model results of Q_{fin} (bottom)

Several curves of radiated power versus fin length and root temperature are given in Figures 5.5-5.7 for different fin thicknesses. Radiated power increases asymptotically to a maximum with fin length. Figures 5.8-5.9 show that the slope of $Q_{fin}(L_f)$ decreases significantly by L_f=10 cm. Fins are not typically longer than 10 cm, because the fin efficiency decreases rapidly with additional length.
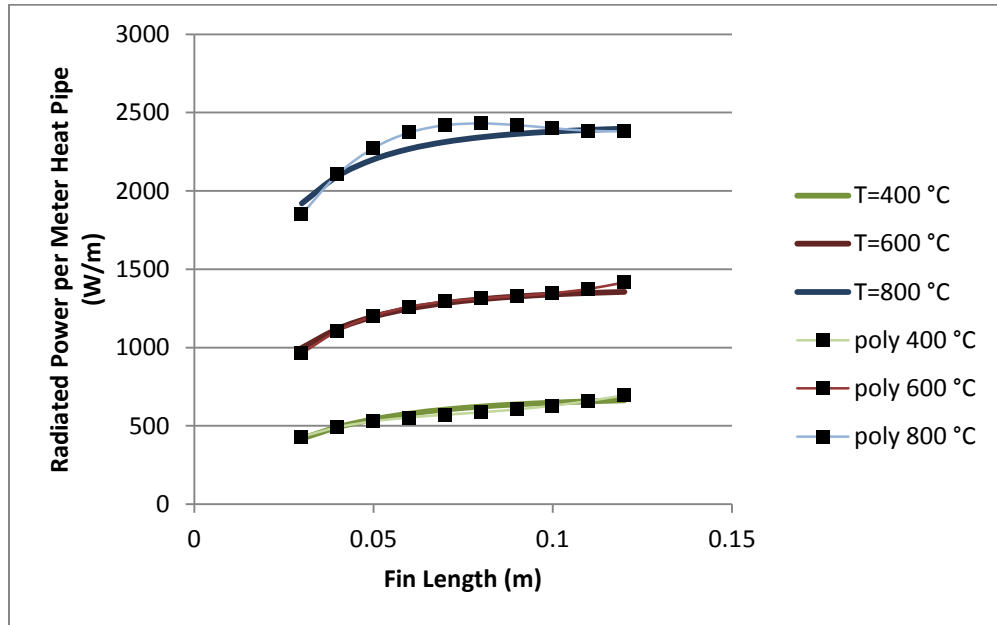
Figure 5.5: Radiated power per meter of heat pipe versus fin length at various root temperatures for a fin thickness of 0.1 mm. The curve for 800°C shows the limitation of Q_{fin} for the smallest thicknesses.

143
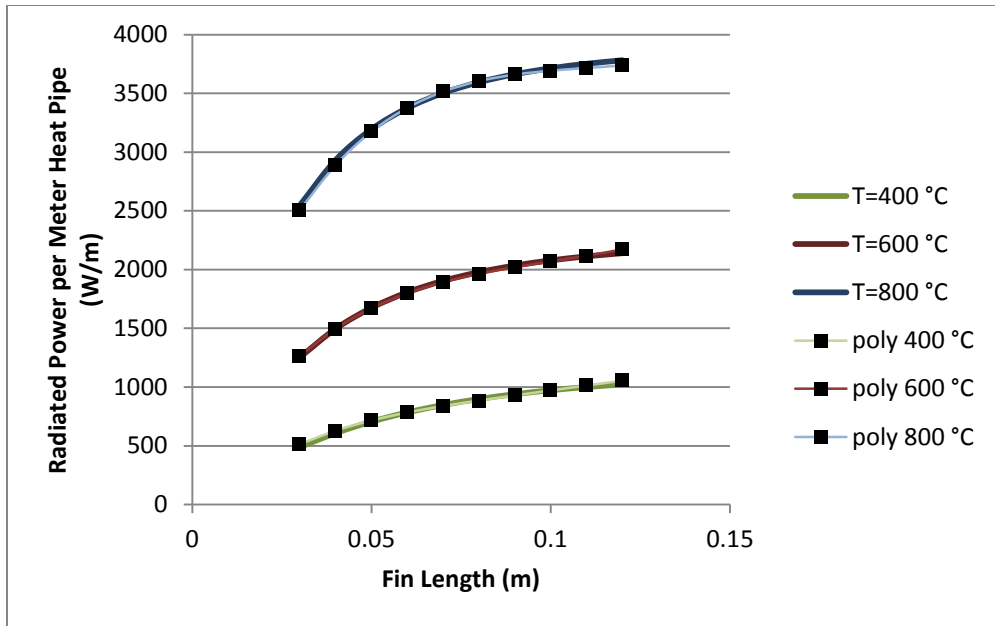
Figure 5.6: Radiated power per meter of heat pipe versus fin length at various root temperatures for a fin thickness of 0.5 mm
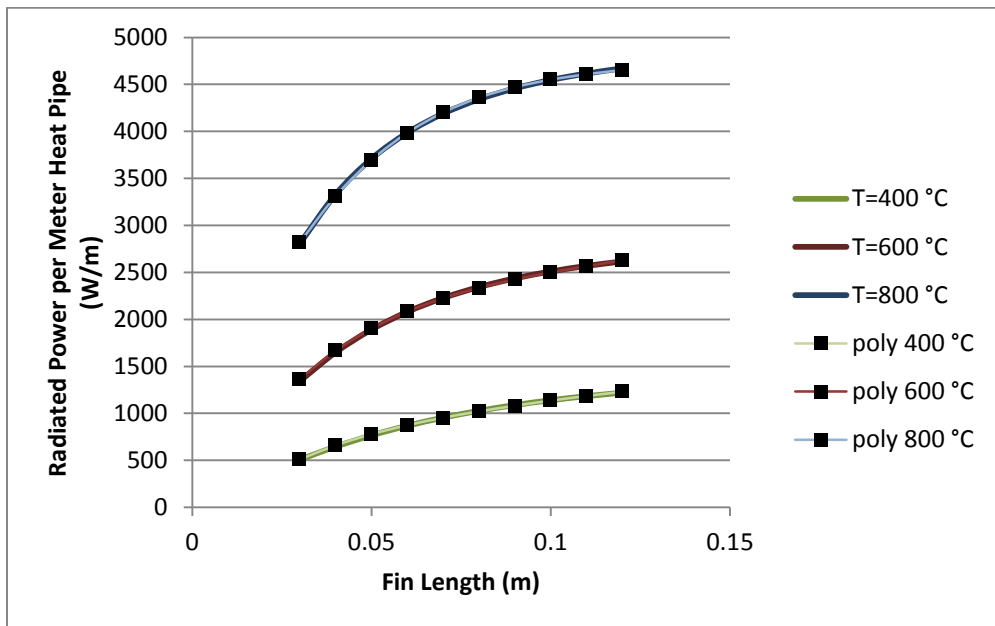
Figure 5.7: Radiated power per meter of heat pipe versus fin length at various root temperatures for a fin thickness of 1 mm

Figure 5.8 shows the radiated power per unit length of heat pipe versus fin length and fin

thickness for a root temperature of 600°C. The effect of fin thickness is small for short fins and then

increases to an asymptote for longer fins. The fin surface temperature, and thus radiated power,

strongly depends on the conductive thermal resistance of the fin, which is inversely proportional to

thermal conductivity and thickness. The conductive thermal resistance for short fins is lower than for

long fins, so the surface temperature of short fins remains closer to the root temperature. This explains

the increased influence of thickness on radiated power with fin length as shown in Figure 5.8. As with

fin length, there is a point at which adding thickness results in diminishing additional radiated power.

The optimum thickness lies near the point at which the slope of power with thickness starts declining

noticeably, typically around 0.3 mm.
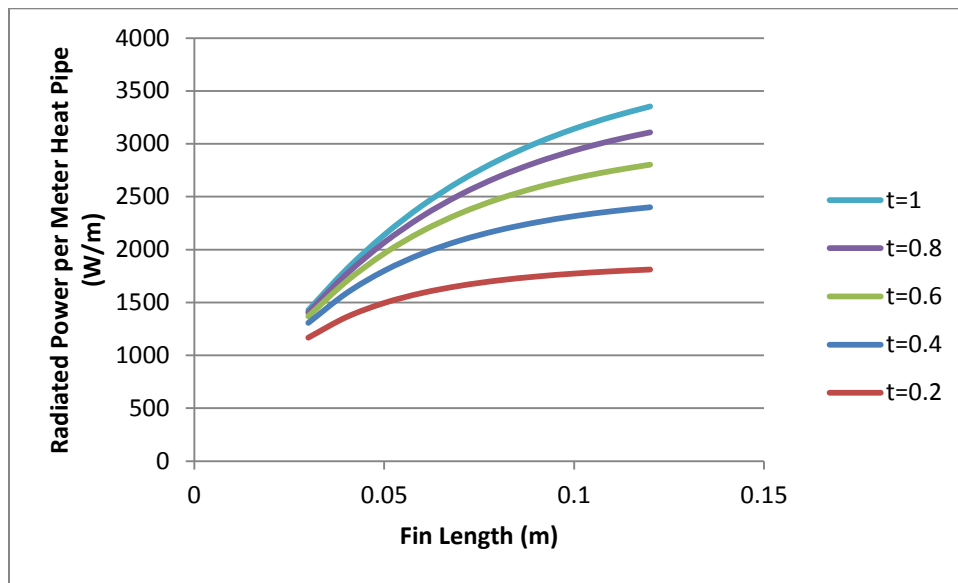
Figure 5.8: Radiated power per meter of heat pipe versus fin length at various fin thicknesses (mm) for the root temperature of 600°C
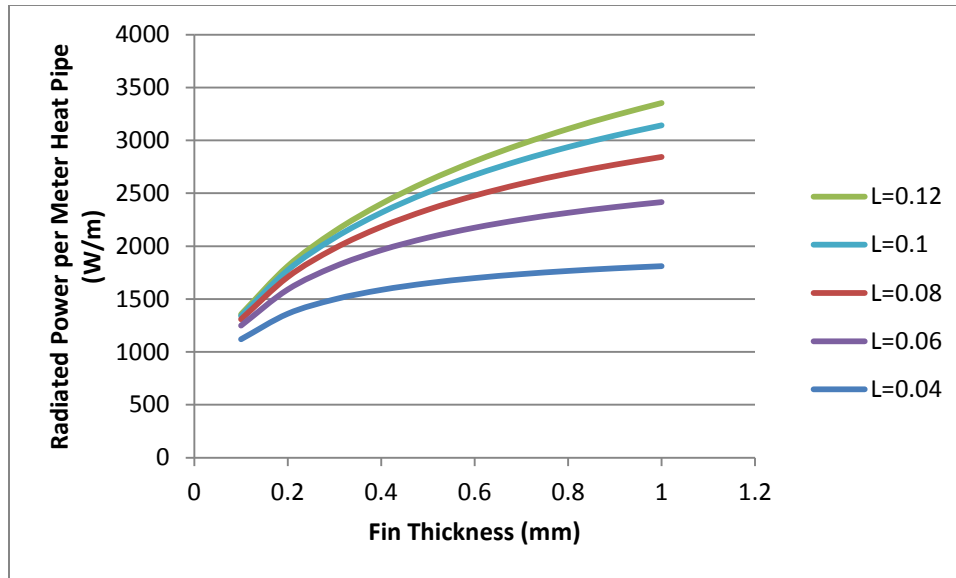
Figure 5.9: Radiated power per meter of heat pipe versus fin thickness at various fin lengths (m) for the root temperature of 600°C

The two-fin configuration maximizes the total power rejected to space for a given total fin thickness due to the radiation heat transfer between heat pipe and fins. For a lower limit on fin heat rejection for a given fin thickness, assuming no radiation from the heat pipe, a single fin with a purely conductive heat source at the fin root was considered. A 3-dimensional fourth order polynomial for the power radiated per meter of heat pipe for this configuration is provided in the Appendix. The percent difference in the total radiated power between these two configurations was less than 10% for all cases studied here (i.e., T_1: 200-800°C, L_f: 0.03-0.12 m, and t_f: 0.1-1 mm). This demonstrates that the trends observed in Q_{fin} are not highly sensitive to the configuration of the fin, thus these findings can be used to approximate the fin performance for any of three basic fin configurations: the double fin with a heat pipe (as was used for Q_{fin}), the single fin with no heat pipe, and the single fin with a heat pipe.

Lastly, the fin efficiency was also evaluated for this design space since it is another common way to characterize fin performance. Fin efficiency is typically defined as the fraction of heat radiated by the fin under consideration to the heat radiated from an ideal fin (i.e., isothermal at the fin-root temperature and radiating to a 0 K enclosure). The fin efficiency was calculated for each fin design point

that was used in the development of Q_{fin}. Figure 5.10 shows contour plots of fin efficiency at three

different fin root temperatures. As the fin length increases, the fin efficiency decreases because the fin

is less isothermal. The fin efficiency increases with fin thickness because the conductive thermal

resistance is reduced, which increases the heat flux along the fin and thus surface temperature at

distances further from the root. With increasing root temperatures, the fin efficiency decreases because

a larger temperature gradient is required to supply the increased radiation, so the fin surface near the

root is much hotter than the fin tip. A 3-dimensional fourth order polynomial for fin efficiency is also

provided in Appendix Table A.3.
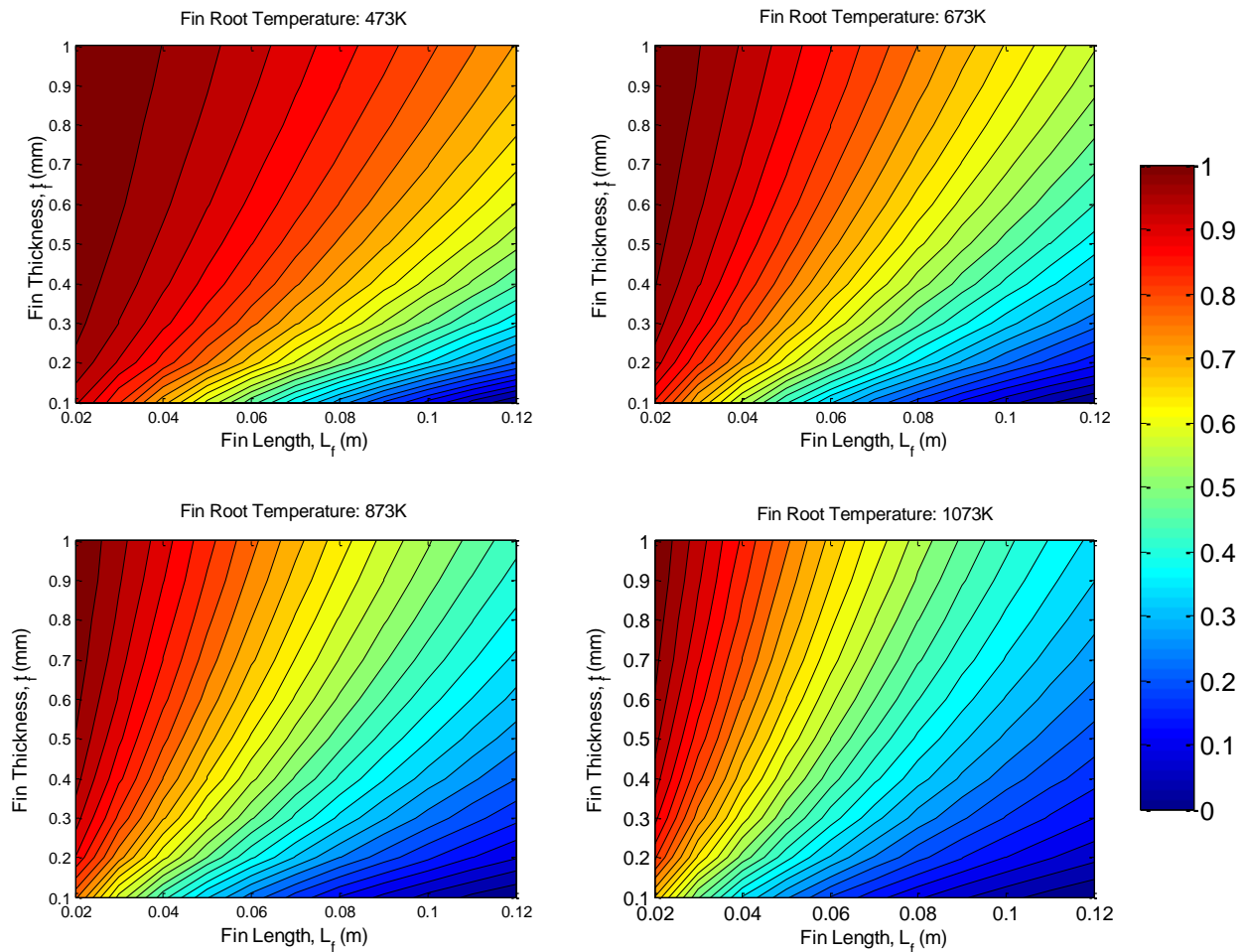
Figure 5.10: Carbon fiber fin efficiency versus fin thickness and length for fins with: thermal conductivity
of 800 W/m-K, emissivity of 0.78, and root temperatures as noted

The analytical formulation of the carbon-fiber fin described in this section can be easily

incorporated into larger heat rejection subsystem models, as demonstrated in the following sections.

5.3   Thermal Resistance Modeling of Heat Transfer Devices

A thermal resistance model is analogous to an electrical resistance model, where current is

replaced with heat flux. This is a cost-effective way to predict the thermal performance of a system

when the heat transport path can be reasonably modeled by a collection of series or parallel flow paths.

This method is especially useful in early design stages of a thermal component where high-fidelity finite

element simulations are not yet feasible or affordable. In the case of the HRS, the heat transport from

the coolant to each heat pipe can be modeled by a series of convective or conductive thermal

resistances and then a set of parallel paths of conductive and radiative thermal resistances from the fin

root to the fin surfaces.

Figure 5.11 shows the basic components of an NEP-HRS including the coolant pipe, coolant

pump, coolant accumulator, hot-end heat exchanger and cold-end radiator. Figure 5.12 shows a single

radiator-heat-pipe section with the coolant pipe, heat pipe annulus evaporator, heat pipe condenser

and radiating fins. The heat pipe annulus evaporator concept was developed by Advanced Cooling

Technologies presented in Ref. [79]. Figure 5.13 shows the thermal resistances from the coolant to the

fin surfaces. Equations for conductive, convective and radiative thermal resistances are given in Table

5.1. The radiation heat transfer coefficient, h_r, given in the table is valid when the surface temperature

is much greater than the environmental temperature, which is applicable for most spacecraft

applications where the environmental temperature is near absolute zero. This heat transfer coefficient

depends on only the fin surface emissivity and temperature. For fins with large surface temperature

gradients, the error in h_r can be reduced by averaging the surface temperatures or subdividing the fin

into small isothermal elements. Chapter 4 demonstrated that the drop in surface temperature along an

8 cm carbon fiber fin was approximately 300°C when the root temperature was near 600°C. To avoid

complications associated with estimating h_r, the heat transfer in the fin was modeled using the

analytical fin heat rejection formulation, Q_{fin}, developed in Section 5.2.
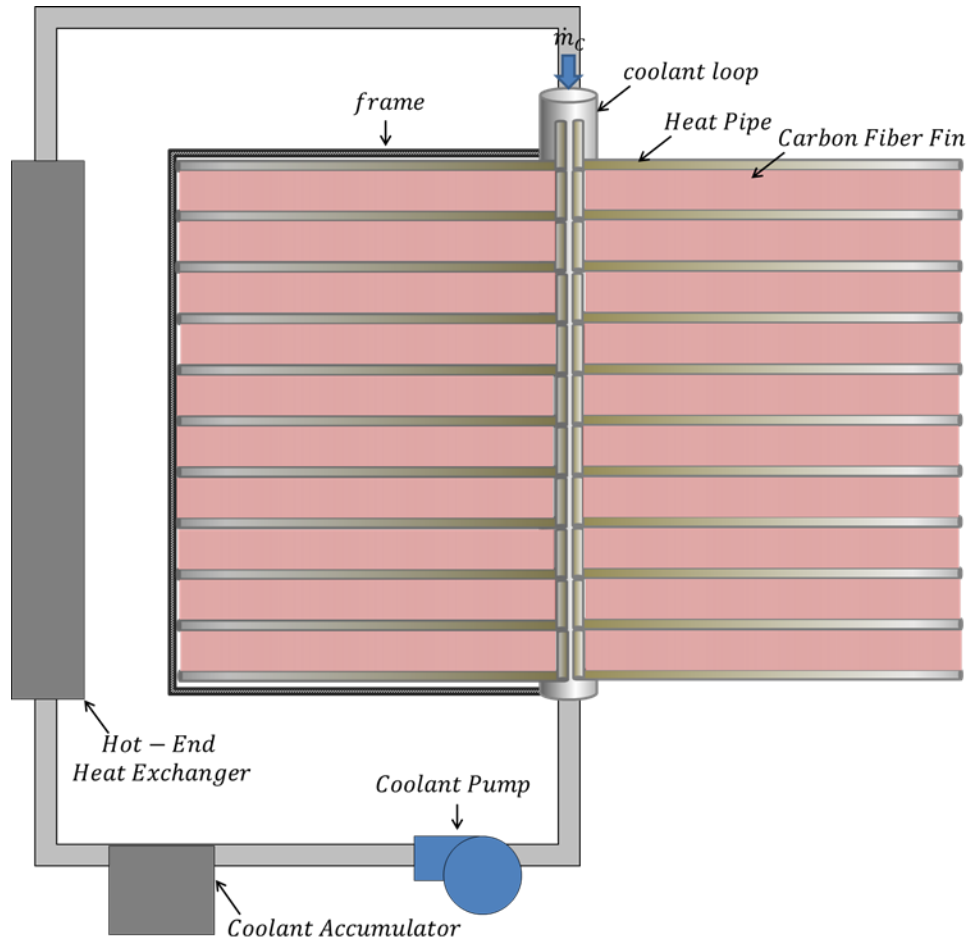
Figure 5.11: Schematic of HRS showing the hot-end heat exchanger, the coolant pump, coolant pipe and radiator
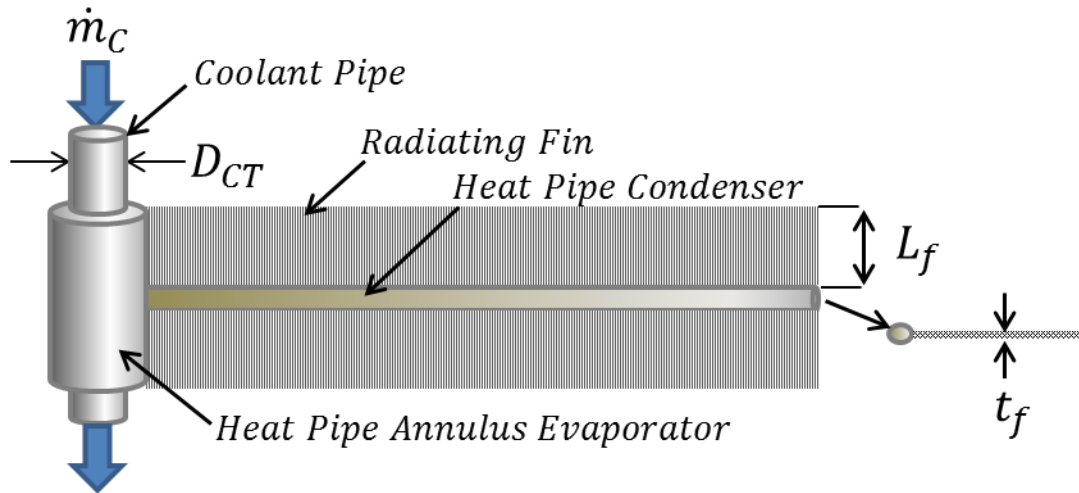
Figure 5.12: Schematic of the interface between the coolant and radiator, showing a single heat pipe and radiating fins
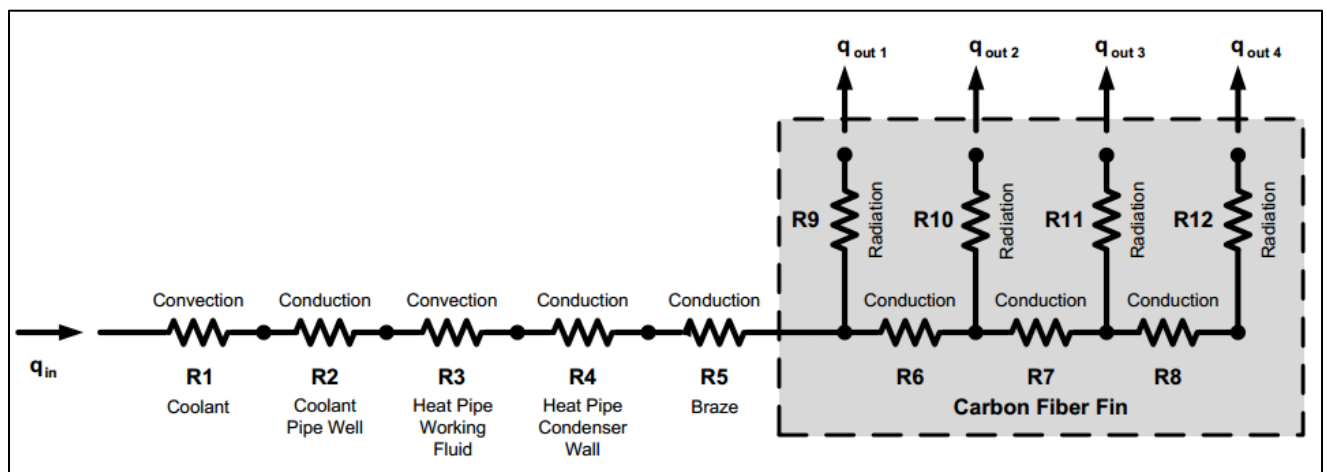
Figure 5.13: Thermal resistance diagram of the heat transport path from the coolant to the fin surfaces

Table 5.1: Equations of Thermal Resistances for Conduction, Convection and Radiation

Conductive Resistance through a Flat Surface	$r_{cond} = \dfrac{t}{kA}$
Conductive Resistance through a Cylindrical Surface	$r_{cond} = \dfrac{R_2 \ln\left(\dfrac{R_2}{R_2}\right)}{k * (2\pi R_1 L)}$ $where\ R_1\ and\ R_2\ are\ the\ inner\ and\ outer\ radii$
Convective Resistance	$r_{conv} = \dfrac{1}{hA}$
Radiative Resistance	$for:\ T_{env} \ll T_s$ $r_{rad} = \dfrac{1}{h_r A}$ $h_r = \sigma \varepsilon T_s^3$

The details of the HRS thermal resistance model are described below.

5.3.1   Heat Rejection Subsystem Model

The components of the HRS included in this subsystem model were the coolant pipe, coolant fluid, coolant pump, heat pipes, radiating fins, and structural radiator frame. The hot-end heat exchanger and coolant accumulator were not included in the HRS system boundary since they interact with the power converter and that is not in the scope for this project.

The thermal resistance model calculates the mass of the HRS for the specified design point. The model determines how many radiator sections, as shown in Figure 5.12, are required to reject the specified amount of waste heat. Radiator sections are added one by one until all of the waste heat has been rejected, and then the total mass is calculated.

In the following sections, the symbols D, R, A, L, t, H_d, u, $\dot{m}$, $\dot{V}$, μ_c, c_p, k, ρ, T, and Q represent diameter, thermal resistance (or radius where specified), area, length, thickness, hydraulic diameter, velocity, mass flow rate, volumetric flow rate, dynamic viscosity, heat capacity, thermal conductivity, density, temperature, and heat flux respectively. The subscripts CP, C, P, HPE, HPC, $HPCW$, f, B, and Fr correspond to the coolant pipe, coolant, pump, heat pipe evaporator, heat pipe condenser, heat pipe condenser wall, fins, braze, and radiator support frame respectively

5.3.1.1 HRS Thermal Resistance Model

To calculate the heat rejected from each radiator-heat-pipe section, the thermal resistance from the coolant to the fin root is calculated. From the fin root, Q_{fin} was used to calculate the simultaneous heat conduction through and radiation from the fin. The heat transfer from the coolant to the fin root is assumed to be a series of one-dimensional conduction and convection steps, as shown in the thermal resistance diagram in Figure 5.13. Equation 5-2 describes the series thermal resistance model up to the fin root.

$$R_1 = R_C + R_{CP} + R_{HPC} + R_{HPCW} + R_B \qquad (5\text{-}2)$$

Where:

R_C is the convective thermal resistance between coolant and heat pipe evaporator. Note that the Nusselt Number correlation given in Equation 5-7 is for turbulent liquid metal flow in a pipe with constant wall heat flux [92]. This was the closest Nusselt Number approximation to this problem.

$$R_C = \frac{1}{h_c A_c} \qquad (5\text{-}3)$$

$$A_c = \pi D_{CP} L_{HPE} \qquad (5\text{-}4)$$

$$h_C = \frac{Nu * k_c}{H_d} \qquad (5\text{-}5)$$

$$H_d = D_{CP} \tag{5-6}$$

$$Nu = 4.82 + 0.0185 * (Pr * Re)^{0.827} \tag{5-7}$$

$$Pr = \frac{\mu_c c_p}{k_c} \tag{5-8}$$

$$Re = \frac{\rho_c u H_d}{\mu_c} \tag{5-9}$$

$$u_D = \frac{\dot{m}}{\rho_c A_{CP}} \tag{5-10}$$

$$A_{CP} = \frac{\pi D_{CP}^2}{4} \tag{5-11}$$

R_{CP} is the conductive thermal resistance of the cylindrical coolant pipe wall:

$$R_{CP} = \frac{R_{CP2} \ln\left(\frac{R_{CP2}}{R_{CP2}}\right)}{k_{CP}*(2\pi R_{CP1} L_{HPE})} \tag{5-12}$$

Where R_{CP1} and R_{CP2} are the inner and outer radii of the coolant pipe respectively.

R_{HP} is the convective thermal resistance of heat pipe working fluid. Heat pipes are designed to operate

isothermally, so this resistance is assumed to be negligible.

$$R_{HP} = \frac{1}{h_{HP}*(\pi D_{HP} L_{HP})} \tag{5-13}$$

R_{HPCW} is the conductive thermal resistance of the cylindrical heat pipe condenser wall:

$$R_{CP} = \frac{R_{HPC2} \ln\left(\frac{R_{HPC2}}{R_{HPC2}}\right)}{k_{HP}*(2\pi R_{HPC1} L_{HPC})} \tag{5-14}$$

Where R_{HPC1} and R_{HPC2} are the inner and outer radii of the heat pipe condenser respectively.

R_B is the conductive thermal resistance of the braze layer. It is assumed that the braze joint covers half

of the heat pipe diameter.

$$R_B = \frac{t_B}{k_B*(\pi D_{HPC} L_{HPC})} \tag{5-15}$$

Equation 5-16 is the steady state heat flow into the fin root, where T_1 is unknown.

$$Q_{in} = \frac{T_C - T_1}{R_1} \tag{5-16}$$

To solve for T_1, and thus Q_{in}, Equation 1-18 must be balanced by the heat rejected by the fins

using Equation 5-17, which accounts for the length of the heat pipe condenser and both fins that are

attached to the heat pipe. The fin-root temperature T_1 is determined by using a root-finding solver to

find the temperature that satisfies $Q_{in} = Q_{HPTotal}$. Having solved for T_1, the total heat rejected from

the current heat pipe was calculated using Equation 5-17

$$Q_{HP\ Total} = L_{HPC} * 2 * Q_{fin}(T_1, L_f, t_f) \tag{5-17}$$

Once the amount of heat rejected from that heat pipe was determined, the coolant

temperature and quantity of remaining waste heat was updated. The temperature of the coolant

decreases as heat is rejected with each successive heat pipe, as given in Equations 5-18 and 5-19 where

the superscript i is for the current heat pipe. With the updated coolant temperature (Equation 5-19),

radiator-heat-pipe sections were added in a loop until the current value of the remaining waste heat

was less than 100 W.

$$\Delta T_c^i = \frac{Q_{HPTotal}}{\dot{m} c_p} \tag{5-18}$$

$$T_c^{i+1} = T_c^i - \Delta T_c^i \tag{5-19}$$

$$Q_{waste}^{i+1} = Q_{waste}^i - Q_{HPTotal}^i \tag{5-20}$$

Once the heat rejection loop was complete, the pressure drop through the coolant pipe is

calculated using the Darcy–Weisbach Relation (Equation 5-21). The Darcy friction factor, f, was

calculated using the Swamee-Jain approximation for a full-flowing circular pipe. The required pumping

power was calculated using Equation 5-22 and was used later as a constraint in the mass optimization

analysis.

$$\Delta P = \frac{f L_{CT} \rho_c u_{CT}^2}{2 D_{CT}} \tag{5-21}$$

$$P_p = \eta_p \dot{V}_c \Delta P \tag{5-22}$$

The final step in the HRS model was to calculate the total subsystem mass. The masses of the coolant, coolant pipe, heat pipes, and carbon fiber fins are all calculated directly using the dimensions and densities of the materials. A structural frame with a mass of 30% of the radiator mass was also added. The pump mass was estimated using the relationship given in Equation 5-23, which is based on experimental data of liquid metal electromagnetic induction pumps [55].

$$M_p(\Delta P, \dot{m}) = 11.5 * ln\,(10^{-5} * \Delta P * \dot{m}) + 20.8 \tag{5-23}$$

5.3.1.2 Thermal Resistance Model Validation

Validating the physics of the thermal resistance model could be accomplished by comparisons with experimental data or with a finite element simulation of the entire HRS. Neither experimental nor finite element simulation data was available. A high-fidelity HRS finite element model can be built, but was out of scope for this work. John Siamidis at NASA Glenn Research Center has built finite element models for low-temperature NEP-HRS's [26][28], so future work could involve collaboration with his group to validate the thermal resistance model developed here.

In the absence of system data, limiting cases can be tested to ensure the thermal resistance model produces the expected trends. For a given system, increasing the coolant flow rate should decrease the coolant temperature drop along the radiator, the number of heat pipes, and the total radiator area, while increasing the coolant pressure drop. Figure 5.14 shows these trends for a system with coolant pipe diameter of 4 cm and a fin length and thickness of 8 cm and 0.3 mm respectively. The pressure drop increases with approximately the square of coolant flow rate as expected from Equation 5-22. Also, the coolant temperature drop across the radiator tends to zero with increasing flow rates. This is because the coolant heat flux is higher with increased flow rates while the total waste heat dissipated by the radiator remains constant, as given by Equation 5-24.

$$Q_{waste} = \dot{m}_c * c_p * \Delta T_c \tag{5-24}$$

At the extreme of near-infinite coolant flow rate, the coolant would be isothermal, which would

maximize the radiator surface temperature, achieving high fin efficiencies. High flow rates are not

desirable from a system perspective due to tradeoffs with pumping power and mass. Above a coolant

flow rate of about 4.6 kg/s, the pumping power consumes more than 5% of the electric power produced

by the engine, which is undesirable from an efficiency standpoint. As the magnitude of the slope of the

coolant temperature drop starts decreasing near $\dot{m}_c$=1.5 kg/s, so does the magnitude of the slope of the

number of heat pipes and radiator area. For a given amount of rejected heat, when the coolant

temperature drop is smaller, the total number of heat pipes is smaller because more of the radiator is

hotter, increasing the efficiency of the fin radiation.
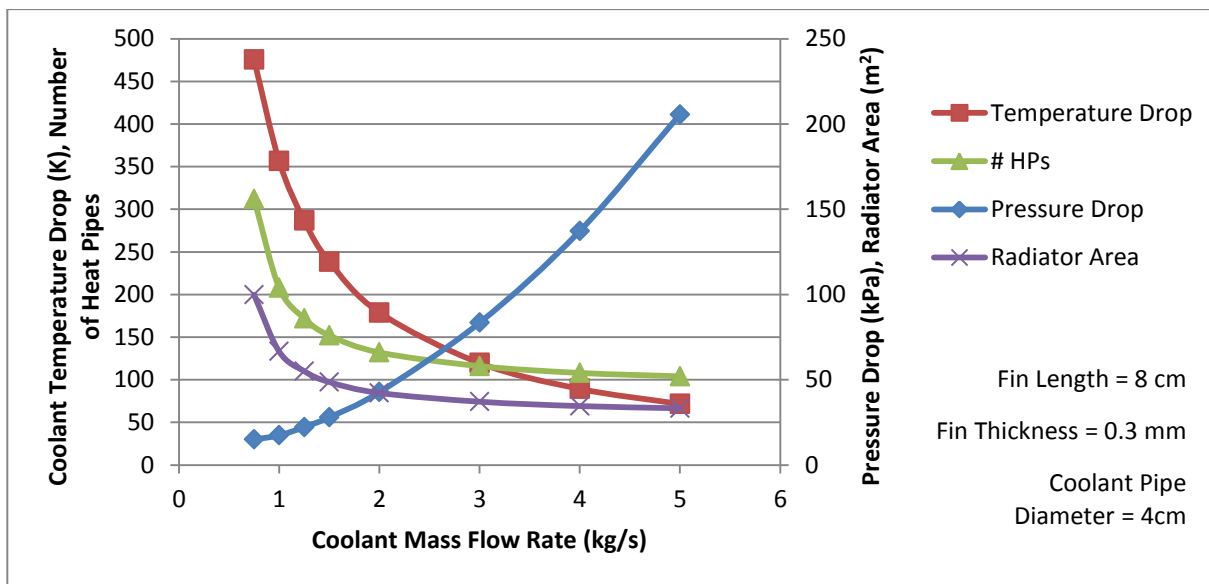
Figure 5.14: Coolant temperature and pressure drops, number of required heat pipes, and total radiator area (projected area, which is half of the total radiating surface) versus coolant mass flow rate for the specified HRS

Figure 5.15 shows the HRS mass versus fin length for a system with a coolant flow rate of 1.5

kg/s, coolant pipe diameter of 4 cm and fin thickness of 0.3 mm. As expected, there is a minimum near 8

cm. The pump mass stays constant and coolant outlet temperature remain nearly constant as expected

from Equation 5-24. The number of heat pipes decreases with increasing fin length because more heat

gets rejected per heat pipe. Even though the number of heat pipes decreases, the radiator length (i.e., length of coolant pipe interfacing with the heat pipes) increases steadily. The mass of the coolant, coolant pipe, heat pipe evaporators and fins increase with radiator length. So as the fin length increases, there is a tradeoff between fewer heat pipes and greater heat transport mass that balances near a fin length of 6 cm.
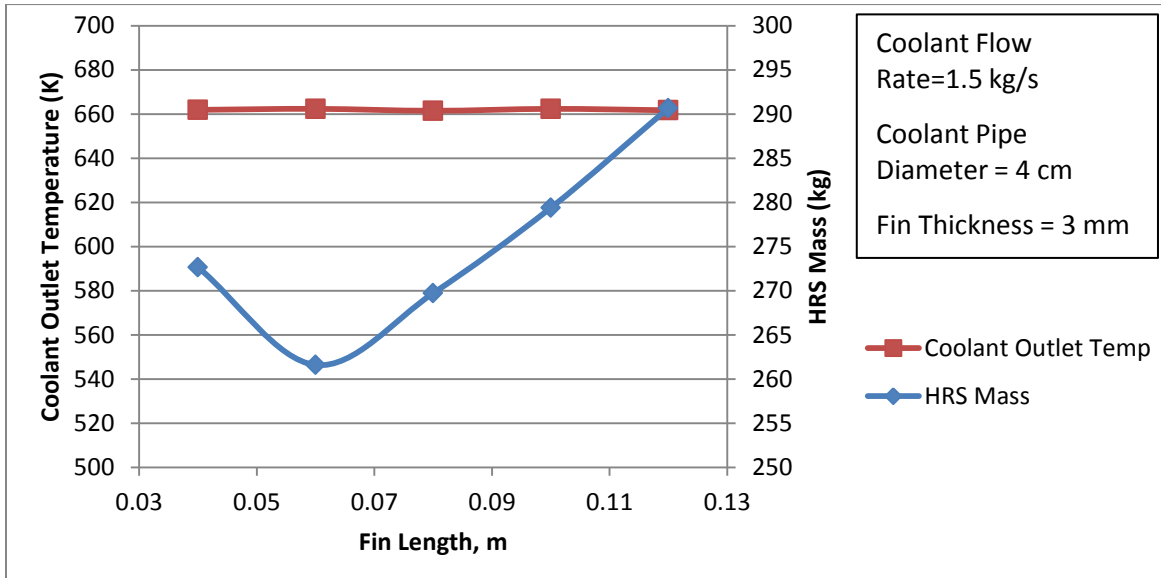
Figure 5.15: HRS mass and coolant outlet temperature versus fin length for the specified HRS

5.3.2   HRS Mass Optimization

Various HRS performance measures can be optimized using the thermal resistance subsystem model described above, including mass, area, and total radiator fin efficiency. The completion of the thermal resistance model was one function evaluation in the optimization study. The goal of this optimization study was to minimize the HRS mass objective function, given in Equation 5-25.

Four constraints were imposed on the design: 1) the pumping power may not exceed 5% of the total electric power generated by the power conversion system, Equation 5-26; 2) the total length of the radiator must be less than 100 m, Equation 5-27; 3) the coolant outlet temperature must not be less than 300 K below the coolant inlet temperature, Equation 5-28; and 4) the coolant pressure drop must

be below 400 kPa due to the limitations of the coolant pump, Equation 5-29. The coolant pumping

power was limited because the pump is powered by the electric power generated by the conversion

system itself, so there must be a significant net power output from the conversion system to power the

electric thrusters. The radiator length was limited due to spacecraft vehicle size and construction

constraints. The coolant pump, which was assumed to be an Annular Linear Induction Pump (ALIP), can

generate NaK mass flow rates in the range of 1-1.5 kg/s at pressures below 400 kPa [91]. The ALIP pump

was designed for NASA during the JIMO project for the purpose of pumping NaK coolant in an NEP HRS

[91].

$$M_{HRS}(\bar{x},\bar{p}) = M_{CP} + M_C + M_P + M_{HPE} + M_{HPC} + M_f + M_B + M_{Fr} \tag{5-25}$$

$$g_1(\bar{x},\bar{p}) = \frac{P_p(\bar{x},\bar{p})}{P_{gen}} - 0.05 \leq 0 \tag{5-26}$$

$$g_2(\bar{x},\bar{p}) = L_{HE}(\bar{x},\bar{p}) - 100 \leq 0 \tag{5-27}$$

$$g_3(\bar{x},\bar{p}) = (T_{inlet}(\bar{p}) - T_{outlet}(\bar{x},\bar{p})) - 300 \leq 0 \tag{5-28}$$

$$g_4(\bar{x},\bar{p}) = \Delta P_{coolant}(\bar{x},\bar{p}) - 400 \leq 0 \tag{5-29}$$

Where M_{HRS} is the total HRS mass, M_i is the mass of the component i, g_i is a constraint, $\bar{x}$ is the set of

design variables, $\bar{p}$ is the set of HRS parameters, P_p is the power consumed by the pump, P_{gen} is the

power generated by the conversion cycle, L_{HE} is the length of the radiator-coolant heat exchanger,

T_{inlet} and T_{outlet} are the coolant temperatures at the radiator inlet and outlet respectively, and

$\Delta P_{coolant}$ is the coolant pressure drop through the radiator-coolant heat exchanger.

Many subsystem parameters can be selected as design variables; however, four were selected

for this HRS optimization study. The design variables ($\bar{x}$) included: coolant mass flow rate ($\dot{m}_C$), coolant

pipe diameter (D_{CT}), fin length (L_f), and fin thickness (t_f). The design variables and their respective

bounds are listed in Table 5.2. The coolant flow rate is limited by the capacity of the current state-of-

the-art liquid metal pumps. Limits on the coolant transport pipe diameter are set based on typical HRS

coolant pipe dimensions, which are also compatible with the ALIP pump. The fin length and thickness

limits are set based on what is expected to be reasonable based on the fin geometry optimization

conducted in Chapter 3. The input parameters ($\bar{p}$) are geometric and operational parameters that are

set for each test case. These parameters are given in Table 5.3. Typical values for these parameters

were collected from the literature [26].

The coolant pipe and heat pipe were assumed to be stainless steel because it can be used at 900

K and is less dense than refractory metals. The annulus heat pipe evaporator had a radius 1.5 cm

greater than the coolant pipe to provide space for the wick material, which was based on the Advanced

Cooling Technologies design [79]. The heat pipe condenser was assumed to be 0.1905 cm (0.75 inch) in

diameter and was filled 5% by volume with sodium working fluid. The wall thicknesses for the coolant

pipe, heat pipe evaporator and condenser were assumed to be 0.5 mm.

Table 5.2. Design Variables and their Bounds

Design Variables ($\bar{x}$)		Bounds
x_1	$\dot{m}_C$ (kg/s)	1-1.5
x_2	D_{CP}(cm)	2-5
x_3	L_f (cm)	3-12
x_4	t_f (mm)	0.1-1

Table 5.3. Fixed Input Parameters ($\overline{\mathbf{p}}$)

Material Properties (coolant, pipe, heat pipe, braze, fin)	
Density (ρ) Thermal Conductivity (k) Heat Capacity (coolant only) (c_p) Viscosity (coolant only) (μ)	(*typ. values*)
Operational	
Power Conversion Cycle Efficiency (η) Power Generated by Cycle (P_{gen}) Waste Heat (P_{waste}) Coolant Max Temperature (T_{inlet}) ALIP Coolant Pump Efficiency (η_p)	*depends on test case* 0.15
Geometric	
Circular Coolant Pipe Coolant Pipe Wall Thickness (t_w) HP Annulus Evaporator Diameter (D_{HPE}) HP Condenser Diameter (D_{HP}) HP Condenser Length (L_{HPC}) HP Wall Thickness (t_w) HRS Configuration: heat pipes aligned parallel to each other, radiating fins view only space	 0.5 mm D_{CP}+3 cm 2 cm 2 m 0.5 mm

5.3.2.1 Optimization Methods

Two optimization software packages, Matlab and ModelCenter, were used to solve this constrained HRS mass minimization problem. Matlab's optimization toolbox offers several algorithms including a global search genetic algorithm tool, *ga*, and several gradient-based tools. In general, genetic algorithms are used for global searches because they use heuristic sampling methods that make them much less vulnerable to local minima as compared with gradient-based methods. The basic steps of a genetic algorithm optimization tool are described in the Matlab documentation and include: picking an initial population of points across the design space, evaluating the objective and constraint functions, "mutating" the points to test how the objective function changes with the design variables, generating a new generation with more of the population placed in regions with promising objective values, and iterating that process until the population converges on the solution [54].

In theory, genetic algorithm tools should converge to the global minimum, but in practice it is possible for the solution to converge to a local minimum if the design space sampling or mutation methods are not robust enough for the complexity or instability of the problem. This is why genetic algorithm solvers do not guarantee finding the global optimum, even though they can typically find a near-optimal solution. From near-optimal points, it may be possible to use a gradient-based solver to search locally and find an improved solution. Running a genetic algorithm tool several times with different start points is a good way to validate that the optimum solution was found.

In addition to the Matlab *ga* tool, the Phoenix Integration software called ModelCenter was used. ModelCenter has 35 optimization tools that can be used for a wide variety of problems. The tool that ModelCenter suggested for solving this constrained optimization was called Design Explorer, which uses surrogate models. A surrogate model is an analytical approximation of the actual objective function obtained by fitting a curve to data sampled from the design space. The basic steps in the Design Explorer tool in ModelCenter include sampling the design space, generating a surrogate model, optimizing the surrogate model, calculating the actual function value at the optimal point, and then iteratively refining the surrogate model until the optimal point over multiple iterations converges. In addition to Design Explorer, ModelCenter has numerous genetic algorithm tools that are suitable for solving this problem. Among the tools described here, a near-optimal point was found and validated.

5.3.3   Optimization Method Verification and Validation

The optimization verification was demonstrated by showing convergence of the objective function and constraints using the Design Explorer tool, as shown in Figure 5.16. A basic validation of the optimal solution was achieved by using multiple optimization tools and start points, and demonstrating that they each found very similar solutions. This validation is shown in the results section.
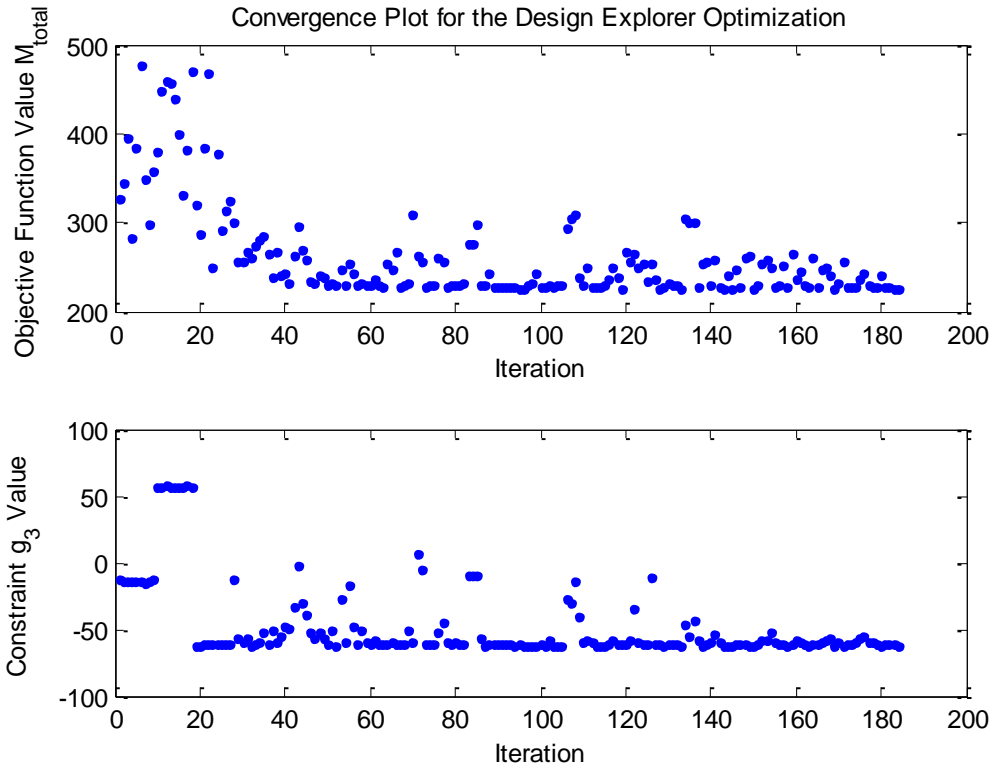
Figure 5.16: Convergence plot for a ModelCenter Design Explorer optimization simulation

5.3.4   Test Case Selection

Lee Mason, branch chief of the Thermal Energy Conversion Branch at the NASA Glenn Research Center, reports that NASA's Project Prometheus [31][58] helped to identify test cases that are aligned with NASA's interests. Table 5.4 shows power conversion systems that could be considered for different mission timeframes, assuming that increasing power will be desired with time. A mid-term 300 kWe potassium-Rankine (k-R) system was selected for the test case because it operates at high temperatures and scales very well at high power levels. These attributes make the k-R system an exciting candidate for incorporating a high-temperature heat rejection system.

Table 5.4. Candidate Power Systems for Various Mission Timeframes

Mission Timeframe	Candidate Power Systems for different Power Classes		Reject Temp (K)	TRL
	Up to 100 kWe			
2020's	SiGe TE (SP-100)		800	6-9
	CBC 1200K (JIMO)		450	5-6
	K-Rankine 1500K		900	2-3
	50 to 500 kWe			
2030's	CBC 1200K (JIMO)		450	5-6
	K-Rankine 1500K		900	2-3
	MHD		600	1-2
	2 to 10 MWe			
2040's	CBC 1200K (JIMO)		450	5-6
	K-Rankine 1500K		900	2-3
	MHD		600	1-2

5.3.5   Test Case Results

In total, nine optimization simulations were run: five to find the minimum HRS mass of the test case, and four investigating other conditions. The five mass optimization simulations were run using various optimization tools and start points. Table 5.5 summarizes the results.

All five simulations found approximately the same solution, which validates that the true global solution is near these points. Simulations 1-3 used Design Explorer with different start points. The ModelCenter genetic algorithm tool called Darwin was used for Simulation 4, and Matlab *ga* was used for Simulation 5. Design Explorer required no more than 3 hours to converge for every simulation, while the two genetic algorithm tools required over ten times the computational time. This demonstrates the advantage of surrogate models over genetic algorithms. Due to the efficiency with which Design Explorer found near-optimal points, it was selected as the primary tool.

Simulation 4 found the most-optimal point for the coolant mass flow rate of 1.50 kg/s, coolant pipe diameter of 2.7 cm, fin length of 6.6 cm (i.e., heat pipe spacing of 13.2 cm), and fin effective

thickness of 0.395 mm. This resulted in a HRS mass of 224.49 kg, a total radiator area (twice the

radiator footprint) of 77.66 m^2, and a radiator efficiency of 30.28%. Radiator efficiency is the ratio of

waste heat load to the power that could be radiated from the area of the radiator if it were isothermal

at the maximum coolant temperature. Figure 5.17 shows a contour plot of the HRS mass versus x_3 and

x_4 where x_1 and x_2 are held constant at the optimal values of 1.5 kg/s and 0.027 m respectively.

Visualizing the HRS mass response surface helps to confirm that that the location of the optimal solution

was identified by Simulation 4. The complex shape of the contours shows why global search algorithms

are required to find the true minimum. The area within the minimum contour indicates that there is a

set of suitable solutions that yield near-optimal designs.

Table 5.5: Summary of Optimization Results for Simulations 1-5

Simulation Number	1	2	3	4	5
Optimization Tool	Design Exp.	Design Exp.	Design Exp.	Darwin	Matlab *ga*
Power Generated [kWe]	300	300	300	300	300
Waste Heat Load [kWt]	700	700	700	700	700
Objective	min Mass	min Mass	min Mass	min Mass	min Mass
Simulation Time [hr]	1.1	1.85	1.6	>50	>80
Number of Iterations Req'd	156	241	206	>5,000	>10,000
Initial Conditions					
Mass flow rate [kg/s]	1.25	1	1.5	1.5	N/A
Coolant Pipe Diameter [m]	0.04	0.02	0.05	0.03	N/A
Fin Length [m]	0.08	0.04	0.12	0.07	N/A
Fin Thickness [mm]	0.3	0.3	1	0.4	N/A
Optimal Solution					
Mass flow rate [kg/s]	1.479	1.500	1.500	1.450	1.500
Coolant Pipe Diameter [m]	0.027	0.027	0.027	0.027	0.027
Fin Length [m]	0.074	0.070	0.069	0.066	0.063
Fin Thickness [mm]	0.447	0.406	0.372	0.395	0.395
HRS Total Mass [kg]	226.90	225.08	225.68	**224.49**	226.60
Constraint Values					
% pump/generated power	1.78	1.72	1.65	1.77	1.51
Radiator Length [m]	10.38	10.23	10.38	9.96	9.76
ΔT [K]	241.13	237.64	237.57	237.70	237.80
ΔP [kPa]	202.38	193.54	185.22	198.79	169.82
Other HRS Results					
Radiator Efficiency [%]	29.06	29.47	29.05	30.28	30.91
Number of Heat Pipes	140	146	150	152	156
Radiator Area [m^2]	41.51	40.93	41.52	39.83	39.02
Radiating Surface Area [m^2]*	83.02	81.85	83.04	79.66	78.04
Radiator Areal Density [kg/m^2]	1.94	1.95	1.91	2.01	2.07
HRS Areal Density [kg/m^2]	2.73	2.75	2.72	2.82	2.90
HRS Specific Power [kWt/kg]	3.09	3.11	3.10	3.12	3.09
Effective Rad Temperature [K]	660.79	663.13	660.75	667.64	671.08

* Twice the radiator footprint
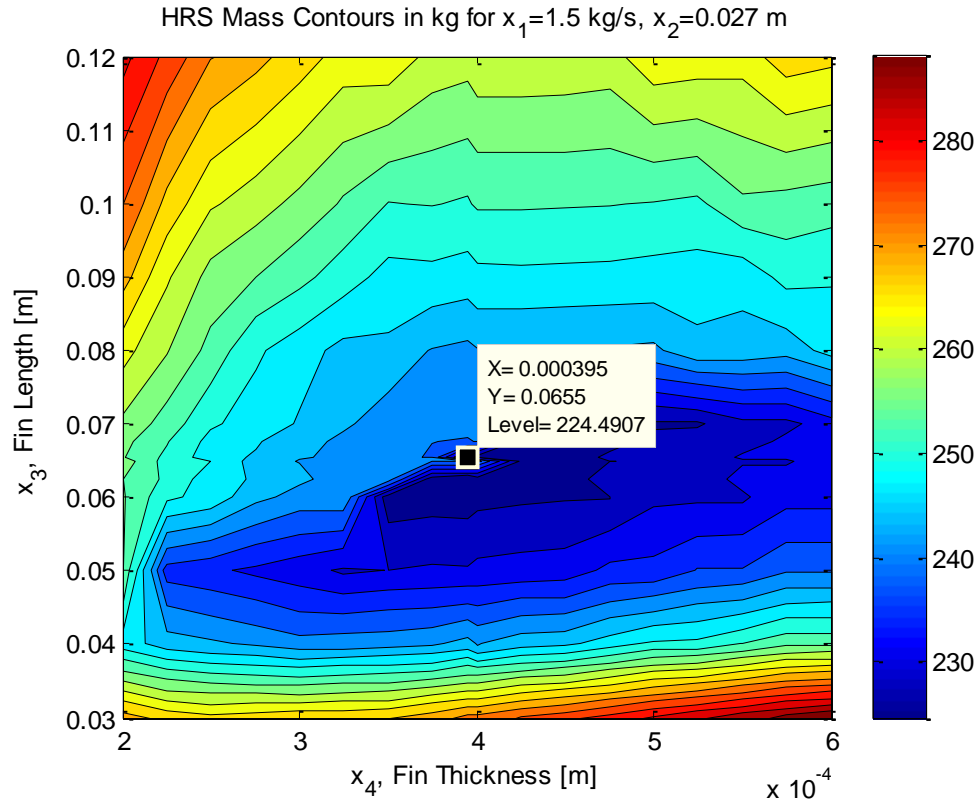
Figure 5.17: Contour plot of HRS Mass versus x_3 and x_4, where x_1 and x_2 are held constant at the optimal values of 1.5 kg/s and 0.027 m respectively, showing the optimal design solution for the 300 kWe power system test case

The HRS areal density, which is the ratio of HRS mass to radiating surface area, was 2.28 kg/m^2, while the radiator areal density, which accounted for the heat pipes, fins and radiator support structure, was 2.01 kg/m^2. This meets NASA's HRS areal density target of 2-4 kg/m^2. Figure 5.18 is a pie chart showing the distribution of component masses for the optimum design (Simulation 4). The heat pipe condensers were the single most-massive component in the HRS, followed by the frame and coolant pump. Future studies may be directed toward in exploring ways to reduce the heat pipe condenser mass, by either decreasing the diameter or using less-dense materials.
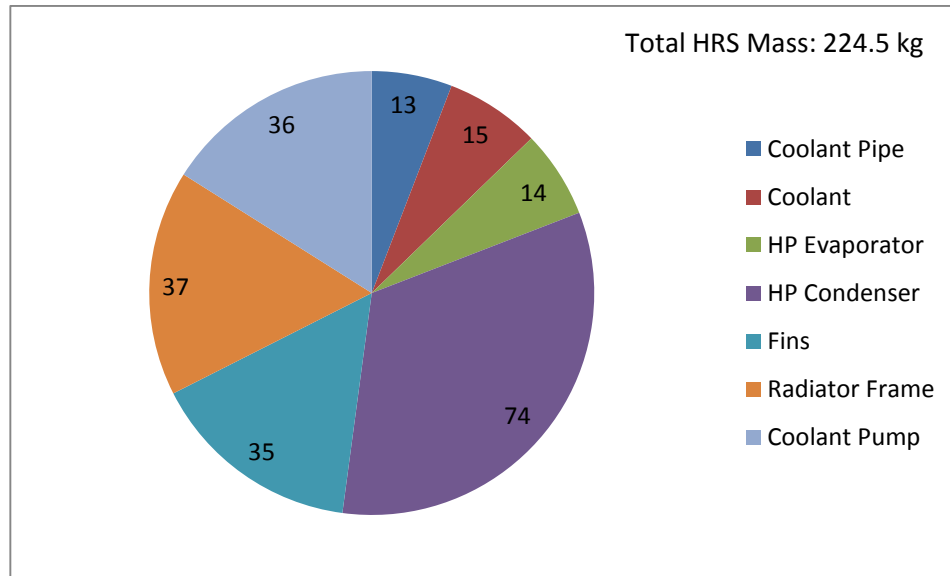
Figure 5.18: The mass distribution of the HRS components in the minimum mass design for the 300 kWe, potassium-Rankine power conversion cycle test case

For most simulations, the optimum coolant mass flow rate, x_1, was a boundary solution while the others design variables had interior point solutions. At the optimum, none of the constraints were active. Since the optimum solution included the upper limit on x_1, the ALIP pump was the biggest limiting factor. Future development of the ALIP pumps may allow for increased capacity. To test how advanced pumps could affect the predicted minimum mass HRS design, the limits on x_1 and x_2 were widened and the results are given in Table 5.6, Simulation 6. In this case, the minimum mass was not limited by any constraint or design variable boundary, so this was the fully unconstrained minimum mass solution. The HRS minimum mass for this case was 194.7 kg, which was about 30 kg less than the original case.

Simulation 7 was run to find the design point that maximized the radiator efficiency. The optimum point, as given in Table 5.6, Simulation 7, resulted in a radiator efficiency of 40.1%, which was 10% higher than the minimum mass solution. This design point had a total HRS mass of 324.0 kg and, as expected, was constrained by pumping power and the upper bound on coolant flow rate. Maximum radiator efficiency occurs when the radiator surface is hottest, so high coolant flow rates are needed.

The total radiator efficiency can be increased by using higher conductivity fins and lowering the thermal resistances even further.

Simulation 8 gives the optimum solution for minimizing HRS mass for a 100 kWe power conversion system with 30% efficiency, with the same constraints and design variable limits as Simulations 1-5. The mass was 80.42 kg, approximately one third the mass of the 300 kWe system, but the solution had a higher radiator efficiency due to the smaller coolant temperature drop. Simulation 9 was built with similar conditions as a study described in Ref. [26], except that the coolant inlet temperature used here was 900 K as compared with 556 K in the study. This was evaluated to demonstrate the significant mass savings achieved just by increasing the reject temperature. Since the lower-temperature study applied slightly different assumptions than this study, an order of magnitude comparison was made. To reject 364 kWt, the HRS in the previous study was predicted to be 854 kg with a total radiating area of 170 m^2, and an HRS areal density of 5 kg/m^2. Simulation 9 shows that a high-temperature carbon fiber radiator can achieve the same heat rejection with a 113 kg HRS that has a radiating area of 34.8 m^2, and an areal density of 3.25 kg/m^2.

Table 5.6: Summary of Optimization Results for Simulations 6-9

Simulation Number	6	7	8	9
Optimization Tool	Design Exp.	Design Exp.	Design Exp.	Design Exp.
Power Generated [kWe]	300	300	100	100
Waste Heat Load [kWt]	700	700	233.3	364
Objective	min Mass	max η_rad	min Mass	min Mass
Simulation Time [hr]	2.4	1.3	0.9	0.55
Number of Iterations Req'd	261	77	359	126
Initial Conditions				
Mass flow rate [kg/s]	2	1.5	1.25	1.28
Coolant Pipe Diameter [m]	0.04	0.03	0.04	0.023
Fin Length [m]	0.08	0.07	0.08	0.06
Fin Thickness [mm]	0.4	0.4	0.3	0.4
Optimal Solution				
Mass flow rate [kg/s]	4.636	1.500	1.356	1.280
Coolant Pipe Diameter [m]	0.045	0.021	0.020	0.023
Fin Length [m]	0.052	0.034	0.054	0.070
Fin Thickness [mm]	0.492	0.947	0.467	0.420
HRS Total Mass [kg]	194.66	324.03	80.42	113.15
Constraint Values				
% pump/generated power	1.74	4.95	3.99	3.61
Radiator Length [m]	5.84	7.52	2.16	4.36
ΔT [K]	76.90	237.77	87.64	144.78
ΔP [kPa]	63.08	556.31	165.28	158.58
Other HRS Results				
Radiator Efficiency [%]	51.63	40.11	46.62	36.00
Number of Heat Pipes	112	222	40	62
Radiator Area [m^2]	23.36	30.07	8.63	17.42
Radiating Surface Area [m^2]*	46.73	60.15	17.25	34.85
Radiator Areal Density [kg/m^2]	2.53	3.90	2.34	1.94
HRS Areal Density [kg/m^2]	4.17	5.39	4.66	3.25
Specific Power [kWt/kg]	3.60	2.16	2.90	3.22
Effective Rad Temperature [K]	762.90	716.23	743.67	697.15

* Twice the radiator footprint

5.3.6 Conclusions

A new model of the heat radiated from a fin was generated for our fin at high temperatures since the Chang model was not valid at our conditions. This model was accurate to within 6% for the following conditions: fin-root temperatures in the range of 400-800°C, fin lengths in the range of 3-12 cm, and fin thicknesses in the range of 0.2-1 mm. A thermal resistance model of the HRS was built to predict the HRS mass and other performance measures for a given set of HRS test cases. This model was used in an optimization code that was built to minimize the total subsystem mass. A test case was selected for the optimization code that uses four HRS design variables. The four design variables were coolant mass flow rate, coolant pipe diameter, radiator fin length and thickness. For the test case of a 300kWe potassium-Rankine power converter with a conversion efficiency of 30% and a cold-end temperature of 900 K, the minimum mass HRS was determined to be 224.5 kg. The values of the design variables at the optimum solution were: coolant mass flow rate of 1.499, coolant pipe diameter of 2.7 cm, fin length of 6.6 cm and fin effective thickness of 0.395 mm. The total radiator area was 77.66 m^2, and the HRS areal density was 2.28 kg/m^2, which meets NASA's HRS areal density goal. This solution was limited by the coolant flow rate, and by the capacity of the ALIP pumps. If higher capacity pumps are developed, this mass could be reduced further. The mass of the HRS was dominated by the heat pipe condensers. Future work should include validating the thermal resistances using experimental or finite element data, designing a frame and deployment mechanism to replace the assumption of 30% of the radiator mass, and investigating ways to reduce the heat pipe mass.

CHAPTER 6

CONCLUSIONS

The four studies presented in this work collectively demonstrate that a carbon fiber heat

radiator offers many benefits over traditional metallic and composite radiators. This research elevated

the technology readiness level of the carbon fiber fin from 2 to 4. Studying various aspects of the fin

concept has provided a thorough understanding of the important design considerations.

A micro-scale model of radiative heat transfer was used to explore the thermal radiation from

an array of fibers. This model and its results were presented in Chapter 2. Calculations show that:

(1) The dependence of the effective emissivity of a carbon fiber fin, that is the total hemispherical

emissivity of the projected fin surface area, on fiber volume fraction was investigated using a

Monte Carlo Ray Tracing model. It was determined that the maximum effective emissivity

occurs at the smallest fiber volume fraction that is still optically thick, which occurs between 15-

20% for a 0.5 mm thick array of uniformly packed fibers. As the fiber volume fraction decreases,

scattering among the fibers increases the amount of radiation that escapes to space as

compared to a flat fin surface, thereby increasing the effective emissivity of the fin.

(2) This increase is quite significant since, for example, fibers with a surface emissivity of 0.7 will

have an effective emissivity of 0.83 when packed in an array with about 13% fiber volume

fraction.

(3) The fiber volume fraction of the 2,000 count fiber tows supplied by Mitsubishi is about 12%,

which is close to the ideal packing density for maximizing effective emissivity as predicted by the

MCRT model.

The design and fabrication of test articles was presented in Chapter 3. The experiments showed

that:

(1) In this proof-of-concept stage, a preliminary fin design was developed based on maximizing specific heat rejection using assumed thermal properties of the fin and heat pipe.

(2) Protocols were developed for weaving the carbon fiber tows and for joining the fiber fin with the heat pipe using a titanium-copper-silver braze foil.

(3) By collaborating with a textile manufacturer, it was proven that the high conductivity carbon fibers can be woven using automated, mass-production looms. This shows that production of the fin material can be readily scaled up.

(4) The brazing method was successful for thin fiber fins, but a proper brazing facility is required for consistent brazing with thick fins due to the limitations of the heating element in the test setup available for this work.

(5) The carbon fiber fin technology readiness level was increased from 2 to 4, which required validation of the fin in the environment.

Measurements of material properties of carbon fibers and fin performance were presented in Chapter 4. The findings included:

(1) A measurement of the spectral emissivity showed only a slight dependence on wavelength, which means that the fibers are nearly gray bodies. The emissivity at room temperature was 0.74, and the emissivity at 600°C was predicted to be about 0.78.

(2) The measured emissivity was used to extract temperature data from IR images of the fins during operation. By comparing thermal models of the fin with surface temperature profiles extracted from IR images, the thermal conductivity of the bulk carbon fiber was determined to be 707±100W/m-K. With estimates of the bulk carbon fiber emissivity and thermal conductivity, models using these property values were used to predict the fin performance over a broader range of fin configurations.

A system-level study of the applicability of the carbon-fiber radiators was presented in Chapter 5. The investigation demonstrated that:

(1) An analytical approximation of the dependence of the heat radiated from a fin on fin length, thickness, and root temperature could be fit by a fourth order polynomial with an R^2 value of 0.9999. This analytical approximation of the radiated power could then be incorporated into a larger, system-level model of the heat rejection subsystem used to design the radiator based on subsystem requirements.

(2) A thermal resistance model of a heat rejection system appropriate for a high-temperature, high-power nuclear-electric powered vehicle was built. Given the heat load and power conversion system coolant temperature, this model predicts many heat rejection subsystem parameters including total mass, area, radiator fin efficiency, and coolant pumping power.

(3) A constrained optimization was run to find the minimum mass heat rejection subsystem design for a test case using the thermal resistance model. The selected test case was a 300 kWe, potassium-Rankine power conversion system generating 700 kWt of waste heat.

(4) The optimal design point had a coolant flow rate of 1.5 kg/s, coolant pipe diameter of 2.7 cm, fin length of 6.6 cm, and fin thickness of 3.95 mm, which resulted in an HRS mass of 224.5 kg. The fin length was slightly shorter than when the mass was optimized in Chapter 3 because there were other mass tradeoffs when considering all of the subsystem components. In the fully unconstrained problem, the optimal solution had a coolant flow rate of 4.6 kg/s, coolant pipe diameter of 4.5 cm, fin length of 5.2 cm, and fin thickness of 4.9 mm, and resulted in an HRS mass of 194.6 kg. This unconstrained design point could be feasible with advanced liquid metal pumps.

(5) The area required to reject 100 kW was compared with published results from a low-temperature heat rejection subsystem for a nuclear-electric power conversion system. For the

high-temperature carbon fiber radiator, 17 m^2 was required compared to the 170 m^2 radiator sized for the low-temperature system.

(6) This lightweight, high-temperature radiator may be the key to enabling nuclear-electric power for space applications where maximizing efficiency is vital to mission feasibility.

CHAPTER 7

FUTURE WORK

If NASA chooses to use an electric power generator for power or propulsion, lightweight radiator designs will continue to be of significant interest. Some of the areas for future work identified in Chapters 2-5 include:

Chapter 2:

(1) Experimental validation of the prediction that the effective emissivity increases with decreasing fiber volume fraction as long as the fiber medium is optically thick. This geometric effect could be tested using fibers made from material with a very-well characterized emissivity, such as an oxidized metal.

(2) The model could also be run with randomly-packed fibers to see how the packing arrangement affects the effective emissivity's dependence on fiber volume fraction. This model would require a three-dimensional domain filled with fibers at random orientations. Studies on fiber insulation using random fiber orientations was conducted by Raghu Arambakam, similar to [57][67]. These references can provide guidance on generating three-dimensional domains of randomly oriented fibers.

Chapter 3:

(1) One major issue encountered during the brazing trials with brazing the test articles in the brazing chamber at MSFC was non-uniform heating. This was in large part due to the heater design and the limited power that could be supplied to the samples. Future work could involve developing a brazing protocol using a proper brazing furnace (an inert gas furnace using argon and large enough for the sample). Developing a heating protocol is an iterative process that involves selecting heating rates, heat soaks, and appropriate temperatures to melt the braze uniformly. Each brazing application requires a heating protocol specific to the type and size of

the furnace and sample. For example, increased sample heat capacity requires longer-duration

heat soaks.

(2) Fabricate test articles with longer sections of heat pipe to demonstrate functionality on a larger

scale. Fight hardware heat pipes may be anywhere from 2-10 m long, so laboratory testing of

larger test articles should employ at least 2 m long heat pipes.

(3) Commission TEAM Inc., or another textile manufacturer, to weave a sample using K13C2U as the

cross tows.

(4) Evaluate options for coating the fins if they will be used in atomic oxygen or if a higher emissivity

is desired. An ideal coating would protect the fibers from atomic oxygen, increase the effective

emissivity of the fin, and not add a significant amount of mass. Options may include chemical

vapor deposited ceramics.

(5) Set criteria about the joint strength based on launch and mission loads. Analyze the strength of

the braze joint and modify accordingly. This could involve using a different quantity of braze, or

using a combination or foil and paste (to help fill the fiber voids), using a different amount of tie

wires, or adding load-absorbing frames around the panels.

Chapter 4:

(1) Design cleaner tests for measuring the longitudinal and through-thickness thermal conductivity,

and radiated power. This could involve fabricating a test chamber with cooled walls that can

approximate an isothermal enclosure, as well as using test articles with longer heat pipes so that

thermal edge effects from the ends of the heat pipe are reduced.

(2) Investigate whether the PAN cross tows have a significant effect on the power rejected by the

fin for a given density of longitudinal pitch tows. This can be done by testing textiles with PAN

and pitch fiber cross tows and comparing the radiated power from the fin, or by measuring the

through-thickness thermal conductivity of the two textiles.

(3) Explore in more detail the dependence of thermal conductivity on temperature for the bulk carbon fibers in the range of 300-800°C. Repeat tests similar to those described in this work for more samples and at multiple temperatures.   Alternatively, direct measurement techniques, such as the guarded hot plate method, can be used to estimate the bulk property.

(4) To demonstrate the versatility of the carbon fiber fin, a low-temperature test article can be fabricated and tested using a titanium-water heat pipe and an epoxy joint. It is predicted that the maximum thermal conductivity of pitch carbon fibers is near 300 K, so there may be lower temperature heat rejection systems that could benefit from this type of fin.

Chapter 5:

(1) Validation of the thermal resistance model using a fully-coupled finite element model of the heat rejection system. These finite element models are often built in Comsol Multiphysics or Thermal Desktop, as these packages offer extensive built-in thermal equations.

(2) Create a more general analytical formulation for the power rejected by a radiator fin that includes thermal conductivity and emissivity as free parameters (similar to Chang's), suitable for high-temperature fins.

(3) As the test case results demonstrated, the heat pipe condensers make up about 33 % of the HRS mass. This result indicates an opportunity to reduce system mass by modifying the heat pipe materials or geometry.

(4) Explore other applications that require lightweight heat transfer devices that could be enabled or improved by using high thermal conductivity carbon fiber instead of traditional materials.

(5) When a space-based power conversion system is adopted by a mission and approaches design phases, the thermal resistance model of the heat rejection subsystem could be used to help evaluate fin material and configuration using the specifics of the application.

(6) Evaluate deployment mechanisms to identify ways to take advantage of the flexibility of carbon fiber radiators to save even more mass versus standard rigid radiator panels. An alternative to the panel design could involve rolling the radiator in its stowed configuration.

APPENDIX

POLYNOMIAL COEFFICIENTS FOR THE FIN PERFORMANCE MODELS DEVELOPED IN CHAPTER 5

Table A.1: Polynomial coefficients for the 3-D, 4th order polynomial fit of the radiated power data, $Q_{fin}(L_f, t_f, T_1)$=(W/m heat pipe), from a heat pipe with two parallel fins, where δ=L/0.12, L is fin length (m), φ=TH/0.001, TH is the total thickness of two fins (m), θ=T/1073.15, and T is root temperature (K).

First Order Terms	Coefficients	Second Order Terms	Coefficients	Third Order Terms	Coefficients	Fourth Order Terms	Coefficients
1	-356.1	δφ	720.19	$δ^3$	-631.88	$δ^4$	-1237.49
δ	234.36	δθ	-5813.55	$φ^3$	1794.03	$δ^3φ$	-201.85
φ	-632.22	φθ	-1310.79	$θ^3$	5852.59	$δ^3θ$	7770.04
θ	3409.25	$δ^2$	1541.01	$δ^2φ$	1344.06	$δ^2φ^2$	2007.02
		$φ^2$	1479.63	$δ^2θ$	-4146.08	$δ^2θ^2$	-9216.53
		$θ^2$	-7709.13	$φ^2δ$	-4808.35	$δ^2φθ$	-6449.32
				$φ^2θ$	-4512.09	$φ^4$	-1882.14
				$θ^2δ$	15652.99	$φ^3δ$	855.33
				$θ^2φ$	2484.03	$φ^3θ$	4639.15
				δφθ	4657.11	$φ^2θ^2$	-5167.46
						$θ^4$	-1103.5
						$θ^3δ$	-2913.25
						$θ^3φ$	3008.29
						$θ^2δφ$	6601.97

Table A.2: Polynomial coefficients for the 3-D, 4th order polynomial fit of the radiated power, $Q_{fin}(L_f, t_f, T_1)$=(W/m heat pipe), data from a single fin with no heat pipe, where δ=L/0.12, L is fin length (m), φ=TH/0.001, TH is the total thickness of the fin (m), θ=T/1073.15, and T is root temperature (K).

First Order Terms	Coefficients	Second Order Terms	Coefficients	Third Order Terms	Coefficients	Fourth Order Terms	Coefficients
1	13717.14	$\delta\varphi$	9483.53	δ^3	-9275.64	δ^4	-2279.14
δ	-38915.80	$\delta\theta$	158993.02	φ^3	-677.48	$\delta^3\varphi$	9204.61
φ	-6299.93	$\varphi\theta$	23669.55	θ^3	-133145.37	$\delta^3\theta$	25485.24
θ	-74801.90	δ^2	38733.26	$\delta^2\varphi$	-7877.01	$\delta^2\varphi^2$	-14150.75
		φ^2	660.94	$\delta^2\theta$	-136204.72	$\delta^2\theta^2$	74229.72
		θ^2	144761.28	$\varphi^2\delta$	3739.51	$\delta^2\varphi\theta$	26130.87
				$\varphi^2\theta$	3725.48	φ^4	-216.58
				$\theta^2\delta$	-131769.00	$\varphi^3\delta$	4349.20
				$\theta^2\varphi$	-28445.51	$\varphi^3\theta$	-2242.61
				$\delta\varphi\theta$	-37538.28	$\varphi^2\theta^2$	536.43
						θ^4	50693.98
						$\theta^3\delta$	21740.05
						$\theta^3\varphi$	13165.60
						$\theta^2\delta\varphi$	5880.29

Table A.3: Polynomial coefficients for the 3-D, 4th order polynomial fit of the fin efficiency data, $\eta_{fin}(L_f, t_f, T_1)$=(W/m heat pipe), from a heat pipe with two parallel fins, where δ=L/0.12, L is fin length (m), φ=TH/0.001, TH is the total thickness of two fins (m), θ=T/1073.15, and T is root temperature (K).

First Order Terms	Coefficients	Second Order Terms	Coefficients	Third Order Terms	Coefficients	Fourth Order Terms	Coefficients
1	0.820672	$\delta\varphi$	1.777401	δ^3	0.800251	δ^4	-0.263747
δ	0.824131	$\delta\theta$	-4.702346	φ^3	3.122574	$\delta^3\varphi$	0.634258
φ	0.318444	$\varphi\theta$	2.572328	θ^3	1.750245	$\delta^3\theta$	-0.751834
θ	0.850592	δ^2	-1.014598	$\delta^2\varphi$	-1.928762	$\delta^2\varphi^2$	0.762621
		φ^2	-2.888200	$\delta^2\theta$	2.408003	$\delta^2\theta^2$	0.343012
		θ^2	-1.853925	$\varphi^2 d$	-0.752834	$\delta^2\varphi\theta$	-0.877581
				$\varphi^2\theta$	-0.724108	φ^4	-1.007969
				$\theta^2 d$	1.671211	$\varphi^3 d$	-0.128780
				$\theta^2\varphi$	-2.565438	$\varphi^3\theta$	-0.320415
				$\delta\varphi\theta$	1.766200	$\varphi^2\theta^2$	0.934275
						θ^4	-0.630248
						$\theta^3\delta$	-0.193811
						$\theta^3\varphi$	0.695290
						$\theta^2\delta\varphi$	-1.051142

REFERENCES

[1] V.J. Lyons, G.A. Gonzalez, M.G. Houts, C.J. Iannello, J.H. Scott, and S. Surampudi. "Draft Space Power and Energy Storage Roadmap, Technology Area 03," NASA Office of the Chief Technologist, November, 2010.

[2] S.M. Canepari, L.A. Bellini, K.J. Riley, and R.W. Hyers, "Damage-Tolerant, Lightweight, High-Temperature Radiator for Nuclear Powered Spacecraft," Final Report, University of Massachusetts Healey Endowment Grant, July 2006.

[3] http://www.nasa.gov/pdf/503466main_space_tech_grand_challenges_12_02_10.pdf (accessed 11/5/2011)

[4] "Mars Exploration Program." http://marsprogram.jpl.nasa.gov/programmissions/ (accessed 1/13/2012)

[5] NASA Factsheet, "Juno Mission to Mars." Jet Propulsion Laboratory, Pasadena, CA. http://www.nasa.gov/pdf/316306main_JunoFactSheet_2009sm.pdf (accessed 1/13/2012)

[6] "Innovative Interstellar Explorer." http://interstellarexplorer.jhuapl.edu/spacecraft/eng_req.html (accessed 1/13 2012).

[7] NASA Glossary: Astronomical Unit. http://neo.jpl.nasa.gov/glossary/au.html (accessed January 16, 2012).

[8] "Voyager: The Interstellar Mission." http://voyager.jpl.nasa.gov/mission/interstellar.html (accessed 5/15/12).

[9] M.Meyer, L.Johnson, B. Palaszewski, D. Goebel, H. White, and D. Coote . "Draft In-Space Propulsion Systems Roadmap, Technology Area 02," NASA Office of the Chief Technologist, November, 2010.

[10]S.A. Hill, C. Kostyk, B. Motil, W. Notardonato, S. Rickman, and T. Swanson. "Draft Thermal Management Systems Roadmap, Technology Area 14," NASA Office of the Chief Technologist, November, 2010.

[11]S. Aftergood. "Background on Space Nuclear Power." Science & Global Security, v.1, pg 93-107 (1989).

[12]J. Chan, J.G. Wood, and J.G. Schreiber. "Development of Advanced Stirling Radioisotope Generator for Space Exploration." NASA Technical Memorandum #214806 (2007).

[13]G.L. Bennett. "Space Nuclear Power: Opening the Final Frontier." AIAA 4th International Energy Conversion Engineering Conference, San Diego, CA, June 2006.

[14]S.L. Rodgers, "Propulsion Research Center." Proceedings of the Workshop on Materials Science for Advanced Space Propulsion, Huntsville, Alabama, October 9-10, 2001.

[15] "External Tank-119 Leaves Michoud Assembly Facility"
http://www.nasa.gov/centers/marshall/michoud/shuttle_et119_1.html (accessed January 14, 2012)

[16] "SNAP Overview." U.S. Department of Energy.
http://etec.energy.gov/Operations/Major_Operations/SNAP_Overview.html (accessed January 13, 2012)

[17] B.A. Cook. "Making Space Nuclear Power a Reality." AIAA 1st. Space Exploration Conference : Continuing the Voyage of Discovery, Orlando, Florida, January 30 - February 1, 2005.

[18] J.P. Fleurial, K. Johnson, J. Mondt, J. Sakamoto, J. Snyder, C. Huang, R. Blair, G. Stapfer, T. Ciallat, W. Determan, P. Frye, B. Heshmatpour, M. Brooks, and K. Tuttle. "Development of Segmented Thermoelectric Multicouple Converter Technology." IEEE Aerospace Conference, Big Sky, Montana (March 4-11, 2006).

[19] A.F. Henry. "Nuclear-Reactor Analysis." The Massachusetts Institute of Technology Press, Cambridge, MA (1975).

[20] L.S. Mason and D. Poston. "Fission Surface Power System Initial Concept Definition," NASA Technical Memorandum 216772 (August 2010).

[21] R.F. Mather. "Nuclear Reactor Space Power Conversion Systems." NASA Technical Memorandum X-52472 (April 1968).

[22] "Themoeletric Generator." http://www.mpoweruk.com/thermoelectricity.htm (accessed 3/28/12).

[23] A.J. Juhasz and R.D. Rovang. "Composite Heat Pipe Development Status: Development of Lightweight Prototype Carbon-Carbon Heat Pipe with Integral Fins and Foil Liner." NASA Technical Memorandum 106909, and Presented at the Ninth International Heat Pipe Conference, Albuquerque, NM (1995).

[24] "Thermionic Converter."
http://www.propagation.gatech.edu/ECE6390/project/Fall2010/Projects/group8/power.html, accessed 3/28/12.

[25] M.G. Houts. "Space Nuclear Power and Propulsion: Materials Challenges for the 21st Century." Presentation from the National Space and Missile Materials Symposium (June 24, 2008).

[26] J. Siamidis, L. Mason, D. Beach, and J. Yuko. "Heat Rejection Concepts for Brayton Power Conversion Systems." NASA Technical Memorandum 213337 (2005).

[27] L.S. Mason. "A Power Conversion Concept for the Jupiter Icy Moons Orbiter." Journal of Propulsion and Power, Vol. 20, No. 5 (September–October 2004).

[28] J. Siamidis. "Heat Rejection Concepts for Lunar Fission Surface Power Applications." NASA Technical Memorandum 214388 (2006).

[29] "Gas Power Cycles." https://wiki.ucl.ac.uk/display/MechEngThermodyn/Gas+Power+Cycles, accessed March 4, 2012.

[30] D. Porter. "NASA Power Systems: Research in New Energy Technology." Purdue Outreach Presentation (2007).

[31] S. Johnson. "Project Prometheus: Two-Phase Flow, Fluid Stability and Dynamics Workshop." NASA Technical Memorandum 212598 (2003).

[32] T.S. Chan, J.G. Wood, and J.G. Schreiber. "Development of Advanced Stirling Radioisotope Generator for Space Exploration." NASA Glenn Technical Memorandum 214806 (2007).

[33] D.M. Goebel and I. Katz. "Fundamentals of Electric Propulsion: Ion and Hall Thrusters." Jet Propulsion Laboratory California Institute of Technology (March 2008).

[34] M.D. Rayman, P. Varghese, D.H. Lehman, and L.L. Livesay. "Results from the Deep Space 1 Technology Validation Mission." Acta Astronautica 47, pg. 475 (2000).

[35] Boeing: NSTAR Ion Thruster Factsheet. http://www.boeing.com/defense-space/space/bss/factsheets/xips/nstar/ionengine.html, accessed January 18, 2012.

[36] R.R Hofer, T.M. Randolph, D.Y. Oh, J.S. Snyder, and K.H. de Grys. "Evaluation of a 4.5 kW Commercial Hall Thruster System for NASA Science Missions." 42nd AIAA/ASME/SAE/ASEE Joint Propulsion Conference, Sacramento, CA (July 2006).

[37] M.D. Rayman. "The Successful Conclusion of the Deep Space 1 Mission: Important Results without a Flashy Title." Space Technology 23, Nos. 2-3, pg. 185 (2003).

[38] A.J. Juhasz and G.P. Peterson, "Review of Advanced Radiator Technologies for Spacecraft Power Systems and Space Thermal Control," NASA Technical Memorandum 4555 (1994).

[39] L. Mason and H.S. Bloomfield. "SP-100 Power System Conceptual Design for Lunar Base Applications." NASA Technical Memorandum 102090 (1989).

[40] J.F. Mondt, V.C. Truscello, and A.T. Marriot. "SP-100 Power Program." Jet Propulsion Laboratory, NASA Report (1994).

[41] H.B. Denham, J.K. Koester, W. Clarke, and A.J. Juhasz. "NASA Advanced Radiator C-C Fin Development." American Institute of Physics Conference Proceedings, 301, p. 1119 (1994).

[42] "Prometheus Project Final Report." Jet Propulsion Laboratory, NASA Report #982-R120461 (2005).

[43] L.S. Mason, D. Palac, M. Gibson, M. Houts, J. Warren, J. Werner, D. Poston, L. Qualla, R. Radel, and S. Harlow. "Design and Test Plans for a Non-Nuclear Fission Power System Technology Demonstration Unit." Proceedings of Nuclear and Emerging Technologies for Space, Albuquerque, NM (February 7-10, 2011).

[44] L.S. Mason. "Recent Advances in Power Conversion and Heat Rejection Technology for Fission Surface Power." NASA Technical Memorandum 216761, July 2010.

[45] D. Ellis, J. Calder, and J. Siamidis. "Summary of the Manufacture, Testing and Model Validation of a Full-Scale Radiator for Fission Surface Power Applications." Proceedings of Nuclear and Emerging Technologies for Space, Albuquerque, NM, February 7-10, 2011, Paper 3181.

[46] "Lambert's Cosine Law." http://en.wikipedia.org/wiki/Lambert's_cosine_law (accessed 6/6/12).

[47] "What is BRDF?" http://www.scratchapixel.com/lessons/3d-advanced-lessons/things-to-know-about-the-cg-lighting-pipeline/what-is-a-brdf/ (accessed 6/6/12).

[48] R. Siegel and J. Howell. Thermal Radiation Heat Transfer, 4th Edition. Taylor and Francis (2002).

[49] A.A. Balandin and D.L. Nika. "Phononics in low-dimensions: engineering phonons in nanostructures and graphene." Materials Today, 15(6), 266-275 (2012).

[50] "Mitsubishi Plastics: Dialead Pitch-Based Carbon Fiber (CF)." http://www.mpi.co.jp/english/products/industrial_materials/pitch_based_carbon_fiber/pbcf001.html#anc10 (accessed 8/12/2013).

[51] X. Zhang, S. Fujiwara, and M. Fujii. "Measurements of thermal conductivity and electrical conductivity of a single carbon fiber." International Journal of Thermophysics, v 21, no 4, pp 965-980 (2000).

[52] B. Zhu, W. Cao, M. Jing, X. Dong, and C. Wang. "Study on Spectral Emissivity of C/C Composites." Spectroscopy and Spectral Analysis, vol. 29, no. 11, pp. 2909-2913 (2009).

[53] G.Neuer. "Emissivity measuremetns on graphite and composite materials in the visible and infrared spectral range." QIRT 92, Eurotherm Series 27, EETI ed., Paris (1992).

[54] Matlab Documentation 2013 http://www.mathworks.com/help/gads/how-the-genetic-algorithm-works.html, accessed 4/30/13.

[55] H.E. Adkins. "NaK(78) Annular Linear Induction Pump (ALIP) Design Study for Proposed Brayton-Cycle Waste Heat Rejection System." NASA Letter Report PNL-47163-1-1 (2004).

[56] D.V. Walters and R.O. Buckius. "Rigorous development for radiation heat transfer in nonhomogeneous absorbing, emitting and scattering media." International Journal of Heat and Mass Transfer, vol. 35, no. 12, pg 3323-3333 (1992).

[57] R. Arambakam, H.V. Tafreshi, and B. Pourdeyhimi . " Analytical Monte Carlo Ray Tracing simulation of radiative heat transfer through bimodal fibrous insulations with translucent fibers." International Journal of Heat and Mass Transfer, vol. 55, pp. 7234-7246 (2012).

[58] Lee Mason, personal communication, July 18, 2012.

[59] Y.H. Zhou, Y.J. Shen, Z.M. Zhang, B.K. Tsai, D.P. DeWitt. "A Monte Carlo model for predicting the effective emissivity of the silicon wafer in rapid thermal processing furnaces." International Journal of Heat and Mass Transfer, vol. 45, pp. 1945-1949 (2002).

[60] C. Argento and D. Bouvard. "A ray tracing method for evaluating the radiative heat transfer in porous media." International Journal of Heat and Mass Transfer, vol 39, no. 15, pp. 3175-3180 (1996).

[61] M.J. Ballico. "Modelling of the effective emissivity of a graphite tube black body." Metrologia, vol. 32, pp. 259-265 (1995).

[62] B.-W. Li and W.-Q. Tao. "Ray effect in ray tracing method for radiative heat transfer." International Journal of Heat and Mass Transfer, vol. 40, no 14, pp. 3419-3426 (1997).

[63] N. Shamsundar, E.M. Sparrow, and R.P. Heinisch. "Monte Carlo solutions-effect of energy partitioning and number of rays." International Journal of Heat and Mass Transfer, vol. 16, no. 3, pp. 690-694 (1973).

[64] V.I. Sapritsky and A.V. Prokhorov. "Calculation of the Effective Emissivities of Specular-Diffuse Cavities by the Monte Carlo Method." Metrologia, vol. 29, pp. 9-14 (1992).

[65] A. Ono. "Calculation of the directional emissivities of cavities by the Monte Carlo method." The Journal of the Optical Society of America, vol. 70, issue 5, pp. 547-554 (1980).

[66] J. Ishii, M. Kobayashi and F. Sakuma. "Effective emissivities of black-body cavities with grooved cylinders." Metrologia, vol. 35, no. 3, pp. 175-180 (1998).

[67] R. Arambakam, S.A. Hosseini, H.V. Tafreshi, and B. Pourdeyhimi. "A Monte Carlo simulation of radiative heat through fibrous media: Effects of boundary conditions and microstructural parameters." International Journal of Thermal Sciences, vol. 50, pp. 935-941 (2011).

[68] J.R. Howell. "The Monte Carlo method in radiative heat transfer." Journal of Heat Transfer, vol. 120, pp. 547-560, (August 1998).

[69] S. Subramaniam and M.P. Menguec. "Solution of the inverse radiation problem for inhomogeneous and anisotropically scattering media using a Monte Carlo technique." International Journal of Heat and Mass Transfer, vol. 34, no. 1, pp. 253-266 (1991).

[70] G. Neuer. "Emissivity measurements on graphite and composite materials in the visible and infrared spectral range." QIRT 92 – Eurotherm Series 27 – EETI ed. (1992).

[71] D.A. Jaworske and T.J. Skowronski. "Portable infrared reflectometer for evaluating emittance." AIP conference Proceedings, Paper 504, pp. 791-796 (2000).

[72] R. Coquard, and D. Baillis, "Radiative characteristics of beds of spheres containing an absorbing and scattering medium." Journal of Thermophysics Heat Transfer, vol. 19, pp. 226-234 (2005).

[73] M.Q. Brewster, "Radiative heat transfer in fluidized bed combustors." ASME Paper No. 83-WA/HT-82 (1983).

[74] Y. Yamada, J.D. Cartigny, and C.L. Tien. " Radiative transfer with dependent scattering by particles: part-2 experimental investigation." Journal of Heat Transfer, Vol. 108, pp. 614-618 (1986).

[75] D. Baillis and J. Sacadura. "Thermal radiation properties of dispersed media: theoretical prediction and experimental characterization." Journal of Quantitative Spectroscopy & Radiative Transfer, vol. 67, pp. 327-363 (2000).

[76] S.C. Lee. "Scattering in fibrous media containing parallel fibers." ASME Journal of Heat Transfer, vol. 118, issue 4, pp. 931-963 (1996).

[77] W.-J. Yang, H. Taniguchi, and K. Kudo. "Radiative Heat Transfer by the Monte Carlo Method." Advances in Heat Transfer, vol. 27 (1995).

[78] Y. Arai. "Structure and Properties of Pitch-Based Carbon Fibers." Nippon Steel Technical Report, no. 59 (October 1993).

[79] W.G. Anderson, B.J. Muzyka, and J.R. Hartenstine. "Variable Conductance Heat Pipe Radiator for Lunar Fission Power Systems." 11th International Energy Conversion Engineering Conference (IECEC), San Jose, CA (July 2013).

[80] M. Singh, T.P. Shpargel, G.N. Morscher, and R. Asthana. "Active metal brazing and characterization of brazed joints in titanium to carbon-carbon composites." Materials Science and Engineering: A, vol. 412, issues 1-2, pp. 123-128 (December 2005).

[81] D. Vallauri, I.C. Atias Adrian, and A. Chrysanthou. "TiC-TiB2 composites: A review of phase relationships, processing and properties." Journal of the European Ceramic Society, vol. 28, issue 8 (2008).

[82] D.M. Jacobson and G. Humpston. Principles of Brazing. ASM International (2005).

[83] "Active Brazing Alloys." http://www.wesgometals.com/products-materials/active-brazing-alloys/, accessed 8/14/13.

[84] H. Mizuhara, E. Heubel, and T. Oyama. "High-Reliability Joining of Ceramic to Metal." The American Ceramic Society Bulletin, vol. 68, no. 9 (September 1989).

[85] J.F. Shackelford, W. Alexander. CRC Materials Science and Engineering Handbook, p.279 (2000).

[86] "Zinc Selenide (ZnSe) Windows," http://www.thorlabs.com/newgrouppage9.cfm?objectgroup_id=3981, accessed 8/20/13.

[87] B. Nysen, L. Piraux, and J.P. Issi. "Thermal conductivity of pitch-derived fibres." J. Phys. D: Appl. Phys., vol. 18, pp 1307-1310 (1985).

[88] C. Pradere, J.C. Batsale, J.M. Goyheneche, R. Pailler, and S. Dihaire. "Thermal properties of carbon fibers at very high temperature." Carbon, vol. 47, pp. 737-743 (2009).

[89] "Properties of Pure Copper," http://www-ferp.ucsd.edu/LIB/PROPS/PANOS/cu.html, accessed 8/10/13.

[90] "Material properties of molybdenum," http://www.plansee.com/en/Materials-Molybdenum-402.htm, accessed 8/10/2013.

[91]H.V. Chang. "Optimization of a Heat Pipe Radiator Design." AIAA 19th Thermophysics Conference, Snowmass, CO (June 1984).

[92]D.P. Dewitt, F.P. Incropera, T.L. Bergman, and A.S. Lavine. Introduction to Heat Transfer, Sixth Edition, John Wiley & Sons Inc. (2011).